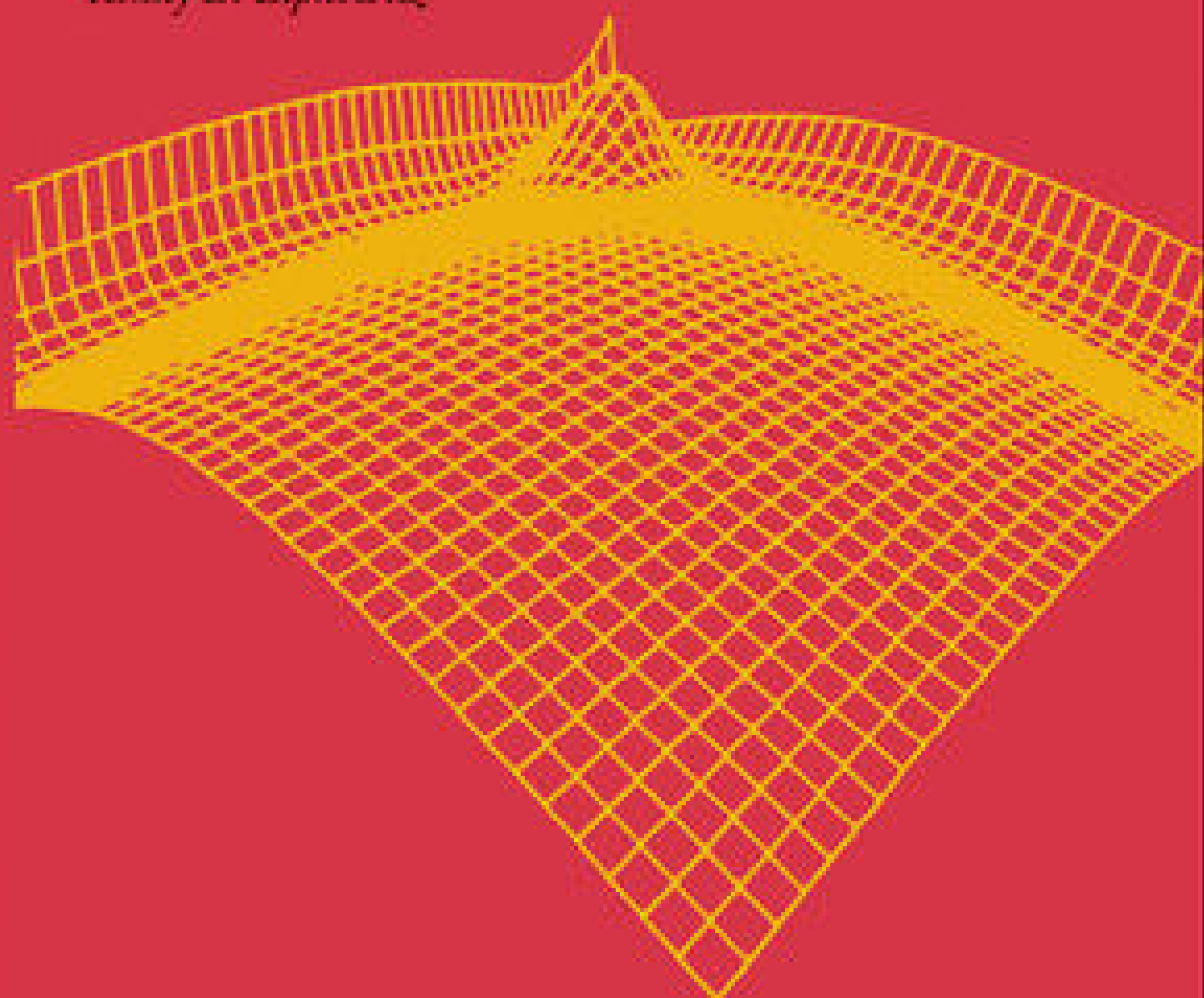


REVIEWS IN COMPUTATIONAL CHEMISTRY

Kenny B. Lipkowitz



 WILEY

VOLUME 27

Contents

1. Brittle Fracture: From Elasticity Theory to Atomistic Simulations	1
<i>Stefano Giordano, Alessandro Mattoni, and Luciano Colombo</i>	
Introduction	1
Essential Continuum Elasticity Theory	5
Conceptual Layout	5
The Concept of Strain	6
The Concept of Stress	10
The Formal Structure of Elasticity Theory	12
Constitutive Equations	13
The Isotropic and Homogeneous Elastic Body	15
Governing Equations of Elasticity and Border Conditions	18
Elastic Energy	19
Microscopic Theory of Elasticity	21
Conceptual Layout	21
Triangular Lattice with Central Forces Only	22
Triangular Lattice with Two-Body and Three-Body Interactions	25
Interatomic Potentials for Solid Mechanics	28
Atomic-Scale Stress	36
Linear Elastic Fracture Mechanics	47
Conceptual Layout	47
Stress Concentration	48
The Griffith Energy Criterion	49
Opening Modes and Stress Intensity Factors	51
Some Three-Dimensional Configurations	53
Elastic Behavior of Multi Fractured Solids	58
Atomistic View of Fracture	60
Atomistic Investigations on Brittle Fracture	64
Conceptual Layout	64
Griffith Criterion for Failure	64
Failure in Complex Systems	68
Stress Shielding at Crack-Tip	75

Acknowledgments	78
Appendix: Notation	78
References	78
2. Dissipative Particle Dynamics	85
<i>Igor V. Pivkin, Bruce Caswell, and George Em Karniadakis</i>	
Introduction	85
Fundamentals of DPD	86
Mathematical Formulation	86
Units in DPD	88
Thermostat and Schmidt Number	90
Integration Algorithms	92
Boundary Conditions	94
Extensions of DPD	97
DPD with Energy Conservation	97
Fluid Particle Model	98
DPD for Two-Phase Flows	98
Other Extensions	99
Applications	99
Polymer Solutions and Melts	100
Binary Mixtures	100
Amphiphilic Systems	102
Red Cells in Microcirculation	103
Summary	104
References	104
3. Trajectory-Based Rare Event Simulations	111
<i>Peter G. Bolhuis and Christoph Dellago</i>	
Introduction	111
Simulation of Rare Events	111
Rare Event Kinetics from Transition State Theory	113
The Reaction Coordinate Problem	114
Accelerating Dynamics	116
Trajectory-Based Methods	116
Outline of the Chapter	117
Transition State Theory	118
Statistical Mechanical Definitions	118
Rate Constants	119
Rate Constants from Transition State Theory	121
Variational TST	126
The Harmonic Approximation	126

Reactive Flux Methods	128
The Bennett–Chandler Procedure	128
The Effective Positive Flux	134
The Ruiz–Montero–Frenkel–Brey Method	135
Transition Path Sampling	137
Path Probability	137
Order Parameters	139
Sampling the Path Ensemble	141
Shooting Move	142
Sampling Efficiency	147
Biasing the Shooting Point	147
Aimless Shooting	149
Stochastic Dynamics Shooting Move	149
Shifting Move	152
Flexible Time Shooting	154
Which Shooting Algorithm to Choose?	156
The Initial Pathway	157
The Complete Path Sampling Algorithm	158
Enhancement of Sampling by Parallel Tempering	158
Multiple-State TPS	160
Transition Path Sampling Applications	161
Computing Rates with Path Sampling	161
The Correlation Function Approach	161
Transition Interface Sampling	164
Partial Path Sampling	176
Replica Exchange TIS or Path Swapping	179
Forward Flux Sampling	184
Milestoning	185
Discrete Path Sampling	186
Minimizing the Action	189
Nudged Elastic Band	189
Action-Based Sampling	191
Transition Path Theory and the String Method	193
Identifying the Mechanism from the Path Ensemble	196
Reaction Coordinate and Committor	196
Transition State Ensemble and Committor Distributions	197
Genetic Neural Networks	199
Maximum Likelihood Estimation	200
Conclusions and outlook	202
Acknowledgments	202
References	202

4.	Understanding Metal/Metal Electrical Contact Conductance from the Atomic to Continuum Scales	211
	<i>Douglas L. Irving</i>	
	Introduction	211
	Factors That Influence Contact Resistance	212
	Surface Roughness	213
	Local Heating	215
	Intermixing and Interfacial Contamination	223
	Dimensions of Contacting Asperities	224
	Computational Considerations	225
	Atomistic Methods	226
	Calculating Conductance of Nanoscale Asperities	230
	Hybrid Multiscale Methods	231
	Characterization of Defected Atoms	233
	Selected Case Studies	235
	Conduction Through Metallic Nanowires	235
	Multiscale Methods Applied to Metal/Metal Contacts	241
	Concluding Remarks	247
	Acknowledgments	247
	References	247
5.	Molecular Detailed Simulations of Lipid Bilayers	253
	<i>Max L. Berkowitz and James T. Kindt</i>	
	Introduction	253
	Membrane Simulation Methodology	254
	Force Fields	254
	Choice of the Ensemble	256
	Verification of the Force Field	258
	Monte Carlo Simulation of Lipid Bilayers	264
	Detailed Simulations of Bilayers Containing Lipid Mixtures	266
	Conclusions	281
	References	281
6.	Semiclassical Bohmian Dynamics	287
	<i>Sophya Garashchuk, Vitaly Rassolov, and Oleg Prezhdo</i>	
	Introduction	287
	The Formalism and Its Features	289
	The Trajectory Formulation	289
	Features of the Bohmian Formulation	292

The Classical Limit of the Schrödinger Equation and the Semiclassical Regime of Bohmian Trajectories	297
Using Quantum Trajectories in Dynamics of Chemical Systems	299
Bohmian Quantum-Classical Dynamics	300
Mean-Field Ehrenfest Quantum-Classical Dynamics	301
Quantum-Classical Coupling via Bohmian Particles	302
Numerical Illustration of the Bohmian Quantum-Classical Dynamics	305
Properties of the Bohmian Quantum-Classical Dynamics	309
Hybrid Bohmian Quantum-Classical Phase-Space Dynamics	311
The Independent Trajectory Methods	313
The Derivative Propagation Method	313
The Bohmian Trajectory Stability Approach. Calculation of Energy Eigenvalues by Imaginary Time Propagation	314
Bohmian Mechanics with Complex Action	316
Dynamics with the Globally Approximated Quantum Potential (AQP)	317
Global Energy-Conserving Approximation of the Nonclassical Momentum	318
Approximation on Subspaces or Spatial Domains	324
Nonadiabatic Dynamics	328
Toward Reactive Dynamics in Condensed Phase	338
Stabilization of Dynamics by Balancing Approximation Errors	340
Bound Dynamics with Tunneling	348
Conclusions	353
Acknowledgments	355
Appendix A: Conservation of Density within a Volume Element	355
Appendix B: Quantum Trajectories in Arbitrary Coordinates	356
Appendix C: Optimal Parameters of the Linearized Momentum on Spatial Domains in Many Dimensions	359
References	360
7. Prospects for Career Opportunities in Computational Chemistry	369
<i>Donald B. Boyd</i>	
Introduction and Overview	369
Methodology and Results	371
Proficiencies in Demand	376
Analysis	381
An Aside: Economics 101	385

Prognosis	389
Acknowledgments	393
References	393
Appendix: List of Computational Molecular Scientists	395
Subject Index	473

CHAPTER 1

Brittle Fracture: From Elasticity Theory to Atomistic Simulations

**Stefano Giordano, Alessandro Mattoni,
and Luciano Colombo**

*Department of Physics of the University of Cagliari and
CNR-IOM (SLACS Unit), Cittadella Universitaria, I-09042
Monserrato (Ca), Italy*

INTRODUCTION

Understanding the mechanical properties of materials with theory traditionally has been done by using continuum methods, ranging from elastic theory (in both linear and nonlinear regimes), to plastic theory, and to fracture mechanics. The computational counterpart of continuum modeling is represented by finite element analysis. Continuum theories have been extremely successful, as proved by the tremendous achievements reached in structural design of buildings, ships, bridges, air-/space crafts, nuclear reactors, and so on. Overall this represents the core of theoretical and computational solid mechanics.

In the last 20 years or so, the technological rush toward nano-sized systems has forced researchers to investigate mechanical phenomena at a length scale in which matter no longer can be considered as a continuum. This is the case, for instance, of investigating the crack-related features in a material displaying elastic or structural complexity (or, equivalently, inhomogeneity or disorder) at the nanoscale. This problem of atomic-scale granularity immediately seems to be prohibitive for (standard) solid mechanics. To better elaborate on this

concept, let us focus on the case of a crack propagating into a nano-composite material, where occasionally it faces phase boundaries between the matrix and the fiber. There are serious conceptual limitations in applying solid mechanics in such situations because continuum stress and strain fields are mathematically singular at vanishing distances from the crack tip. This, of course, prevents any meaningful application of continuum mechanics over a region in the near vicinity of the crack tip (i.e., at the length scale where a direct interaction between the crack and the phase boundary indeed occurs). Computational limitations exist as well for the same problem. As a matter of fact, the total numerical workload of the continuum analysis based on finite elements could become prohibitively large because of the extreme refinement of the numerical mesh that is required to take into account the inhomogeneity displayed at the nanoscale. Such a mesh refinement, therefore, would be stopped at a larger length scale, representing a (possibly bad) coarse grain picture of the actual elastic or structural disorder.

A new feeling within the computational materials science community is that a completely different approach (other than continuum modeling) really is needed for predicting mechanical properties at the nanoscale. Such a novel approach is based on a direct atomistic description of relevant phenomena, and therefore, it has been named atomistic (or atomic-scale) modeling. The key idea of atomistic modeling is to look at a solid body under mechanical load as being an assembly of atoms interacting through direct coupling; their collective response to loading eventually will drive the overall mechanical response (for the above discussed case, such a collective response will drive the propagation of the crack). Because the material is now resolved atomistically, there is no ambiguity in representing its actual nanostructure, displaying in principle any combination (at any possible relative distance) of cracks, phase boundaries, or whatever kind of elastic inclusion. In other words, atomistic modeling naturally operates at the length scale, which falls out-of-reach of continuum theories. Furthermore, because the response is represented by the collective displacement of atoms, the mechanical behavior is governed by the selected interatomic potentials, which in turn, are derived from a fundamental analysis of chemical bonding between atoms. In other words, no guess is needed any longer about the constitutive equations for the mechanical behavior (i.e., the actual stress–strain relation for the investigated material). To clarify this conceptual breakthrough, it is useful to turn back to the crack-inclusion interaction problem; the mathematical singularity of stress and strain fields at the crack tip is removed naturally when mapping the problem onto a discrete atom-resolved lattice. The elementary step for crack advancement, in fact, is represented by a bond breaking event, whereas the corresponding strain field simply is computed by the prediction of the new atomic coordinates (just after the bond snaps). Similarly, the local stress is computed on each displaced atom so that no singular behavior ever is reached. In this respect, atomistic modeling could be viewed at as a first-principles mechanical theory.

The present chapter mainly is intended as a tutorial introduction to brittle fracture. Although the emphasis is on atomistic simulations, a detailed (but, hopefully, gentle) introduction to the continuum elasticity theory and to fracture mechanics is offered as well. We believe that basic mechanical concepts like strain, stress, and border conditions—which are central to this topic—more effectively are introduced and discussed within a continuum framework. This allows us to develop such concepts at the needed degree of rigorous formalism, as is actually done in the “Essential Continuum Elasticity Theory” Section.

In the “Microscopic Theory of Elasticity” Section, we introduce the microscopic theory of elasticity, in which the atomic (discrete) structure of materials explicitly is taken into account as the main underlying constitutive hypothesis. By making use of simple two-dimensional model systems, we develop the most fundamental features of the microscopic description of elasticity. This will determine the minimal degree of complexity that any interatomic force model must display to describe correctly essential elasticity. We then will describe modern interaction potentials and outline their most recent applications. Another very important topic discussed in this section is the atomic-scale formulation of the stress; here we develop the formalism under the most general assumptions, and provide practical recipes for any two-body or many-body potential. Establishing a clean and complete theory for atomic-level stress tensor, which today is still a matter of investigation, is a crucial part of this section.

The “Linear Elastic Fracture Mechanics” Section is devoted to presenting the basics of brittle fracture, starting from the energy balance criterion developed by Griffith. Here, we also discuss the typical border conditions reflecting the kind of loading that can be applied to a cracked solid. The importance of this issue often is underestimated in typical atomistic simulations, which therefore, sometimes do not correspond—even if technically correct—to any realistic situation. We also present some of our recent continuum results obtained for multicracked systems. Finally, the section is completed with a qualitative introduction to the atomistic view of fracture.

This review concludes with a section titled “Atomistic Investigation on Brittle Fracture” in which we discuss extensively our investigations on brittle fracture in silicon carbide. Several topics are developed, all of them being underpinned by the same concept: Atomistic simulations are both consistent with standard fracture mechanics (when referred to a situation that can be treated equally well by two different approaches), and they provide a valuable source of hints for developing improved continuum models. Our main message is that by means of molecular dynamics simulations, it is indeed possible to develop atomically informed mesoscopic models that enlarge the range of validity of continuum theory down to the nanoscale.

Fracture mechanics is a beautiful example of how a natural science has developed over the years. It is, therefore, instructive to consider its historical evolution. The attempt to formulate a microscopic (i.e., atomistic or molecular) theory of elasticity has been addressed largely in the scientific literature since

the first approaches to model the mechanical behavior of elastic bodies. During the nineteenth century, different approaches have been followed. Fresnel¹ and Navier² published in 1820 and 1821, respectively, very similar results based on the so-called *corpuscular approach*. They systematically adopted the Lagrange “*Mécanique analytique*,” describing the motion of an elastic solid decomposed into a given collection of point masses interacting by means of distance-varying elastic forces. This approach did not consider the modern concept of stress because the forces were transmitted at the molecular level only. Although this microscopic description of fundamental interactions is qualitatively consistent with modern solid state physics,^{3–5} the model by Fresnel and Navier (as well as their actual understanding of microscopic material physics) was too rudimentary and, therefore, resulted in being insufficient for developing either a consistent or a predictive theory. An alternative methodology was followed by assuming the mass distribution within a solid body to be continuous throughout its volume; in 1822, Cauchy⁶ introduced the *continuum approach* to study the elastic properties of solid bodies. Cauchy obtained the equilibrium equations exactly in the same form in which they appear in modern textbooks; in particular, he defined a tensorial pressure (stress), and he proved that the stress tensor divergence is zero (at equilibrium and in absence of volumetric external forces). Moreover, in 1828, Cauchy⁷ introduced the linear constitutive relations (the Hooke law established in 1678) defining two different elastic constants needed to model isotropic media.

Despite several efforts, the problem of reconciling the opposing corpuscular and continuum approaches remained an intriguing challenge for many years.⁸ The simplest atomistic models—including only central two-body interactions—describe the mechanical behavior of any material by means of a single elastic constant, a sort of *scalar stiffness*. At variance, the continuum approach predicts, in the isotropic case, the need for two independent and material-specific parameters. So, the basic question is as follows: Do we need just one modulus or actually two elastic moduli to describe elastic isotropic media properly?

The first robust attempt to address this problem was given by Voigt.⁹ According to his model, the regular structure of a crystal suggests that, when a molecule (or atom) is added to the lattice, an ad hoc couple of forces act on the molecule to set its correct orientation within the crystal. In modern terminology, we can say that such a molecular torque corresponds to an effective many-body interaction that is at work among the elementary constituents of the lattice (either atoms or molecules). By considering both the central forces and the three-body interactions (i.e., the simplest effective molecular torques), Voigt obtained the general equations of elasticity theory for isotropic solids containing two independent constants, as predicted by the continuum approach and as is consistent with experimental knowledge. In conclusion, three-body forces and angle-dependent forces must be considered to reproduce the correct behavior of a solid elastic body.

The modern theory of elasticity is concerned with the mechanics of deformable media, which completely recover their original shape and give up all work expended in the deformation after the applied deforming forces are removed. The development of the theory of elasticity was based on the concept of a continuous medium, which enables one to ignore its atomic structure and to describe macroscopic phenomena by the methods of continuum mechanics.¹⁰ Within the framework of elasticity theory, the so-called fracture mechanics has been introduced, which deals with the failure of a given body or structure due as a result of the propagation of cracks or fractures.¹¹

The fundamental science underlying fracture is rich, spanning from physics and chemistry at the atomic scale to micromechanics of materials and to continuum mechanics of structures on the large scale. Most real materials, when loaded with some stresses, can exhibit internal cuts in their microstructure, called cracks or fractures, which cause degradation of the mechanical properties or complete breaking (failure). Thus, it is observed that fracture is a significant problem in the industrialized world and that a theoretical and practical basis for design against fracture is needed. Fracture mechanics deals essentially with the following problems. Given a structure with a preexisting crack or crack-like flaw, we must determine what loads can be tolerated by the structure for any given crack size or configuration. Similarly, considering a structure in a given state of load, it is important to predict the creation or the growth of a crack. Moreover, for a given number of cycles of loading in a system, we are interested in determining when a crack propagates catastrophically. Finally, we might ask what size crack can be allowed to exist in a given component of a device or engineering structure for it to operate safely.

From a historical point of view, the first experiments on fracture mechanics were performed by Leonardo da Vinci, who measured the strength of iron wires in terms of their length. He found that the strength varied inversely with wire length. This result implied that flaws in materials govern the strength. In fact, for a longer wire, we have a larger volume of material, and therefore, there is a higher probability of encountering many flaws. Of course, it is a qualitative result only. The first quantitative result connecting mechanical stress and crack size was found by Griffith in 1920,¹² and fracture mechanics became a science-based engineering discipline during World War II. For a brief review of the history and development of fracture mechanics, see Ref. 13.

ESSENTIAL CONTINUUM ELASTICITY THEORY

Conceptual Layout

The classical theory of elasticity is based on the approximation of *continuum medium*, which consists of replacing the full set of pointlike atomic masses distributed within a solid body by a continuum distribution of mass.

This approximation is valid when the spatial wavelength of the displacement field (describing the imposed deformation) is much greater than the interatomic distance. In this case, the crystalline structure is not relevant for determining the variation of the shape of the solid body; the continuum macroscopic description is, in fact, sufficient to study its mechanical response. The next most important ideas of elasticity theory are the concepts of strain and the stress, both of which are described easily by means of specific mathematical objects called tensors.^{14–16}

A deformation relates two configurations (or states) of the material. The initial state is called the *reference configuration* and usually refers to the initial time; the other is called the *current configuration* and refers to a following time (which may be regarded conveniently as the present moment).^{17,18} In linear elasticity, the strains (typically extensions and shears) and the angles of rotation are considered small.¹⁹ In this case, we use the *infinitesimal strain tensor* (or *small strain tensor*), which is the main object introduced to describe all deformation features.^{20,21}

To calculate the force of interaction between volume elements situated in an arbitrary closed region (imagined to be isolated within the body) and volume elements situated outside this region, it was advantageous to introduce the concept of the average force of interaction between them. This approach provides us with the definition of the *stress tensor*, which takes into consideration all interaction forces among the volume elements of the continuum body.^{22,23}

The strain in a given body can be considered the effect of the applied stress. The relationship between the strain tensor and the stress tensor depends on the material under consideration, and therefore, it is called the *constitutive equation*.²² The empirical Hooke law establishes a linear relation between stresses (forces inside the body) and strains (deformations of the body itself). In its general form, Hooke's law can describe an arbitrary inhomogeneous and anisotropic behavior of the material under consideration.²⁰ However, the most simple and important constitutive equation used in elasticity theory applies to materials that are homogeneous (the elastic behavior is the same at any point of the body) and isotropic (the direction of application of the stress is not relevant). The linear, homogeneous, and isotropic constitutive equation is obtained and discussed in the following sections.

The Concept of Strain

Let \vec{x} be the position vector of a volume element within a body in its reference (equilibrium) configuration, and let \vec{X} be the position of the same volume element in the current configuration. Both configurations are framed within the same cartesian coordinate system (see Figure 1). Because \vec{X} is a function of \vec{x} , we can write the following:

$$\vec{X} = \vec{f}(\vec{x}) = (f_1(\vec{x}), f_2(\vec{x}), f_3(\vec{x})) \quad [1]$$

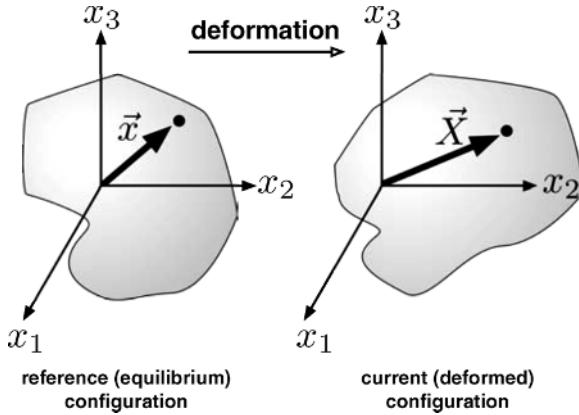


Figure 1 Reference configuration and current configuration after a deformation.

We observe that the function \vec{f} , connecting the vector \vec{X} to the vector \vec{x} , is a vector field. Of course, the relation $\vec{f}(\vec{x}) \neq \vec{f}(\vec{y})$ is verified for any pair of volume elements with $\vec{x} \neq \vec{y}$ in the reference configuration. This means that \vec{f} is a biunivocal vector function, and therefore, the inverse function \vec{f}^{-1} always exists. We also assume that \vec{f} and \vec{f}^{-1} are differentiable functions. Basically, the vector field $\vec{f}(\vec{x})$ contains all the information about the deformation driving the solid body from the reference to the current configuration. In the theory of elasticity, the deformation gradient $\hat{F} = \{F_{ij}, i, j = 1, 2, 3\}$, and

$$F_{ij} = \frac{\partial f_i}{\partial x_j} \quad [2]$$

is introduced. The matrix \hat{F} also is referred to as the Jacobian matrix of the transformation and has two important properties: (1) It is not singular because of the invertibility of \vec{f} ($\exists \hat{F}^{-1}$ such that $\hat{F}\hat{F}^{-1} = \hat{F}^{-1}\hat{F} = \hat{I}$); and (2) its determinant is always strictly positive ($\det F > 0$).¹⁷ We can better exploit the concept of deformation by introducing the displacement field $\vec{u}(\vec{x})$ as:

$$\vec{X} = \vec{f}(\vec{x}) = \vec{x} + \vec{u}(\vec{x}) \quad [3]$$

The Jacobian matrix of the displacement $\hat{J} = \{J_{ij}, i, j = 1, 2, 3\}$ (i.e., the displacement gradient), therefore, is calculated as:

$$J_{ij} = \frac{\partial u_i}{\partial x_j} \quad [4]$$

From the definitions of \hat{F} and \hat{J} , we have $\hat{F} = \hat{I} + \hat{J}$ or $\hat{J} = \hat{F} - \hat{I}$.

In *linear* elasticity, the extent of the deformations is assumed small. Although this notion is intuitive, it can be formalized by imposing that, for small deformations, \hat{F} is very similar to \hat{I} or, equivalently, that \hat{J} is very small. Therefore, we adopt as an operative definition of *small deformation* the following relation:

$$\text{Tr}(\hat{J}\hat{J}^T) \ll 1 \quad [5]$$

That is, a deformation hereafter will be regarded as *small*, provided that the trace of the product $\hat{J}\hat{J}^T$ is negligible. We observe that \hat{J} can be written as the sum of a symmetric and a skew-symmetric (antisymmetric) part as follows:

$$J_{ij} = \underbrace{\frac{1}{2} \left(\frac{\partial u_i}{\partial x_j} + \frac{\partial u_j}{\partial x_i} \right)}_{\text{symmetric}} + \underbrace{\frac{1}{2} \left(\frac{\partial u_i}{\partial x_j} - \frac{\partial u_j}{\partial x_i} \right)}_{\text{skew-symmetric}} = \epsilon_{ij} + \Omega_{ij} \quad [6]$$

Accordingly, we define the (symmetric) *infinitesimal strain tensor* (or *small strain tensor*) as:

$$\epsilon_{ij} = \frac{1}{2} \left(\frac{\partial u_i}{\partial x_j} + \frac{\partial u_j}{\partial x_i} \right) \quad [7]$$

and the (antisymmetric) *local rotation tensor* as:

$$\Omega_{ij} = \frac{1}{2} \left(\frac{\partial u_i}{\partial x_j} - \frac{\partial u_j}{\partial x_i} \right) \quad [8]$$

Such a decomposition²⁰ is useful to obtain the following very important properties of the small strain tensor, which is the key quantity to determine the state of deformation of an elastic body:

- For a pure local rotation (a volume element is rotated but not changed in shape and size), we have $\hat{J} = \hat{\Omega}$ and, therefore, $\hat{\epsilon} = 0$. This means that the small strain tensor does not take into account any local rotation but only the changes of shape and size (dilatations or compression) of that element of volume.²²

Let us clarify this fundamental result with point \vec{x} inside a volume element that is transformed to $\vec{x} + \vec{u}(\vec{x})$ in the current configuration. Under a pure local rotation, we have $\vec{x} + \vec{u}(\vec{x}) = \hat{R}\vec{x}$, where \hat{R} is a given orthogonal rotation matrix (satisfying $\hat{R}\hat{R}^T = \hat{I}$). We simply obtain $\vec{u}(\vec{x}) = (\hat{R} - \hat{I})\vec{x}$ or, equivalently, $\hat{J} = \hat{R} - \hat{I}$. Because the applied deformation (i.e., the local rotation) is small by hypothesis, we observe that the difference $\hat{R} - \hat{I}$ is small too. The product $\hat{J}\hat{J}^T$, therefore, will be

negligible, leading to the following expression:

$$\begin{aligned} 0 &\cong \hat{\mathbf{j}}\hat{\mathbf{j}}^T = (\hat{\mathbf{R}} - \hat{\mathbf{I}})(\hat{\mathbf{R}}^T - \hat{\mathbf{I}}) = \hat{\mathbf{R}}\hat{\mathbf{R}}^T - \hat{\mathbf{R}} - \hat{\mathbf{R}}^T + \hat{\mathbf{I}} \\ &= \hat{\mathbf{I}} - \hat{\mathbf{R}} - \hat{\mathbf{R}}^T + \hat{\mathbf{I}} = -\hat{\mathbf{j}} - \hat{\mathbf{j}}^T \end{aligned} \quad [9]$$

Therefore, $\hat{\mathbf{j}} = -\hat{\mathbf{j}}^T$ or, equivalently, $\hat{\mathbf{j}}$ is a skew-symmetric tensor. It follows that $\hat{\mathbf{j}} = \hat{\mathbf{\Omega}}$ and $\hat{\mathbf{\epsilon}} = 0$. We have verified that a pure rotation corresponds to zero strain. In addition, we remark that the local rotation of a volume element within a body cannot be correlated with any arbitrary force exerted in that region (the forces are correlated with $\hat{\mathbf{\epsilon}}$ and not with $\hat{\mathbf{\Omega}}$); for this reason, the infinitesimal strain tensor is the only relevant object for the analysis of the deformation because of applied loads in elasticity theory.

- The infinitesimal strain tensor allows for the determination of the length variation of any vector from the reference to the current configuration. By defining $\epsilon_{\vec{n}}$ as the relative length variation in direction \vec{n} , it is possible to prove that:²²

$$\epsilon_{\vec{n}} = \vec{n} \times (\hat{\mathbf{\epsilon}} \vec{n}) \quad [10]$$

If \vec{n} is actually any unit vector of the reference frame, then it is straightforward to attribute a geometrical meaning to the components ϵ_{11} , ϵ_{22} , and ϵ_{33} of the strain tensor. Because $\epsilon_{\vec{e}_i} = \vec{e}_i \times (\hat{\mathbf{\epsilon}} \vec{e}_i) = \epsilon_{ii}$, they describe the relative length variations along the three axes of the reference frame.

- The infinitesimal strain tensor allows for the determination of the angle variation between any two vectors from the reference to the current configuration. The variation of the angle defined by the two orthogonal directions \vec{n}_1 and \vec{n}_2 is given by:²²

$$\Delta\alpha_{\vec{n}_1, \vec{n}_2} = 2\vec{n}_1 \times (\hat{\mathbf{\epsilon}} \vec{n}_2) \quad [11]$$

The present result is also useful for giving a direct geometrical interpretation of the components ϵ_{12} , ϵ_{23} , and ϵ_{13} of the infinitesimal strain tensor. As an example, we take into consideration the component ϵ_{12} , and we assume that $\vec{n}_1 = \vec{e}_1$ and $\vec{n}_2 = \vec{e}_2$. The quantity $\Delta\alpha_{\vec{n}_1, \vec{n}_2}$ represents the variation of a right angle lying on the plane (x_1, x_2) . Because $\epsilon_{12} = \vec{e}_1 \times (\hat{\mathbf{\epsilon}} \vec{e}_2)$, we easily obtain the relationship $\Delta\alpha_{\vec{n}_1, \vec{n}_2} = 2\epsilon_{12} = \frac{\partial u_1}{\partial x_2} + \frac{\partial u_2}{\partial x_1}$. In other words, ϵ_{12} is half the variation of the right angle formed by the axis x_1 and x_2 . Of course, the same interpretation is valid for the other components ϵ_{23} and ϵ_{13} .

Knowing the $\hat{\epsilon}$ tensor field within a strained (i.e., deformed) elastic body allows us to calculate the volume change ΔV of a given region. We get $\Delta V = \int_V \text{Tr}(\hat{\epsilon})d\vec{x}$, where V is the volume of the unstrained region.¹⁷

This discussion states that, given a displacement field $\vec{u}(\vec{x})$, the components of the infinitesimal strain tensor are easily calculated by direct differentiation. The inverse problem is much more complicated.^{17,22} Given an arbitrary infinitesimal strain tensor $\hat{\epsilon}(\vec{x})$, we could search for that displacement field $\vec{u}(\vec{x})$ generating the imposed deformation. In general, such a displacement field may not exist. There are, however, suitable conditions under which the solution of this inverse problem is actually found. These conditions are written in the following compact form:

$$\eta_{qki}\eta_{phj} \frac{\partial^2 \epsilon_{ij}}{\partial x_k \partial x_h} = 0 \quad [12]$$

where η 's are the Levi-Civita permutation symbols (see Appendix). Equation [12] is known as an infinitesimal strain compatibility equation or a Beltrami Saint-Venant equation.¹⁸

The Concept of Stress

In continuum mechanics, we must consider two kinds of forces acting on a given region of a material body, namely body forces and surface forces.

Body forces depend on the external fields acting on the elastic body. They are described by the vector field $\vec{b}(\vec{x})$, representing their volume density. The total force $d\vec{F}_V$ applied to a small volume dV centered on the point \vec{x} is given by $d\vec{F}_V = \vec{b}(\vec{x})dV$. A typical example is given by the gravitational forces, proportional to the mass of the volume under consideration. In this case, we can write $d\vec{F}_V = \vec{g}dm$, where \vec{g} is the gravitational acceleration and dm is the mass of the volume dV . If we define $\rho = \frac{dm}{dV}$ as the density of the body, then we simply obtain $\vec{b}(\vec{x}) = \rho\vec{g}$.

Surface forces are concerned with the interaction between neighboring internal portions of deformable bodies. Although such an interaction results from the full set of interatomic forces, we can make the simplifying assumption that its overall effect can be represented adequately by a single vector field defined across the surface.

In principle, it is possible to introduce more complicated forces, such as volume and surface distributions of couples. However, the elastic behavior of most materials is adequately described by body and surface forces only. More advanced formulations, based on nonclassical or multipolar continuum theories, can be found elsewhere.²⁴

It is useful to introduce the following notation for the surface force $d\vec{F}_S$ applied to the area element dS :

$$d\vec{F}_S = \vec{f}dS \tag{13}$$

where \vec{f} assumes the meaning of a surface density of forces. The Cauchy theorem¹⁷ states that a tensor \hat{T} exists such that:

$$\vec{f} = \hat{T}\vec{n} \tag{14}$$

where \vec{n} is the external normal unit vector to the surface delimiting the portion of body subjected to the force field \vec{f} . The quantity \hat{T} has been called the *Cauchy stress tensor* or simply the *stress tensor*. The proof of this theorem is not trivial and can be found in any standard book on continuum mechanics.^{20,22} The forces applied to the area element, therefore, can be written in the following form:

$$d\vec{F}_S = \hat{T}\vec{n}dS \tag{15}$$

or, equivalently as $\frac{dF_{S,i}}{dS} = T_{ij}n_j$. We identify the stress tensor \hat{T} with a vector pressure. Typical stress values in solid mechanics range from MPa to GPa.

To better understand the physical meaning of the stress tensor, we consider the cubic element of volume shown in Figure 2, corresponding to an infinitesimal portion $dV = (dl)^3$ taken in an arbitrary solid body. The six faces of the

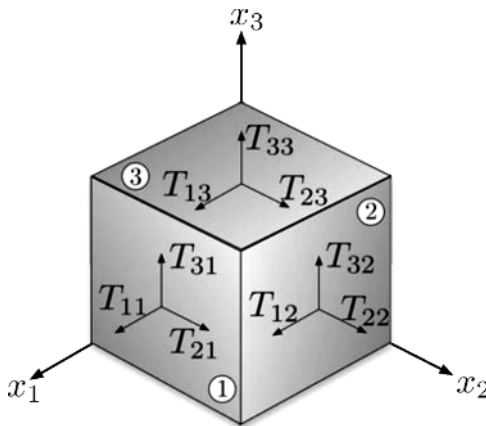


Figure 2 Geometrical representation of the stress tensor \hat{T} ; the T_{ij} component represents the pressure applied on the j th face of the cubic volume along the i th direction.

cube have been numbered as shown in Figure 2. We suppose that a stress \hat{T} is applied to that region; the T_{ij} component represents the pressure applied on the j th face along the i th direction.

The Formal Structure of Elasticity Theory

The relationships among the mathematical objects introduced in the previous sections represent the formal structure of the theory of elasticity (for small deformations).

The first two equations can be derived from the balance equations holding for the linear and angular momentum.^{16,17,21} In solid mechanics, the two key quantities are the linear and angular momentum densities for a continuum material system. We consider a portion V within a material body limited by the close surface S , and we define \vec{P} as its total linear momentum, \vec{F} as the resultant of the applied forces, \vec{L} as the total angular momentum, and \vec{M} as the resultant torque. The momentum balance equation of Newtonian dynamics $\frac{d\vec{P}}{dt} = \vec{F}$ for a portion V is written in the form:

$$\frac{d}{dt} \int_V \rho \frac{\partial u_j}{\partial t} d\vec{x} = \int_S T_{ji} n_i dS + \int_V b_j d\vec{x} \quad [16]$$

where we made use of body and surface forces as described in the previous section. The density of mass ρ is assumed to be constant and uniform under the small deformation assumption. By means of the Gauss divergence theorem, we get:

$$\frac{d}{dt} \int_V \rho \frac{\partial u_j}{\partial t} d\vec{x} = \int_V \frac{\partial T_{ji}}{\partial x_i} d\vec{x} + \int_V b_j d\vec{x} \quad [17]$$

Because the volume V is arbitrary, we easily obtain the following:

$$\frac{\partial T_{ji}}{\partial x_i} + b_j = \rho \frac{\partial^2 u_j}{\partial t^2} \quad [18]$$

which represents a first important relation. We turn now to the angular momentum balance equation $\frac{d\vec{L}}{dt} = \vec{M}$, which can be written in the following form:

$$\frac{d}{dt} \int_V \vec{x} \times \frac{\partial \vec{u}}{\partial t} \rho d\vec{x} = \int_S \vec{x} \times (\hat{T} \vec{n}) dS + \int_V \vec{x} \times \vec{b} d\vec{x} \quad [19]$$

As before, the surface integral can be simplified with the application of the Gauss divergence theorem as follows:

$$\int_S \vec{x} \times (\hat{T}\vec{n}) \, dS = \int_V \left[T_{kb} + x_b \frac{\partial T_{kp}}{\partial x_p} \right] \eta_{bkj} \vec{e}_j \, d\vec{x} \quad [20]$$

and we get:

$$\int_V \left\{ x_b \left[\frac{\partial^2 u_k}{\partial t^2} \rho - \frac{\partial T_{kp}}{\partial x_p} - b_k \right] - T_{kb} \right\} \eta_{bkj} \vec{e}_j \, d\vec{x} = 0 \quad [21]$$

Because of Eq. [18] we obtain $\int_V T_{kb} \eta_{bkj} \vec{e}_j \, d\vec{x} = 0$ or, equivalently, $T_{kb} \eta_{bkj} = 0$. This leads to:

$$T_{\hat{j}\hat{i}} = T_{\hat{j}\hat{i}} \quad [22]$$

This second fundamental equation states that the stress tensor is symmetric.

Equations [7], [12], [18], and [22] hold for most materials regardless of their constitution and microstructure. To complete the formal structure of the theory of elasticity, we need to introduce the specific constitutive equations, characterizing the elastic behavior of the material under investigation.^{10,25} They are written as follows:

$$T_{\hat{j}\hat{i}} = f(\{\epsilon_{\hat{i}\hat{j}}\}) \quad [23]$$

defining, at any point of the solid, a biunivocal correspondance between stress and strain. When a perfect elastic behavior is observed, the body relaxes back to its equilibrium configuration when applied forces are removed. In other words $\hat{T} = 0$ if and only if $\hat{\epsilon} = 0$. For most materials Eq. [23] is linear for small deformations. The following section is devoted to the study of the linear constitutive equations for both isotropic and anisotropic materials. The actual form of the constitutive equations cannot be determined within continuum mechanics; it is an input information of elasticity theory. Typically, it is determined experimentally²⁵ and formalized a posteriori.¹⁷ Once more, we remark that in this chapter we only concern ourselves with fully recoverable small deformations and point out that possible variations from a purely elastic behavior (e.g., plasticity) are treated elsewhere.²⁶

Constitutive Equations

Because of the symmetry of \hat{T} , the elastic stress–strain relation is defined by six relations of the form $T_{\hat{j}\hat{i}} = f(\{\epsilon_{\hat{i}\hat{j}}\})$, which are uniquely solvable for each different component of the strain. A thermoelastic material is one whose state

of stress depends on the present strain and on the temperature (or entropy). In what follows, we always assume that the temperature (or entropy) is constant so that, effectively, we have a pure stress–strain relationship.¹⁰

For most materials, Eq. [23] is linear if the strain is small.^{17,19} This corresponds to the generalized Hooke’s law, which has the following general form:

$$T_{ij} = C_{ijkl}\epsilon_{kl} \quad [24]$$

where C_{ijkl} are constants (for homogeneous materials). Equation [24] is of general validity, including all possible crystalline symmetries or, in other words, any kind of anisotropy. The fourth-rank tensor (with 81 components) of the elastic constants satisfies the following symmetry rules:

- Symmetry in the first pair of indices; because $T_{ij} = T_{ji}$, we have

$$C_{ijkl} = C_{jikl} \quad [25]$$

- Symmetry in the last pair of indices; because $\epsilon_{kl} = \epsilon_{lk}$, we have

$$C_{ijkl} = C_{ijlk} \quad [26]$$

- Symmetry between the first pair and the last pair of indices:

$$C_{ijkl} = C_{klij} \quad [27]$$

This result is easily proved if we suppose that an elastic energy density $U = U(\hat{\epsilon})$ exists as dependent only on the state of strain. From the energy density, we derive the constitutive relation $T_{ij} = \frac{\partial U(\hat{\epsilon})}{\partial \epsilon_{ij}}$ (just think about the case of the one-dimensional harmonic spring, where $U = \frac{1}{2}kx^2$ and $F = kx$). Drawing a comparison between the energy-based constitutive relation, $T_{ij} = \frac{\partial U(\hat{\epsilon})}{\partial \epsilon_{ij}}$ and Eq. [24] we simply obtain:

$$C_{ijkl} = \frac{\partial T_{ij}}{\partial \epsilon_{kl}} = \frac{\partial^2 U(\hat{\epsilon})}{\partial \epsilon_{kl} \partial \epsilon_{ij}} \quad [28]$$

The symmetry of the second-order derivative directly leads to Eq. [27].

According to these universal symmetry properties, C_{ijkl} has at most 21 independent components. Further reductions of the number of independent elastic constants depend on the possible crystalline symmetry of the material body.^{4,10}

The linear relation can be written in tensor compact form $\hat{T} = \hat{C}\hat{\epsilon}$, where the elastic tensor \hat{C} is called the *stiffness tensor*. We also introduce the inverse relation $\hat{\epsilon} = \hat{D}\hat{T}$ with $\hat{D} = \hat{C}^{-1}$. The new tensor \hat{D} is called the *compliance tensor*.

The Isotropic and Homogeneous Elastic Body

The paradigmatic system investigated by elasticity theory is the linear, isotropic, and homogeneous medium. The homogeneity property implies that the elastic behavior of the medium is the same in all its points; the stiffness and the compliance tensors are constant everywhere in the medium. The isotropy property implies that the mechanical response does not depend on the direction considered; stiffness or compliance tensors are invariant under arbitrary rotations. For a linear, isotropic, and homogeneous body, we will prove that only two elastic moduli are independent. They typically are called Lamé coefficients, and they are referred to as μ (shear modulus) and λ , respectively. Alternatively, we may use the Young modulus E and the Poisson ratio ν . A bulk modulus K can be used as well.

Let us now derive the constitutive equation for a linear, isotropic, and homogeneous elastic body. Because the stress tensor \hat{T} is symmetric, we can select a suitable reference frame in which \hat{T} is diagonal.¹⁴ In this reference frame, we refer to \hat{T}^* as the diagonal representation of \hat{T} , where the only components different from zero are T_{11}^* , T_{22}^* , and T_{33}^* . To begin, we consider the case of a uniaxial traction (i.e., an elongation) along the x_1 axis, which means $T_{11}^* \neq 0$, $T_{22}^* = 0$, and $T_{33}^* = 0$. For most materials, the experimental observation^{15,22} shows that the body will be elongated along the direction x_1 while it shrinks in the plane (x_2, x_3) . We can formalize this response by writing the linear relations:

$$\begin{aligned} \epsilon_{11}^* &= +\frac{1}{E}T_{11}^* \\ \epsilon_{22}^* &= -\frac{\nu}{E}T_{11}^* \\ \epsilon_{33}^* &= -\frac{\nu}{E}T_{11}^* \\ \epsilon_{12}^* = \epsilon_{23}^* = \epsilon_{31}^* &= 0 \end{aligned} \tag{29}$$

The Young modulus E describes the length variation along the direction x_1 , whereas the Poisson ratio ν describes the contractions in the two perpendicular directions. Of course, in these conditions, we cannot observe shear deformations.

When the diagonal stress \hat{T}^* assumes triaxial character, Eq. [29] easily can be generalized as:

$$\begin{aligned}\epsilon_{11}^* &= \frac{1}{E} [T_{11}^* - \nu (T_{22}^* + T_{33}^*)] \\ \epsilon_{22}^* &= \frac{1}{E} [T_{22}^* - \nu (T_{11}^* + T_{33}^*)] \\ \epsilon_{33}^* &= \frac{1}{E} [T_{33}^* - \nu (T_{22}^* + T_{11}^*)] \\ \epsilon_{12}^* &= \epsilon_{23}^* = \epsilon_{31}^* = 0\end{aligned}\quad [30]$$

The constitutive relations given in Eq. [30] are valid only in the reference frame where the stress tensor is diagonal. We remark that Eq. [30] can be written in the following, more compact, form:

$$\hat{\epsilon}^* = \frac{1}{E} [(1 + \nu)\hat{T}^* - \nu\hat{I} \text{Tr}(\hat{T}^*)] \quad [31]$$

If we make an arbitrary change of reference frame by means of a rotation matrix \hat{R} , then the stress tensor \hat{T}^* is transformed into \hat{T} , and the strain tensor $\hat{\epsilon}^*$ is transformed into $\hat{\epsilon}$ ($\hat{\epsilon} = \hat{R}^T \hat{\epsilon}^* \hat{R}$ and $\hat{T} = \hat{R}^T \hat{T}^* \hat{R}$).¹⁴ By means of such transformations, we obtain the isotropic constitutive equation in an arbitrary reference frame in the form:

$$\hat{\epsilon} = \frac{1}{E} [(1 + \nu)\hat{T} - \nu\hat{I} \text{Tr}(\hat{T})] \quad [32]$$

This is in fact the constitutive equation of a linear, isotropic, and homogeneous elastic material. Eq. [32] can be inverted, thus obtaining the stress tensor in terms of the strain tensor:

$$\hat{T} = \frac{E}{1 + \nu} \hat{\epsilon} + \frac{\nu E}{(1 + \nu)(1 - 2\nu)} \hat{I} \text{Tr}(\hat{\epsilon}) \quad [33]$$

We now introduce the Lamé coefficients, μ and λ , defined by the following relations:

$$\mu = \frac{E}{2(1 + \nu)} \quad \lambda = \frac{\nu E}{(1 + \nu)(1 - 2\nu)} \quad [34]$$

which, inserted into Eq. [33], provide the constitutive equation in its most popular form:

$$\hat{T} = 2\mu\hat{\epsilon} + \lambda\hat{I}\text{Tr}(\hat{\epsilon}) \quad [35]$$

Similarly, Eq. [32] also can be written in terms of the Lamé coefficients:

$$\hat{\epsilon} = \frac{1}{2\mu} \hat{T} - \frac{\lambda}{2\mu(2\mu + 3\lambda)} \hat{T} \text{Tr}(\hat{T}) \quad [36]$$

To introduce the bulk modulus K , we consider an hydrostatic stress described by the tensor:

$$\hat{T} = \begin{bmatrix} \sigma & 0 & 0 \\ 0 & \sigma & 0 \\ 0 & 0 & \sigma \end{bmatrix} \quad [37]$$

By means of Eq. [36], we easily obtain the corresponding state of strain:

$$\hat{\epsilon} = \frac{1}{3} \frac{1}{\lambda + \frac{2}{3}\mu} \sigma \hat{I} \quad [38]$$

This simple result allows us to define the bulk modulus K as follows:

$$K = \lambda + \frac{2}{3}\mu \quad [39]$$

Therefore, the stress–strain relation in hydrostatic condition can be summarized as $\hat{\epsilon} = \frac{1}{3K} \sigma \hat{I}$, where σ represents the (scalar) pressure applied to the system. The further relation $\text{Tr}(\hat{\epsilon}) = \frac{\sigma}{K}$ has an important physical interpretation; it describes the local volumetric variation under the assumption of hydrostatic stress.

To conclude, we observe that the stress–strain relation (Hooke’s law) for an isotropic elastic medium can be written in terms of any two independent material constants, chosen in the set λ, μ, K, E, ν . In Table 1 one can find all possible conversions among the defined elastic moduli. The elastic moduli E ,

Table 1 Relations Among the Different Elastic Moduli

	(λ, μ)	(K, μ)	(μ, ν)	(E, ν)	(E, μ)
λ		$K - \frac{2}{3}\mu$	$\frac{2\mu\nu}{1-2\nu}$	$\frac{\nu E}{(1+\nu)(1-2\nu)}$	$\frac{\mu(E-2\mu)}{3\mu-E}$
μ				$\frac{E}{2(1+\nu)}$	
K	$\frac{3\lambda+2\mu}{3}$		$\frac{2\mu(1+\nu)}{3(1-2\nu)}$	$\frac{E}{3(1-2\nu)}$	$\frac{E\mu}{3(3\mu-E)}$
E	$\frac{\mu(3\lambda+2\mu)}{\lambda+\mu}$	$\frac{9K\mu}{3K+\mu}$	$2(1+\nu)\mu$		
ν	$\frac{\lambda}{2(\lambda+\mu)}$	$\frac{3K-2\mu}{2(3K+\mu)}$			$\frac{E-2\mu}{2\mu}$

λ , μ , and K are measured in Pa, whereas the Poisson ratio ν is dimensionless being defined as a ratio between deformations.

Governing Equations of Elasticity and Border Conditions

When dealing with a linear, isotropic, and homogeneous material, the governing equations of the elasticity theory can be summarized by Eqs. [7], [18], and [35]. From these laws, we can obtain a new equation describing the time behavior of the displacement field during the deformation process as follows:

$$(\lambda + \mu) \vec{\nabla}(\vec{\nabla} \cdot \vec{u}) + \mu \vec{\nabla}^2 \vec{u} + \vec{b} = \rho \frac{\partial^2 \vec{u}}{\partial t^2} \quad [40]$$

which has been called the Lamé or Navier equation.^{17,22,27} To find a solution of Eq. [40], we must impose suitable boundary conditions, depending on the physical problem under consideration.^{21,28,29} In general, for three-dimensional problems we can fix either the displacement field at the surface of the elastic body (Dirichlet boundary conditions) or the stress applied on the same surface (Neumann boundary conditions). Mixed boundary conditions are possible as well.²² However, for the specific applications discussed later, we focus on those boundary conditions that convert a three-dimensional problem into an effective (and more simple) two-dimensional one.

We first introduce the *plane strain border condition*, which is considered to be a displacement field described by $u_1(x_1, x_2, x_3)$, $u_2(x_1, x_2, x_3)$, and $u_3(x_1, x_2, x_3)$. A state of plane strain is said to exist in a body if the displacement components take the form $u_1 = u_1(x_1, x_2)$, $u_2 = u_2(x_1, x_2)$, and $u_3 = 0$. In other words, these conditions are fulfilled if the displacement vector belongs to the plane x_1 , and x_2 , and if it does not depend on the coordinate x_3 . Of course, the definition of the plane strain conditions can be generalized to any arbitrarily oriented plane. It is easy to prove that the plane strain conditions impose the following relations on the strain tensor: $\epsilon_{33} = 0$, $\epsilon_{13} = 0$, and $\epsilon_{23} = 0$. The constitutive equations given in Eq. [33] take the following simplified form:

$$\begin{bmatrix} T_{11} \\ T_{22} \\ T_{12} \end{bmatrix} = \frac{E}{(1 + \nu)(1 - 2\nu)} \begin{bmatrix} 1 - \nu & \nu & 0 \\ \nu & 1 - \nu & 0 \\ 0 & 0 & 1 - 2\nu \end{bmatrix} \begin{bmatrix} \epsilon_{11} \\ \epsilon_{22} \\ \epsilon_{12} \end{bmatrix} \quad [41]$$

The inverse constitutive equation is therefore given by:

$$\begin{bmatrix} \epsilon_{11} \\ \epsilon_{22} \\ \epsilon_{12} \end{bmatrix} = \frac{1}{E} \begin{bmatrix} 1 - \nu^2 & -\nu(1 + \nu) & 0 \\ -\nu(1 + \nu) & 1 - \nu^2 & 0 \\ 0 & 0 & 1 + \nu \end{bmatrix} \begin{bmatrix} T_{11} \\ T_{22} \\ T_{12} \end{bmatrix} \quad [42]$$

The relation $T_{33} = \frac{E}{1+\nu} \frac{\nu}{1-2\nu} (\epsilon_{11} + \epsilon_{22})$ is not included in the previous sets, but it is still valid, and it can be useful for some applications.

We now introduce the *plane stress border condition*. A state of plane stress is said to exist when the stress tensor satisfies the property $\hat{T}\vec{n} = 0$ for a given unit vector \vec{n} in any point of the material. We consider \vec{n} parallel to the x_3 axis. It follows that $T_{33} = 0$, $T_{13} = 0$, and $T_{23} = 0$. Moreover we suppose that $T_{11} = T_{11}(x_1, x_2)$, $T_{22} = T_{22}(x_1, x_2)$, and $T_{12} = T_{12}(x_1, x_2)$. With these assumptions, the constitutive relation given in Eq. [32] can be simplified as follows:

$$\begin{bmatrix} \epsilon_{11} \\ \epsilon_{22} \\ \epsilon_{12} \end{bmatrix} = \frac{1}{E} \begin{bmatrix} 1 & -\nu & 0 \\ -\nu & 1 & 0 \\ 0 & 0 & 1 + \nu \end{bmatrix} \begin{bmatrix} T_{11} \\ T_{22} \\ T_{12} \end{bmatrix} \quad [43]$$

They can also be inverted as follows:

$$\begin{bmatrix} T_{11} \\ T_{22} \\ T_{12} \end{bmatrix} = \frac{E}{1-\nu^2} \begin{bmatrix} 1 & \nu & 0 \\ \nu & 1 & 0 \\ 0 & 0 & 1 - \nu \end{bmatrix} \begin{bmatrix} \epsilon_{11} \\ \epsilon_{22} \\ \epsilon_{12} \end{bmatrix} \quad [44]$$

As shown, the relation $\epsilon_{33} = -\frac{\nu}{E} (T_{22} + T_{11})$ is not included in the previous sets, but it too is still valid, and it can be useful for some applications.

It is important to observe that a simple formal substitution transforms Eqs. [43] and [44] for plane stress conditions into the corresponding Eqs. [41] and [42] for plane strain condition. In fact, if we consider in Eqs. [43] and [44] the change of variables $E \rightarrow \frac{E}{1-\nu^2}$ and $\nu \rightarrow \frac{\nu}{1-\nu}$, we obtain Eqs. [41] and [42] exactly. This property is very useful in many practical applications.

Elastic Energy

In general, the constitutive equation of an elastic material can be derived by the strain energy function by means of the relation:²²

$$T_{ij} = \frac{\partial U(\hat{\epsilon})}{\partial \epsilon_{ij}} \quad [45]$$

We consider a linear elastic body described by the constitutive relation given in Eq. [24]. It is possible to obtain the explicit form of its energy density U in terms of the strain tensor. From the following relation:

$$\frac{dU}{dt} = \frac{\partial U}{\partial \epsilon_{ij}} \frac{d\epsilon_{ij}}{dt} = T_{ij} \frac{d\epsilon_{ij}}{dt} \quad [46]$$

giving the rate of change of the energy density during a time-dependent deformation, we obtain:

$$\frac{dU}{dt} = C_{ijkb} \epsilon_{kb} \frac{d}{dt} \epsilon_{ij} \quad [47]$$

which, by using the symmetry given in Eq. [27], can be written as follow:

$$\frac{dU}{dt} = \frac{1}{2} C_{ijkb} \frac{d}{dt} (\epsilon_{ij} \epsilon_{kb}) \quad [48]$$

It follows that the energy density can be placed in the very general form:

$$U = \frac{1}{2} C_{ijkb} \epsilon_{ij} \epsilon_{kb} \quad [49]$$

This expression can be simplified further when the material is linear, isotropic, and homogeneous. Indeed, it assumes the very compact form:¹⁰

$$U(\hat{\epsilon}) = \frac{1}{2} T_{ij} \epsilon_{ij} = \mu \epsilon_{ij} \epsilon_{ij} + \frac{1}{2} \lambda \epsilon_{kk} \epsilon_{ii} \quad [50]$$

where we have made use of the Lamé coefficients defined in a previous section. Because $\epsilon_{kk} = \epsilon_{ii} = \text{Tr}(\hat{\epsilon})$ and $\epsilon_{ij} \epsilon_{ij} = \text{Tr}(\hat{\epsilon}^2)$, we obtain the following final tensor form:

$$U(\hat{\epsilon}) = \mu \text{Tr}(\hat{\epsilon}^2) + \frac{1}{2} \lambda [\text{Tr}(\hat{\epsilon})]^2 \quad [51]$$

which represents the elastic energy density for an isotropic material.

For an elastic solid body at equilibrium (i.e., for $\epsilon_{ij} = 0 \ \forall i, j$) the function $U(\hat{\epsilon})$ must exhibit a minimum (i.e., the equilibrium configuration is stable). Because $U(\hat{\epsilon} = 0) = 0$, we conclude that the quadratic form defined in Eqs. [49] or [51] is positive definite. In other words, we have proved that the stiffness and the compliance tensors are always positive definite for real materials. We search for the specific conditions assuring a positive definite energy density for an isotropic material. To this aim, we apply a deformation satisfying the relation $\epsilon_{ii} = 0$, leading to $U = \mu \epsilon_{ij} \epsilon_{ij} > 0$ or, equivalently, $\mu > 0$. Moreover, if we apply a hydrostatic deformation $\epsilon_{ij} = s \delta_{ij}$, where s is a constant, we obtain $U = 3s^2 (3\lambda/2 + \mu) > 0$ or, equivalently, $3\lambda + 2\mu > 0$. By means of Table 1 we obtain the additional relations $K > 0$ and $E > 0$. Finally, by means of the expression $\nu = \frac{3K-2\mu}{2(3K+\mu)}$, we easily can prove that $-1 < \nu < \frac{1}{2}$. It is interesting to observe that the last result admits negative values for the Poisson ratio. This point was considered controversial for a long time. In fact, standard natural

materials exhibit a nonnegative Poisson ratio, meaning that all traditional materials, when elongated in a given direction, always display a shrinking in the transverse (perpendicular) directions. However, during the last decades, many composite and complex materials have been realized with negative values of the Poisson ratio.^{30–32} Hence, when elongated in a given direction, these materials show an unconventional extension in the transverse directions. Although intriguing, this phenomenon, as proved, does not violate thermodynamics.

MICROSCOPIC THEORY OF ELASTICITY

Conceptual Layout

This section represents a tutorial introduction to the atomistic theory of elasticity in which the macroscopic elastic properties of a material are obtained by explicitly taking into account its atomic-scale structure and the fundamental interactions among its constituents. Although this subject has been widely investigated in the past,⁸ the connection between the continuum and the atomistic approach still remains a topic of crucial importance in modern materials science.

We develop an atomistic version of the elasticity theory for an isotropic and homogeneous material, and we establish the minimum level of complexity that any microscopic model of atomic interactions must exploit to obtain results consistent with the continuum theory. In particular, we will examine two situations: a two-dimensional triangular lattice with two-body interactions and a two-dimensional triangular lattice with both two-body and three-body interactions. Such a case study is paradigmatic under two remarkably important standpoints. On the one hand, the two-dimensional (perfect) triangular lattice is the only (homogeneous) isotropic crystal structure; therefore, it represents the simplest crystalline counterpart of the continuum medium discussed in the previous section. On the other hand, by considering either a two-body or a more sophisticated force field, we can understand the role of the microscopic interaction model in predicting elastic features. Either way, we remark that our conclusions will be of general validity, although our arguments are developed for two-dimensional crystals only. We will prove that two-body force fields provide an elastic picture that is not consistent with continuum mechanics because they describe the elastic behavior of the material with only one elastic modulus. On the contrary, force fields including both two-body and three-body interactions provide results in formal agreement with continuum elasticity theory (i.e., they predict the existence of two independent elastic constants.)

In the second part of this section, we introduce some typical interaction potentials used in molecular dynamics simulations. In particular, we will elaborate a general conceptual framework that can be used to generate improved force fields for applications in the realm of solid mechanics.

Finally, we work out the complete theory for the calculation of the stress tensor at the atomic scale. We will discuss finite temperature effects extensively, and we will address some important conceptual and technical issues, which are tricky and often cause incorrect implementations of stress calculations.

Triangular Lattice with Central Forces Only

We begin by considering an arbitrary lattice of point masses that interact through simple central forces (two-body interaction), acting between nearest neighbors only. We focus on a pair of particles placed in positions $\vec{r}_1^{(0)}$ and $\vec{r}_2^{(0)}$ at equilibrium or, equivalently, in a configuration of minimum energy. If a small deformation is applied, then the new positions will be given by:

$$\vec{r}_i = \vec{r}_i^{(0)} + \vec{u}(\vec{r}_i^{(0)}) \quad [52]$$

where, according to Eq. [3] we have introduced the displacement vector field $\vec{u}(\vec{r}_i^{(0)})$ for any equilibrium lattice site. We further assume that the two-body interaction may be represented by a harmonic spring of constant k_s . If the particles in \vec{r}_1 and \vec{r}_2 are nearest neighbors, then the force on the first particle resulting from the second one is:

$$\vec{F}_1^{2B} = k_s \vec{n} (|\vec{r}_2 - \vec{r}_1| - l) \quad [53]$$

where $l = |\vec{r}_2^{(0)} - \vec{r}_1^{(0)}|$ is the equilibrium distance and \vec{n} is the unit vector in the direction of the central force (see Figure 3 for details). This force corresponds to a two-body interaction potential energy $U^{2B} = (1/2)k_s (|\vec{r}_2 - \vec{r}_1| - l)^2$. By

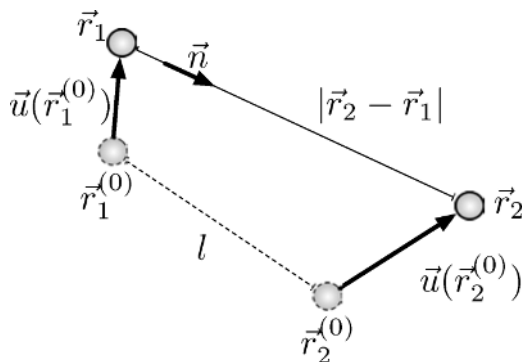


Figure 3 Displacement (\vec{u}) and distance (\vec{r}) vectors for a pair of atoms before (this configuration is labelled by suffix $^{(0)}$) and after deformation. The unit vector \vec{n} along the direction of the central force acting between atoms 1 and 2 is shown as well.

assuming slow variations of the displacement over the atomic scale (this is actually the case of deformations as a result of applied loads at the macroscale), we can expand this force up to the first order in the difference $\vec{u}(\vec{r}_2^{(0)}) - \vec{u}(\vec{r}_1^{(0)})$. Then, writing:

$$\vec{u}(\vec{r}_2^{(0)}) = \vec{u}(\vec{r}_1^{(0)}) + \left[\frac{\partial \vec{u}}{\partial \vec{r}} \right] (\vec{r}_2^{(0)} - \vec{r}_1^{(0)}) \quad [54]$$

we obtain:

$$\vec{F}_1^{2B} = k_s l \vec{n} \left(\vec{n} \times \left[\frac{\partial \vec{u}}{\partial \vec{r}} \right] \vec{n} \right) \quad [55]$$

Finally, defining the strain tensor as in Eq. [7] we find:

$$\vec{F}_1^{2B} = k_s l \vec{n} (\vec{n} \times \hat{\epsilon} \vec{n}) \quad [56]$$

This is the force acting on a given particle caused by a neighboring atom, placed at distance l and aligned in direction \vec{n} , when the local deformation is characterized by the strain tensor $\hat{\epsilon}$. In this derivation, we have implicitly assumed the Cauchy–Born rule³ stating that, within a body under a small strain, the positions of the atoms follow the overall deformation of the material. This approximation generally holds for face-centered cubic and body-centered cubic crystals (in general for Bravais lattices), whereas for lattices with a basis of two (or more) atoms in the unit cell, the rule has to be modified to allow for internal degrees of freedom between the sublattices.

We now apply the result given in Eq. [56] to the specific case of the two-dimensional triangular lattice shown in Figure 4 and representing the only case

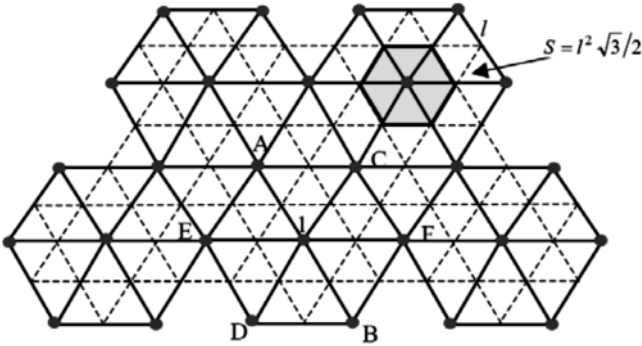


Figure 4 Planar (two-dimensional) triangular crystal with lattice constant l . One easily can find the area S of the unit cell and the six first-next-neighbors A, B, C, D, E, and F of atom 1.

of isotropic crystal. Any particle has six nearest neighbors placed at distance l (corresponding to the edge of the triangular mesh). By computing the force caused by the opposite neighbors A and B of atom 1, we find $\vec{F}_{1,AB}^{2B} = k_s l \vec{n} \times (\hat{e}_A - \hat{e}_B) \vec{n}$ where we indicated the unit vector connecting A to B with \vec{n} . The total force on atom 1 is given by the sum of three terms calculated along the three directions A-B, C-D, and E-F (see Figure 4). To match the continuum formalism, we must divide the total force by $S = l^2 \sqrt{3}/2$, namely by the area occupied by each atom. The resulting force density is:

$$\vec{f}_{1,AB}^{2B} = \frac{2\sqrt{3}}{3} k_s \vec{n} \times \frac{(\hat{e}_A - \hat{e}_B) \vec{n}}{l} \vec{n} \quad [57]$$

The ratio $\frac{1}{l} (\hat{e}_A - \hat{e}_B)$ in Eq. [57] is identified with the projection $(\vec{n} \times \partial/\partial\vec{r}) \hat{e}$ of the gradient of the strain tensor. Therefore, the total force from the couple AB is written as:

$$\vec{f}_{1,AB}^{2B} = \frac{2\sqrt{3}}{3} k_s \vec{n} \times (\vec{n} \times \partial/\partial\vec{r}) \hat{e} \vec{n} \quad [58]$$

Finally, the Newtonian law describing the motion of atom 1 is obtained as $\vec{f}_{1,AB}^{2B} + \vec{f}_{1,CD}^{2B} + \vec{f}_{1,EF}^{2B} + \vec{b} = \rho \ddot{\vec{u}}$, where \vec{b} is the density of external forces applied to the system, ρ is the mass density and $\ddot{\vec{u}}$ is the acceleration. Each force term can be developed through the Eq. [58], leading to the final elasticity equation:

$$\frac{\sqrt{3}}{4} k_s [\nabla^2 \vec{u} + 2\nabla (\nabla \times \vec{u})] + \vec{b} = \rho \ddot{\vec{u}} \quad [59]$$

By comparing Eq. [59] to Eq. [40], we obtain the effective elastic moduli of the triangular lattice:

$$\lambda = \mu = \frac{\sqrt{3}}{4} k_s \quad [60]$$

or, equivalently, the Young modulus and the Poisson ratio:

$$E = \frac{5\sqrt{3}}{8} k_s \quad \text{and} \quad \nu = \frac{1}{4} \quad [61]$$

Eqs. [60] and [61] prove that an atomistic model for the triangular lattice with first next-neighbors central forces only, cannot take into account all the elastic features predicted by the continuum elastic theory (and confirmed experimentally). In particular, Eq. [60] indicates that, according to this model, the material should have only one characteristic elastic constant, whereas Eq. [61] implies

that a universal value of the Poisson ratio should exist independent of the actual physical properties of the material.

Triangular Lattice with Two-Body and Three-Body Interactions

We now consider a more refined force field, including three-body interactions among nearest neighbors. In this case, we begin by defining a potential function involving three atomic positions \vec{r}_1 , \vec{r}_2 , and \vec{r}_3 . We assume that the three angles ϑ_1 , ϑ_2 , and ϑ_3 (see Figure 5) are equal to α_1 , α_2 , and α_3 , respectively, at equilibrium.

Therefore, we can choose a potential energy of the form:

$$U^{3B} = \frac{1}{2} \left\{ H_1 [\cos \vartheta_1 - \cos \alpha_1]^2 + H_2 [\cos \vartheta_2 - \cos \alpha_2]^2 + H_3 [\cos \vartheta_3 - \cos \alpha_3]^2 \right\} \quad [62]$$

where H_1 , H_2 , and H_3 are suitable constants. For a triangular lattice, we have $\alpha_1 = \alpha_2 = \alpha_3 = \pi/3$ and, therefore:

$$U^{3B} = \frac{1}{2} b l^2 \left\{ \left[\cos \vartheta_1 - \frac{1}{2} \right]^2 + \left[\cos \vartheta_2 - \frac{1}{2} \right]^2 + \left[\cos \vartheta_3 - \frac{1}{2} \right]^2 \right\} \quad [63]$$

where, for simplicity, we set $H_1 = H_2 = H_3 = b l^2$, with l being the interatomic distance in the unstrained lattice. In such a way, the constant k_s (describing the two-body interactions) and the constant b (describing the three-body interactions) usefully assume the same physical units.

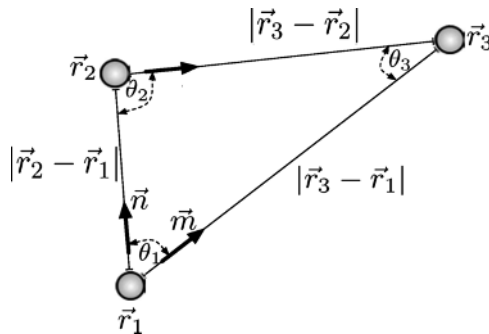


Figure 5 Distances and angles for a three-atom cluster. The unit vector \vec{n} (\vec{m}) in the direction of the central force acting between atoms 1 and 2 (1 and 3) is shown as well.

By applying the same approximations used to derive Eq. [56], we find the following net force on atom 1:

$$\begin{aligned} \vec{F}_1^{3B} = \frac{3}{2}hl \left\{ \left(\vec{m} \times \hat{\epsilon} \vec{n} + \frac{1}{2} \vec{m} \times \hat{\epsilon} \vec{m} - \vec{n} \times \hat{\epsilon} \vec{n} \right) \vec{m} \right. \\ \left. + \left(\vec{m} \times \hat{\epsilon} \vec{n} + \frac{1}{2} \vec{n} \times \hat{\epsilon} \vec{n} - \vec{m} \times \hat{\epsilon} \vec{m} \right) \vec{n} \right\} \end{aligned} \quad [64]$$

where \vec{m} and \vec{n} are the unit vectors defined in Figure 5. We remark that the bilinear form $\vec{m} \times \hat{\epsilon} \vec{n}$ is directly connected to the variation of the angle between \vec{m} and \vec{n} , induced by the deformation described by $\hat{\epsilon}$. As expected, the force term given in Eq. [64] depends on the angular distortion of the triangle represented in Figure 5. Moreover, if ϑ_2 and ϑ_3 are equal, then the force is oriented along the bisector of the angle ϑ_1 in such a way to increase ϑ_1 if $\vartheta_1 < \pi/3$ and to decrease ϑ_1 if $\vartheta_1 > \pi/3$.

By adopting the angular-dependent force defined in Eq. [64], we can itemize the full set of forces at work as follows: (1) two-body interaction forces, as given in Eq. [57]; (2) three-body interaction forces: six angular terms are working on atom 1 of Figure 4, as calculated in Eq. [64] (they correspond to the angles A1C, C1F, F1B, B1D, D1E, and E1A); (3) the external forces applied to the lattice. Following the same procedure outlined in the previous section, we get:

$$\frac{3}{4} \left(\frac{\sqrt{3}}{3} k_s + \frac{9}{4} h \right) \nabla^2 \vec{u} + \frac{\sqrt{3}}{2} k_s \nabla (\nabla \times \vec{u}) + \vec{b} = \rho \ddot{\vec{u}} \quad [65]$$

By comparing Eq. [65] to Eq. [40] we easily find the effective elastic moduli of the lattice:

$$\lambda = \frac{3}{4} \left(\frac{\sqrt{3}}{3} k_s - \frac{9}{4} h \right) \quad \text{and} \quad \mu = \frac{3}{4} \left(\frac{\sqrt{3}}{3} k_s + \frac{9}{4} h \right) \quad [66]$$

or, equivalently, the Young modulus and the Poisson ratio:

$$E = \frac{3\sqrt{3}}{8} k_s \left(\frac{\sqrt{3}}{3} + \frac{9}{4} \frac{h}{k_s} \right) \left(\frac{5\sqrt{3}}{3} - \frac{9}{4} \frac{h}{k_s} \right) \quad \text{and} \quad \nu = \frac{1}{4} - \frac{9\sqrt{3}}{16} \frac{h}{k_s} \quad [67]$$

In conclusion, only this improved lattice model can correctly describe the elastic behavior of any isotropic media because it provides the atomistic expression for *both independent* elastic constants. In other words, we can state that at least three-body interactions are mandatory to reproduce the complex mechanical behavior of real isotropic materials accurately.

Finally, we introduce some energetic considerations. The Lamé constants must obey the inequalities $\mu > 0$ and $2\mu + 3\lambda > 0$. Consequently, the interaction parameters k_s and h must be as follows: $k_s > 0$ and $-\frac{4\sqrt{3}}{27}k_s < h < \frac{20\sqrt{3}}{27}k_s$. When h approaches the value $-\frac{4\sqrt{3}}{27}k_s$, the Poisson ratio becomes equal to 1/2 (a situation found in rubbery materials); the system is *volume (area) preserving* because the three-body interactions are working contrarily ($h < 0$) to what is expected. On the other hand, when h approaches the value $\frac{20\sqrt{3}}{27}k_s$, the Poisson ratio has the value of -1 (a situation common in some *reentrant polymer foams*):³⁰ in this case, the structure is *shape preserving*, allowing only deformations described by isotropic rescaling of the body.

In our approach, we considered some hypotheses to simplify the mathematical complexity of the interaction models. The main assumptions are summarized as follow: (1) we described only two-dimensional systems; (2) the interaction potentials are linear (springs); (3) their action is limited to between nearest neighbors only; (4) we have analyzed simple Bravais lattices where internal strains do not occur. Nevertheless, the final conclusions about the primary importance of the three-body interactions for obtaining the correct number of independent elastic constants can be applied to arbitrary crystals (in three dimensions) with arbitrarily nonlinear and long-range interaction potentials.

In many earlier publications, the method of homogeneous deformations was used to derive expressions analytically for the elastic constants of a crystalline solid in which the energy density can be separated into contributions from many-body interactions of a different order.^{33,34} For example, the exact explicit expressions for the body-centered cubic lattice³⁵ and for hexagonal closed packing lattice^{36,37} have been derived for an arbitrary many-body interatomic potential. In these complicated expressions, if we reset the three-body interaction (and higher order multibody terms) to zero, we then obtain a reduction in the number of independent elastic constants, confirming our predictions. We remark, however, that this result is valid only if we determine the elastic constants of the crystalline structure in the reference equilibrium configuration (i.e., when the external pressure applied to the body is exactly reset to zero). In a recent publication,³⁸ the two-dimensional triangular lattice with two-body (arbitrarily nonlinear and long-range) interactions was studied under an external pressure P , and it was proven that the lattice can show a negative Poisson ratio behavior, as long as certain conditions involving the two-body interaction potential are satisfied. The result is given by the relation:³⁸

$$\nu(P) = \frac{1 + 2PK_T}{4} \quad [68]$$

where $P = -\frac{dU}{dV}$ is the applied pressure and $K_T = -\frac{1}{V}\frac{dV}{dP}$ is the compressibility (U is the total energy and V is the volume of the body). If we let $P = 0$ in Eq. [68] we obtain the value of the Poisson ratio given in Eq. [61]. Therefore, Eq. [61]

is exact also with nonlinear and long-range interaction potentials. Moreover, Eq. [68] shows that with $P < 0$ we can obtain a negative Poisson ratio.

Interatomic Potentials for Solid Mechanics

In computational atomic-scale solid mechanics, it is important to use interatomic interaction potentials that can correctly describe arbitrary configurations (which may significantly differ from the perfect crystalline one) or systems possibly subjected to large deformations. The development of accurate and predictive representations of the interaction forces is an open and active research field.

An accurate description of interatomic forces can be achieved by ab initio quantum mechanical methods. They are more fundamental and often superior with respect to empirical force fields. Such methods are nevertheless computationally very demanding, so their use is limited to a relatively small number of atoms (typically < 1000), which is not large enough to investigate many important problems in the physics of brittle solids (e.g., crack initiation, crack propagation, and fiber toughening). Rather, ab initio methods have been applied successfully to study specific aspects of brittle fracture (including surface energies, surface reconstructions, and quasi-static separation of semi-bulks), relegating the development of the more general picture to empirical methods. Alternatively, ab initio schemes have been used in combination with less computationally demanding models according to the multiscale paradigm.

In this review, we focus on empirical potentials, thus allowing a direct approach to brittle fracture; we are motivated in this choice by the observation that, so far, most molecular dynamics applications to fracture have relied on empirical potentials. It has been shown recently that most of the problems found when using model potentials are a result of an unsuitable choice of the interaction range.³⁹ Several possible solutions to bypass this bottleneck have been proposed in the literature to extend the use of model potentials. This critical issue is discussed extensively below.

The simplest interatomic potential is obtained by taking into account only two-body interactions:

$$U = \sum_{\alpha < \beta} U^{2B}(x_{\alpha\beta}) \quad [69]$$

As explained earlier, such a two-body interaction is not sound enough for simulations in the realm of solid mechanics. However, it can be used in this field when simple, qualitative, and paradigmatic computations must be performed on very large systems. This is the case of the renowned Lennard—Jones potential, originally developed for describing the properties of gases. In this model, two distinct forces are considered in the interaction between two atoms: in the

limit of a large separation an attractive force (van der Waals force, or dispersion force) and a repulsive force at short ranges (the result of overlapping electron orbitals). The Lennard-Jones potential (also referred to as the L-J potential or 6-12 potential) was proposed in 1924 by John Lennard-Jones.⁴⁰ It assumes the form:

$$U^{2B}(r) = 4\epsilon \left[\left(\frac{\sigma}{r} \right)^{12} - \left(\frac{\sigma}{r} \right)^6 \right] \quad [70]$$

where ϵ is the depth of the potential well, σ is the distance at which the interparticle potential is zero, and r is the distance between the particles. The $(1/r)^{12}$ term describes repulsion and the $(1/r)^6$ term describes attraction.

The L-J potential is particularly accurate for describing a noble gas. Concerning condensed matter, the L-J can describe, at a qualitative level, the physics of metals with a close-packed crystalline structure. As a matter of fact, the lowest energy arrangement of an infinite number of atoms is the hexagonal close-packing. Upon raising the temperature, the lowest free energy arrangement becomes cubic close packing and then liquid. Under pressure, the lowest energy structure switches between cubic and hexagonal close packing.⁴¹ Accordingly the applicability of the L-J model for brittle solids is limited; nevertheless, it has been applied successfully to study the brittle-to-ductile transition in simple metals⁴² and the dynamics of brittle fracture⁴³ among other uses.

To achieve more realistic interatomic force models, it is necessary to go beyond the two-body approximation. An important example is the Stillinger-Weber (SW) potential, which was developed to describe covalently bonded silicon.⁴⁴ The SW potential takes into account both two-body and three-body terms:

$$U = \sum_{\alpha < \beta} U^{2B}(x_{\alpha\beta}) + \sum_{\alpha < \beta < \gamma} U^{3B}(\vec{x}_\alpha, \vec{x}_\beta, \vec{x}_\gamma) \quad [71]$$

where \vec{x}_α is the position of the α -th atom and $x_{\alpha\beta} = |\vec{x}_\alpha - \vec{x}_\beta|$. The potential terms for two-body interactions can be written as $U^{2B}(x_{\alpha\beta}) = \epsilon f_2(x_{\alpha\beta}/\sigma)$ and $U^{3B}(\vec{x}_\alpha, \vec{x}_\beta, \vec{x}_\gamma) = \epsilon f_3(\vec{x}_\alpha/\sigma, \vec{x}_\beta/\sigma, \vec{x}_\gamma/\sigma)$. The function f_2 is given by:

$$f_2(r) = A (Br^{-p} - r^{-q}) \exp \left[(r - a)^{-1} \right] \quad [72]$$

if $r < a$ and $f_2 = 0$ if $r > a$, where A, B, p, q and a are positive constants. The three-body term is expressed can follow:

$$f_3(\vec{x}_\alpha, \vec{x}_\beta, \vec{x}_\gamma) = h(x_{\beta\alpha}, x_{\beta\gamma}, \theta_{\alpha\beta\gamma}) + h(x_{\alpha\beta}, x_{\alpha\gamma}, \theta_{\beta\alpha\gamma}) + h(x_{\gamma\alpha}, x_{\gamma\beta}, \theta_{\alpha\gamma\beta}) \quad [73]$$

where $\theta_{\alpha\beta\gamma}$ is the angle between \vec{x}_α and \vec{x}_γ subtended at vertex β and

$$h(x_{\beta\alpha}, x_{\beta\gamma}, \theta_{\alpha\beta\gamma}) = \lambda \exp \left[\xi (x_{\beta\alpha} - a)^{-1} + \xi (x_{\beta\gamma} - a)^{-1} \right] \times \left(\cos \theta_{\alpha\beta\gamma} + \frac{1}{3} \right)^2 \quad [74]$$

where λ and ξ are constants. The object of the three-body component of the potential is to enforce the tetrahedral bond angle (109.47°) among triplets of bonded atoms. This model has been developed for describing interactions in solid and liquid forms of Si, but it seems only moderately accurate to describe the amorphous phase.⁴⁵ Deficiencies of the SW force model, furthermore, are found when studying the brittle cleavage of silicon.⁴⁶

To improve the reliability of the models and to extend their applicability to configurations far from equilibrium, it is possible to use higher order (up to five-body) expansion terms.⁴⁷ Despite the increased complexity, similar models improve only selectively the description of the solid system and often at a considerable increase of the computational cost.

A computationally more convenient approach is to use an environment dependent interatomic potential (EDIP).^{48,49} The interaction model includes only two-body and three-body terms as is the case of the SW model, but in addition, it has an explicit dependence on the local atomic environment through an effective coordination number

$$Z_\alpha = \sum_{\gamma \neq \alpha} f(x_{\alpha\gamma}) \quad [75]$$

where $f(x_{\alpha\gamma})$ is a cut-off function that measures the contribution of neighbor γ to the coordination of atom α in terms of the separation $x_{\alpha\gamma}$. For silicon,^{48,49} the environment-dependent formulation can successfully capture (1) the energetics and elastic properties of the ground-state diamond lattice, (2) the covalent rehybridization of undercoordinated atoms, and (3) a smooth transition to metallic bonding for overcoordinated atoms. Unfortunately, the EDIP potential cannot reproduce the brittle cleavage in silicon.⁴⁶

The primary importance of the local coordination Z_α to describe bonding in solids properly first was pointed out by Abell.⁵⁰ In fact, it can be shown by quantum-mechanic arguments that the more neighbors an atom has, the weaker the bond to each neighbor will be. Abell proposed an interatomic potential formed by a sum over nearest neighbors two body terms in the form:

$$U = \frac{1}{2} \sum_{\alpha \neq \beta} [f_r(x_{\alpha\beta}) + b_{\alpha\beta} f_a(x_{\alpha\beta})] \quad [76]$$

where $f_r(r_{\alpha\beta})$ and $f_a(r_{\alpha\beta})$ are pair-additive repulsive and attractive interactions, respectively. The bond strength $b_{\alpha\beta}(Z_\alpha)$ (also named bond order) is a monotonically decreasing function of the coordination number $b_{\alpha\beta} \sim Z_\alpha^{-\frac{1}{2}}$. With Morse-type repulsive and attractive pair interactions:

$$f_r(r) = A \exp(-\lambda_1 r) \quad [77]$$

$$f_a(r) = -B \exp(-\lambda_2 r) \quad [78]$$

Eq. [76] yields an energy versus volume relationship similar to the universal binding energy curve for solids⁵¹ (see “Universal Energy Relation” on page 33). Furthermore, at variance with a simple two-body potential, by using the bond order b_{ij} environment dependence, it is possible to reproduce both the open (e.g., diamond) or close-packed crystalline structures, depending on the actual choice of the parameters. This point is crucial for determining the equilibrium state of a crystal structure.

Recognizing the utility of the Abell’s approach, Tersoff proposed a model for Si, Ge, C, and SiC by taking into account the environmentally dependent bond strength.⁵² In Tersoff formulation, the total energy is:

$$U = \frac{1}{2} \sum_{\alpha \neq \beta} f_c(x_{\alpha\beta}) [f_r(x_{\alpha\beta}) + b_{\alpha\beta} f_a(x_{\alpha\beta})] \quad [79]$$

where a cut-off function is introduced to limit the sum over nearest neighbors:

$$f_c(r) = \begin{cases} 1 & r < R - D \\ \frac{1}{2} - \frac{1}{2} \sin[\pi(r - R)/D] & R - D < r < R + D \\ 0 & r > R + D \end{cases} \quad [80]$$

The bond-order parameter $b_{\alpha\beta}$ is given by:

$$b_{\alpha\beta} = (1 + \beta \zeta_{\alpha\beta}^n)^{-1/(2n)} \quad [81]$$

with

$$\zeta_{\alpha\beta} = \sum_{\gamma \neq \alpha, \beta} f_c(x_{\alpha\gamma}) g(\theta_{\alpha\beta\gamma}) \exp[\lambda_3^3 (x_{\alpha\beta} - x_{\alpha\gamma})^3] \quad [82]$$

$$g(\theta) = 1 + \frac{c^2}{d^2} - \frac{c^2}{d^2 + (h - \cos \theta)^2} \quad [83]$$

The function $b_{\alpha\beta}$ is a measure of the bond order, and it is assumed to be a monotonically decreasing function of the coordination of atoms α and β . In

addition, terms that act to limit the range of interaction to the first neighbor shell are included in $b_{\alpha\beta}$. This model can be modified to describe multicomponent mixtures and, more specifically, SiC and SiGe mixtures.

In 1990,⁵³ Brenner extended the analytic form of the Tersoff potential by introducing two additional ad hoc terms into the bond order to counter the overbinding of radicals. A second-generation Brenner potential⁵⁴ leads to a significantly better description of bond energies, lengths, and force constants for hydrocarbon molecules, as well as elastic properties of diamond. This prominent model has been applied successfully in several atomic scale studies of complex processes involving hydrocarbon molecules, graphite, graphene, and diamond lattice.

Improved bond order model potentials for hydrocarbons, that can be derived from quantum-mechanical treatment of bond order, are possible.⁵⁵ Such refinements are not necessary when describing the brittle behavior of solid systems. From this perspective, it has been proved^{39,56} that a central issue is the choice of the interaction range (i.e., the cut-off function) employed in the model potentials. The use of an environmentally dependent interaction range has been proposed recently to cure substantially the deficiencies of the Brenner-type model potentials. An extensive discussion of the interaction range necessary to study brittle materials is reported in the next section.

Interatomic Potentials and Brittle Materials

In this section, we discuss some very basic and important features relevant to developing improved potentials for applications in nanomechanics. We will focus on the atomistic simulation of brittle materials (Si, Ge, C, and SiC), which turned out to be a very challenging problem; as a matter of fact, most available potentials for elemental as well as compound group-IV materials cannot reproduce the brittle nature of crack propagation.⁴⁶ In the case of silicon, this holds for the Tersoff potential,⁵⁷ the SW potential,⁵⁸ and for the EDIP potential.⁵⁹ All of them predict nonphysical behavior during fracture. Only a few force field models can predict the brittle fracture in covalent materials.^{51,60,61}

The origin of the deficiencies of most potentials in describing brittleness first was analyzed by Holland and Marder.⁴⁶ They concluded that none of the available models for silicon describes the force-separation curve accurately. This conclusion was obtained by comparing the atomic force provided by SW and EDIP potentials with the universal energy relation (UER) obtained by ab initio calculations.⁵¹ Here, we extend the analysis of Holland and Marder, and we identify the minimal conditions that a model potential must satisfy to describe brittle solids. In particular, we focus on the role of the interaction range. By following the general conclusions outlined in the previous section (namely, the need of many-body interactions and relatively long-ranged forces), here it is investigated how a valid and efficient potential indeed can be generated. The argument is illustrated by using the bond order Tersoff potential as the

prototype for interaction models for group-IV materials and by comparing its predictions with the UER obtained by ab initio calculations.⁵¹

Universal Energy Relation

The UER⁵¹ is a two-parameter equation of state describing the variation of the internal energy $U(s)$ of a solid upon the scaled interatomic separation (hereafter referred to as s):

$$U(s) = -E_0 (1 + s) e^{-s} \tag{84}$$

where E_0 is the the cohesive energy per atom (absolute value) and s is:

$$s = \left(\frac{r}{r_0} - 1 \right) \frac{1}{\mu} \tag{85}$$

where r and r_0 are the interatomic distances in the strained and in the equilibrium configuration, respectively. The quantity μ is a dimensionless parameter measuring the material anharmonicity.

This parameter can be fitted to experiments or to ab initio calculations, and it can be easily cast in the form:

$$\mu = \frac{1}{3} \left(\frac{E_0}{K\omega} \right)^{\frac{1}{2}} \tag{86}$$

where ω is the (average) atomic volume and K is the bulk modulus of the material.⁶² For the zincblend structure, we have $\omega = (2/\sqrt{3})^3 r_0^3$. For silicon carbide, diamond, silicon, and germanium, we calculated $\mu = 0.221, 0.230, 0.205,$ and $0.198,$ respectively. As shown later, these relatively large values are not compatible with the (oversimplified) assumption of first-next-neighbor interactions only; this is consistent with the conclusions of the previous section.

The work $W(s)$ necessary to stretch a perfect crystal hydrostatically up to a scaled interatomic distance s is calculated from Eq. [84] as:

$$W(s) = E_0 + U(s) \tag{87}$$

The work $W(s)$ is completely controlled by the three constants $E_0, \mu,$ and r_0 that, in turn, depend on the actual material. For example, the inflection point r_I of the curve $W(s)$ corresponds to $r_I = r_0(1 + \mu)$, occurring at $s = 1$. Such an interatomic separation is obtained by spending a work $W(r_I) = (1 - 2/e)E_0$ as large as 26% of the total work of separation (per atom) E_0 . In Figure 6 (bottom) the work function $W(s)$ (full line) is represented for the choice $\mu = 0.22,$ corresponding to the SiC case.

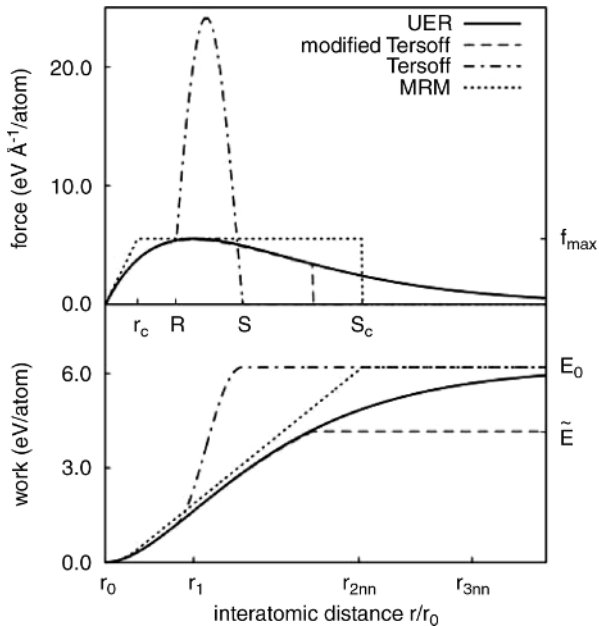


Figure 6 Work (bottom) and force (top) for hydrostatic separation in silicon carbide. r and r_0 are the interatomic distances in the strained and in the equilibrium configuration, respectively. The second and third next-neighbor distance is indicated by r_{2nn} and r_{3nn} , whereas $r_1 = r_0(1 + \mu)$ and μ is given in Eq. [86]. R and S represent the switch-on and switch-off distance for the cut-off function in the Tersoff potential, respectively and $S_c = r_0[1 + (e + 0.5/e)\mu]$. Finally, r_c is fixed by the intersection between the linear and constant force regime. Details are reported elsewhere.³⁹

The force $f(s)$ necessary to separate atoms at the interatomic distance s is obtained straightforwardly from $W(s)$:

$$f(s) = \frac{dW}{ds} = E_0 \frac{s}{\mu r_0} e^{-s} \quad [88]$$

This force is positive for tensile strain ($r > r_0$, i.e., $s > 0$). f is represented in Figure 6 (top panel) by a full line. The maximum separation force $f_{\max} = E_0(e\mu r_0)^{-1}$ is $r_1 = r_0(1 + \mu) = 1.44r_0$, falling within the first $r_{1nn} = r_0$ and the second $r_{2nn} = 1.633r_0$. At distances $r > r_1$ ($s > 1$) the force f decreases as the separation increases. A 90% force reduction (i.e., $f = f_{\max}/10$) is observed when $r \sim 2.0r_0 > r_{3nn} = 1.91r_0$. It is important to clarify that the hydrostatic separation energy described by the UER does not correspond to any realistic fracture event. Nevertheless, we guess that any force model suitable for fracture must be able to reproduce the UER curve correctly.

Determining the Minimum Range for the Model Potential

The development of a force field with a not-too-short range of action is worked out from the corresponding UER by imposing a few fundamental requirements:

1. The force must be a continuous function of strain;
2. The maximum separation force must be reproduced correctly (i.e., $f_{\max}^{sr} = f_{\max}$);
3. The bulk modulus at equilibrium must fit the experimental (or ab initio) value;
4. At tensile strains (up to r_I), the bulk modulus must not increase;
5. The work of separation E_0 must be reproduced correctly.

Condition (2) is related to the fracture toughness of the perfect material. For instance, if the maximum force is overestimated, then the fracture toughness of the material is overestimated as well. Similarly, conditions (3) and (4) are needed to reproduce the elastic properties of the material. Finally, condition (5) imposes a simple physical requirement: the atomic bonds cannot stiffen during tensile deformation up to the maximum force.

Results from the simplest force model fulfilling these conditions are presented in Figure 6 (top panel) as a dotted line. We refer to such a model as the *minimum range model* (MRM). It consists of a linear elastic force across the interval $r_0 \leq r \leq r_c$ (where the bulk modulus is given by the constant value K), whereas for $r_c \leq r \leq S_c$, the force is constant and equal to the f_{\max} value provided by UER. Finally, for any interatomic distance larger than S_c , the force is zero. The actual value of r_c is fixed by the intersection between the linear force with slope K , occurring in the region $[r_0, r_c]$, and the constant f_{\max} . The parameter S_c , in turn, is fixed by the cohesive energy E_0 :³⁹

$$S_c = r_0 + r_0 \left(e + \frac{1}{2e} \right) \mu \quad [89]$$

and sets the minimum range, below which it is not possible to find a force field satisfying conditions 1–5; in other words, a model with force extension below S_c is unlikely to describe brittle fracture.

The value S_c/r_0 depends only on the parameter μ characterizing the material. It can be proved that, in the case of covalent group-IV materials, such a minimum value S_c is close to the second nearest neighbor (2nn) distance at equilibrium. In particular, for silicon carbide, $S_c \approx 1.64r_0$ that is slightly larger than the second nearest neighbor distance $r_{2nn} \approx 1.15r_0$, whereas for silicon and germanium, we get $S_c \sim 0.9r_{2nn}$. These values suggest that only by taking into account interactions beyond the first neighbor ($\sim r_{2nn}$), is it possible to describe correctly the maximum separation force and, in turn, the fracture toughness of a material. This conclusion, although derived by different arguments, is consistent with the discussion in the previous section.

The minimum range model is indeed a very rough model, its only value being explicatory. In particular, this force model hardly can be used in atomistic simulations. A better device is obtained by multiplying the energy function $U(s)$ by a cut-off function $h(s)$, so as to obtain a new force model $T(s)$:

$$T(s) = U(s)h(s) \quad [90]$$

The corresponding work separation $W^{sr}(s)$ is modified accordingly as follows:

$$W^{sr}(s) = E_0 + T(s) \quad [91]$$

and it is (relatively) short-ranged as well. An example of the results of such a model is represented as a dot-dashed line in the bottom panel of Figure 6 where $[R, S]$ is the range in which the cut-off $h(s)$ operates. We remark that the cut-off function does not modify the total work of separation, so that condition (v) is satisfied. Furthermore, it does not modify the force field close to the equilibrium distance. Accordingly, conditions 3–5 are still satisfied by construction. Condition (2), instead, is satisfied only if the range S of the force model is larger than S_c , according to the previous analysis.

These remarks are valid, in general, regardless of the actual form of the potential. In particular, they apply to the original Tersoff potential⁶³ in which $S = 1.33r_0$, a value much shorter than the 2nn distance. This model is represented in Figure 6 as a dot-dashed line. As expected, the force is overestimated in the range $[R, S]$, and a nonphysical peak is observed in the separation force, which is four times larger than the correct maximum value f_{\max} (Figure 6, top panel).

Although the present analysis suggests to extend the interactions range beyond the second nearest neighbors distance, this solution is unfortunately demanding in terms of the development of the new model potential. In particular, this approach would imply refitting existing force fields, possibly generating inconsistency with previous results. This is an unpleasant feature because a huge body of valuable knowledge has been produced so far by using the original short-range potentials. Alternatively, it is possible to cure the major deficiencies of the original model potentials by using modified cut-off functions (such as environmentally dependent cut-off functions,⁵⁶ as well as nonconservative force fields).³⁹

Atomic-Scale Stress

Identifying the stress tensor by means of atomistic quantities is important because it allows for the comparison of the results obtained through molecular dynamics simulations with those achieved within the continuum elasticity theory.

To obtain the atomic-scale counterpart of the Cauchy stress tensor (see Eqs. [14] and [15]), we consider a small portion of a given elastic body with volume V and surface S . We suppose that, in this region, there are N atoms described by positions \vec{x}_α for $\alpha = 1, \dots, N$. The number of the atoms is large enough to allow the definition of the macroscopic elastic fields (stress and strain) in that region, but it is also small enough to identify the local stress with its average on the volume. To get the continuum-to-molecular equivalence, it is useful to introduce the so-called virial form $\sum_{\alpha=1}^N \vec{x}_\alpha \otimes \vec{F}_\alpha$ where the symbol \otimes represents the tensor product of vectors (see the Appendix). The quantity \vec{F}_α is the total force acting on the α -th atom, and therefore, the equation of motion $\vec{F}_\alpha = m_\alpha \vec{a}_\alpha$ (m_α is the mass of the α -th atom) leads to the balance:

$$\sum_{\alpha=1}^N \vec{x}_\alpha \otimes \vec{F}_\alpha = \sum_{\alpha=1}^N m_\alpha \vec{x}_\alpha \otimes \vec{a}_\alpha \quad [92]$$

Now, the total force \vec{F}_α can be written as the sum of two contributions: $\vec{F}_\alpha^{\text{int}}$, which is the internal force on the α th atom caused by the atoms contained in the volume V ; and $\vec{F}_\alpha^{\text{ext}}$, which is the external force on the α th atom caused by the atoms falling outside the V and by any external action. By exploiting this contributions we get:

$$\sum_{\alpha=1}^N \vec{x}_\alpha \otimes \vec{F}_\alpha^{\text{int}} + \sum_{\alpha=1}^N \vec{x}_\alpha \otimes \vec{F}_\alpha^{\text{ext}} = \sum_{\alpha=1}^N m_\alpha \vec{x}_\alpha \otimes \vec{a}_\alpha \quad [93]$$

The external force $\vec{F}_\alpha^{\text{ext}}$, in turn, is given by the surface force $\vec{F}_\alpha^{\text{ext}}(S)$ (caused by atoms nearby the surface S) and by the body force $\vec{F}_\alpha^{\text{ext}}(V)$ (caused by external fields). Therefore, Eq. [93] can be cast in the form:

$$\sum_{\alpha=1}^N \vec{x}_\alpha \otimes \vec{F}_\alpha^{\text{int}} + \sum_{\alpha=1}^N \vec{x}_\alpha \otimes \vec{F}_\alpha^{\text{ext}}(V) + \sum_{\alpha=1}^N \vec{x}_\alpha \otimes \vec{F}_\alpha^{\text{ext}}(S) = \sum_{\alpha=1}^N m_\alpha \vec{x}_\alpha \otimes \frac{d\vec{v}_\alpha}{dt} \quad [94]$$

where \vec{v}_α is the velocity of the α th atom. We observe that the velocity \vec{v}_α of each atom is the sum $\vec{v}_\alpha = \vec{v}_\alpha^d + \vec{v}_\alpha^{\text{th}}$ of a macroscopic drift \vec{v}_α^d and a thermal fluctuation $\vec{v}_\alpha^{\text{th}}$. The macroscopic drift velocities \vec{v}_α^d of the α th atom is defined as the mean value of the velocities \vec{v}_β of the atoms belonging to a given neighborhood of the α th site. Evidently, this mean value removes the statistical fluctuations, resulting in a macroscopic quantity. Therefore, we get the following:

$$\sum_{\alpha=1}^N \vec{x}_\alpha \otimes \vec{F}_\alpha^{\text{int}} + \sum_{\alpha=1}^N \vec{x}_\alpha \otimes \vec{F}_\alpha^{\text{ext}}(V) + \sum_{\alpha=1}^N \vec{x}_\alpha \otimes \vec{F}_\alpha^{\text{ext}}(S) \quad [95]$$

$$= \sum_{\alpha=1}^N m_{\alpha} \ddot{x}_{\alpha} \otimes \frac{d\vec{v}_{\alpha}^d}{dt} + \sum_{\alpha=1}^N m_{\alpha} \ddot{x}_{\alpha} \otimes \frac{d\vec{v}_{\alpha}^{th}}{dt}$$

Any quantity appearing in Eq. [95] must be understood as instantaneous. To obtain the corresponding average values, we introduce the time average $\langle \cdot \rangle = \lim_{\tau \rightarrow \infty} \frac{1}{\tau} \int_0^{\tau} (\cdot) dt$. As for the last term of the right-hand side of Eq. [95] we get:

$$\begin{aligned} \left\langle \sum_{\alpha=1}^N m_{\alpha} \ddot{x}_{\alpha} \otimes \frac{d\vec{v}_{\alpha}^{th}}{dt} \right\rangle &= \left\langle \sum_{\alpha=1}^N m_{\alpha} \left[\frac{d}{dt} (\ddot{x}_{\alpha} \otimes \vec{v}_{\alpha}^{th}) - \ddot{v}_{\alpha} \otimes \vec{v}_{\alpha}^{th} \right] \right\rangle \quad [96] \\ &= \lim_{\tau \rightarrow \infty} \frac{1}{\tau} \int_0^{\tau} \sum_{\alpha=1}^N m_{\alpha} \frac{d}{dt} (\ddot{x}_{\alpha} \otimes \vec{v}_{\alpha}^{th}) dt \\ &\quad - \left\langle \sum_{\alpha=1}^N m_{\alpha} \ddot{v}_{\alpha} \otimes \vec{v}_{\alpha}^{th} \right\rangle \\ &= \lim_{\tau \rightarrow \infty} \frac{1}{\tau} \sum_{\alpha=1}^N m_{\alpha} \ddot{x}_{\alpha} \otimes \vec{v}_{\alpha}^{th} \Big|_{t=0}^{t=\tau} - \left\langle \sum_{\alpha=1}^N m_{\alpha} \ddot{v}_{\alpha} \otimes \vec{v}_{\alpha}^{th} \right\rangle \end{aligned}$$

We are dealing with an elastic solid body, which is a stable bound system (i.e., a system that hangs together forever). In other words, coordinates and velocities for all particles are expressed by finite quantities forever. In this case, the function $G(t) = \sum_{\alpha=1}^N m_{\alpha} \ddot{x}_{\alpha} \otimes \vec{v}_{\alpha}^{th}$ is bounded between two extremes, G_{\min} and G_{\max} , and the first term in Eq. [96] is, therefore, zero in the limit of very long times τ

$$\begin{aligned} \lim_{\tau \rightarrow \infty} \frac{1}{\tau} \sum_{\alpha=1}^N m_{\alpha} \ddot{x}_{\alpha} \otimes \vec{v}_{\alpha}^{th} \Big|_{t=0}^{t=\tau} &= \lim_{\tau \rightarrow \infty} \frac{G(\tau) - G(0)}{\tau} \quad [97] \\ &\leq \lim_{\tau \rightarrow \infty} \frac{G_{\max} - G_{\min}}{\tau} = 0 \end{aligned}$$

On the other hand, the last term in Eq. [96] can be computed easily as follows:

$$\left\langle \sum_{\alpha=1}^N m_{\alpha} \ddot{v}_{\alpha} \otimes \vec{v}_{\alpha}^{th} \right\rangle = \left\langle \sum_{\alpha=1}^N m_{\alpha} \ddot{v}_{\alpha}^d \otimes \vec{v}_{\alpha}^{th} \right\rangle + \left\langle \sum_{\alpha=1}^N m_{\alpha} \ddot{v}_{\alpha}^{th} \otimes \vec{v}_{\alpha}^{th} \right\rangle \quad [98]$$

The first term is zero because $\langle \ddot{v}_{\alpha}^{th} \rangle = 0$ (we also have used the statistical independence of \ddot{v}_{α}^d and \ddot{v}_{α}^{th}). Conversely, the second term is quadratic in the

fluctuation \vec{v}_α^{th} , and it is not negligible. So far, we have proved the following important result:

$$\left\langle \sum_{\alpha=1}^N m_\alpha \vec{x}_\alpha \otimes \frac{d\vec{v}_\alpha^{th}}{dt} \right\rangle = - \left\langle \sum_{\alpha=1}^N m_\alpha \vec{v}_\alpha^{th} \otimes \vec{v}_\alpha^{th} \right\rangle \quad [99]$$

and, therefore, the virial balance given in Eq. [95] can be written as:

$$\begin{aligned} \left\langle \sum_{\alpha=1}^N \vec{x}_\alpha \otimes \vec{F}_\alpha^{\text{int}} \right\rangle + \left\langle \sum_{\alpha=1}^N \vec{x}_\alpha \otimes \vec{F}_\alpha^{\text{ext}}(V) \right\rangle + \left\langle \sum_{\alpha=1}^N \vec{x}_\alpha \otimes \vec{F}_\alpha^{\text{ext}}(S) \right\rangle & [100] \\ = \left\langle \sum_{\alpha=1}^N m_\alpha \vec{x}_\alpha \otimes \frac{d\vec{v}_\alpha^d}{dt} \right\rangle - \left\langle \sum_{\alpha=1}^N m_\alpha \vec{v}_\alpha^{th} \otimes \vec{v}_\alpha^{th} \right\rangle \end{aligned}$$

To proceed further, we must link some atomic terms with their continuum counterparts. In fact, we have that the term depending on body forces corresponds to a volume integral; the term depending on surface forces corresponds to a surface integral; the first term in the right-hand side can be converted to a volume integral by observing that $d\vec{v}_\alpha^d/dt$ is the macroscopic acceleration field \vec{a} . Accordingly:

$$\begin{aligned} \left\langle \sum_{\alpha=1}^N \vec{x}_\alpha \otimes \vec{F}_\alpha^{\text{int}} \right\rangle + \left\langle \int_V \vec{x} \otimes \vec{F}^{\text{ext}}(V) d\vec{x} \right\rangle + \left\langle \int_S \vec{x} \otimes \vec{F}^{\text{ext}}(S) dS \right\rangle & [101] \\ = \left\langle \int_V \rho \vec{x} \otimes \vec{a} d\vec{x} \right\rangle - \left\langle \sum_{i=1}^N m_\alpha \vec{v}_\alpha^{th} \otimes \vec{v}_\alpha^{th} \right\rangle \end{aligned}$$

As described in “The Concept of Stress” on page 10, in continuum elasticity we have $\vec{F}^{\text{ext}}(V) = \vec{b}$ and $\vec{F}^{\text{ext}}(S) = \hat{T}\vec{n}$. Therefore, the balance equation given in Eq. [100] becomes:

$$\begin{aligned} \left\langle \sum_{\alpha=1}^N \vec{x}_\alpha \otimes \vec{F}_\alpha^{\text{int}} \right\rangle + \left\langle \int_V \vec{x} \otimes \vec{b} d\vec{x} \right\rangle + \left\langle \int_S \vec{x} \otimes (\hat{T}\vec{n}) dS \right\rangle & [102] \\ = \left\langle \int_V \rho \vec{x} \otimes \vec{a} d\vec{x} \right\rangle - \left\langle \sum_{\alpha=1}^N m_\alpha \vec{v}_\alpha^{th} \otimes \vec{v}_\alpha^{th} \right\rangle \end{aligned}$$

or, equivalently:

$$\begin{aligned} \left\langle \sum_{\alpha=1}^N x_{\alpha,k} F_{\alpha,b}^{\text{int}} \right\rangle + \left\langle \int_V x_k b_b d\vec{x} \right\rangle + \left\langle \int_S x_k T_{bp} n_p dS \right\rangle \\ = \left\langle \int_V \rho x_k a_b d\vec{x} \right\rangle - \left\langle \sum_{\alpha=1}^N m_{\alpha} v_{\alpha,k}^{th} v_{\alpha,b}^{th} \right\rangle \end{aligned} \quad [103]$$

By applying the divergence theorem to the surface integral, we get the following:

$$\begin{aligned} \left\langle \sum_{\alpha=1}^N x_{\alpha,k} F_{\alpha,b}^{\text{int}} \right\rangle + \left\langle \int_V x_k b_b d\vec{x} \right\rangle + \left\langle \int_V \frac{\partial}{\partial x_p} (x_k T_{bp}) d\vec{x} \right\rangle \\ = \left\langle \int_V \rho x_k a_b d\vec{x} \right\rangle - \left\langle \sum_{\alpha=1}^N m_{\alpha} v_{\alpha,k}^{th} v_{\alpha,b}^{th} \right\rangle \end{aligned} \quad [104]$$

We now can develop the derivative:

$$\begin{aligned} \left\langle \sum_{\alpha=1}^N x_{\alpha,k} F_{\alpha,b}^{\text{int}} \right\rangle + \left\langle \int_V x_k b_b d\vec{x} \right\rangle + \left\langle \int_V \left(\delta_{kp} T_{bp} + x_k \frac{\partial T_{bp}}{\partial x_p} \right) d\vec{x} \right\rangle \\ = \left\langle \int_V \rho x_k a_b d\vec{x} \right\rangle - \left\langle \sum_{\alpha=1}^N m_{\alpha} v_{\alpha,k}^{th} v_{\alpha,b}^{th} \right\rangle \end{aligned} \quad [105]$$

so that:

$$\begin{aligned} \left\langle \sum_{\alpha=1}^N x_{\alpha,k} F_{\alpha,b}^{\text{int}} \right\rangle + \left\langle \int_V T_{bk} d\vec{x} \right\rangle \\ + \left\langle \int_V x_k \left(\frac{\partial T_{bp}}{\partial x_p} + b_b - \rho a_b \right) d\vec{x} \right\rangle + \left\langle \sum_{\alpha=1}^N m_{\alpha} v_{\alpha,k}^{th} v_{\alpha,b}^{th} \right\rangle = 0 \end{aligned} \quad [106]$$

The third term is zero because of Eq. [18]. Moreover, we can define the local average value:

$$\mathcal{T}_{bk} = \frac{1}{V} \int_V T_{bk} d\vec{x} \quad [107]$$

of the stress tensor over the V . In conclusion, the balance equation for the virial sum leads to the following definition of stress:

$$\langle \mathcal{T}_{hk} \rangle = -\frac{1}{V} \left\langle \sum_{\alpha=1}^N m_{\alpha} v_{\alpha,k}^{th} v_{\alpha,h}^{th} \right\rangle - \frac{1}{V} \left\langle \sum_{\alpha=1}^N x_{\alpha,k} F_{\alpha,h}^{\text{int}} \right\rangle \quad [108]$$

where only atomic-scale quantities are used, namely: particle positions and velocities and interatomic forces. This very important relation links atomistic to continuum elasticity; it can be written in tensor form as follows:

$$\langle \hat{\mathcal{T}} \rangle = -\frac{1}{V} \left\langle \sum_{\alpha=1}^N m_{\alpha} \vec{v}_{\alpha}^{th} \otimes \vec{v}_{\alpha}^{th} \right\rangle - \frac{1}{V} \left\langle \sum_{\alpha=1}^N \vec{x}_{\alpha} \otimes \vec{F}_{\alpha}^{\text{int}} \right\rangle \quad [109]$$

This result has innumerable applications in molecular dynamics simulations of mechanical properties. In fact, it enables us to evaluate the macroscopic Cauchy stress in an elastic solid system defined at the atomic or molecular level. We remark that we have identified a macroscopic field (the stress tensor introduced in “The Concept of Stress” section) with a combination of microscopic quantities by means of two average procedures: the first one performed over the V (denoted by $\hat{\mathcal{T}}$) and the second one over the time (denoted by the angle brackets). It is also important to observe that the first kinetic term depends on the velocity contribution resulting from thermal fluctuations only, although it does not depend on drift velocities. This contribution plays a key role in finite-temperature thermoelasticity.⁶⁴ We point out that Eq. [109] is exactly correct for systems undergoing arbitrary time-dependent deformations.

It is possible to reformulate the result given in Eq. [109] by writing:

$$\langle \hat{\mathcal{T}} \rangle = -\frac{1}{N\omega} \left\langle \sum_{\alpha=1}^N m_{\alpha} \vec{v}_{\alpha}^{th} \otimes \vec{v}_{\alpha}^{th} \right\rangle - \frac{1}{N\omega} \left\langle \sum_{\alpha=1}^N \vec{x}_{\alpha} \otimes \vec{F}_{\alpha}^{\text{int}} \right\rangle \quad [110]$$

where we have attributed to any atom the same average volume $\omega = V/N$. Although this assumption is widely used in atomistic simulations on mechanical behavior of materials, it nevertheless should be noted that it is, in principle, correct for atomic-scale homogeneous systems only. Actually, many interesting problems in modern nanomechanics (including fracture) refer to systems that do not fulfill such an assumption. We, therefore, need to better refine the volume concept by introducing a suitable criterion for dividing the space into locally proper subdomains that we will refer to as atomic volumes ω_{α} :

$$\langle \hat{\mathcal{T}} \rangle = -\frac{1}{N} \left\langle \sum_{\alpha=1}^N \frac{m_{\alpha}}{\omega_{\alpha}} \vec{v}_{\alpha}^{th} \otimes \vec{v}_{\alpha}^{th} \right\rangle - \frac{1}{N} \left\langle \sum_{\alpha=1}^N \frac{1}{\omega_{\alpha}} \vec{x}_{\alpha} \otimes \vec{F}_{\alpha}^{\text{int}} \right\rangle \quad [111]$$

A possible solution is offered by the following discretization procedure. We can work out a partitioning of the total available space into elementary volumes (much smaller than ω_α). Then, each elementary volume is uniquely assigned to its next-neighbor atom site.⁶⁵ The atomic volume of any given lattice site is finally defined as the sum of the elementary volumes attributed to that atom site. It can be proved that such a discretization procedure is basically equivalent to the Voronoi tessellation; it is unique, and unambiguously attributes to each atom a proper value of the volume.

Finally, it is possible to find a direct conceptual relation between the atomic stress defined in Eq. [109] and the Cauchy stress tensor derived by the strain energy function, as in Eq. [45]. To reconcile these two points of view, we observe that, at thermodynamic equilibrium, the first tensor term in Eq. [109] is directly proportional to the temperature because it contains the average values of the kinetic quantities $m_\alpha \bar{v}_\alpha^{th} \otimes \bar{v}_\alpha^{th}$. Therefore, in the thermal linear approximation, we can write the following:

$$-\frac{1}{V} \left\langle \sum_{\alpha=1}^N m_\alpha \bar{v}_\alpha^{th} \otimes \bar{v}_\alpha^{th} \right\rangle = -\hat{C} \hat{\alpha} T \quad [112]$$

where \hat{C} is the (fourth-order) stiffness tensor, $\hat{\alpha}$ is the (second-order) thermal expansion coefficient tensor (satisfying the symmetry relation $\alpha_{ij} = \alpha_{ji}$), and T is the temperature. The second term in Eq. [109] can be handled by observing that $\bar{F}_\alpha^{\text{int}} = -V \frac{\partial U}{\partial \bar{x}_\alpha}$, where U is the strain energy function defined in Eq. [45]. So, Eq. [109] assumes the form:

$$\langle \hat{T} \rangle = -\hat{C} \hat{\alpha} T + \left\langle \sum_{\alpha=1}^N \bar{x}_\alpha \otimes \frac{\partial U}{\partial \bar{x}_\alpha} \right\rangle \quad [113]$$

Now, we observe that $\frac{\partial U}{\partial \hat{\epsilon}} = \sum_{\alpha=1}^N \bar{x}_\alpha \otimes \frac{\partial U}{\partial \bar{x}_\alpha}$ and, therefore:

$$\langle \hat{T} \rangle = -\hat{C} \hat{\alpha} T + \left\langle \frac{\partial U}{\partial \hat{\epsilon}} \right\rangle \quad [114]$$

When we are working at $T = 0$, Eq. [114] is perfectly consistent with Eq. [45] as expected. Moreover, for a linear elastic material, we have $\langle \frac{\partial U}{\partial \hat{\epsilon}} \rangle = \hat{C} \hat{\epsilon}$, and therefore, Eq. [114] is simplified as follows:

$$\langle \hat{T} \rangle = -\hat{C} \hat{\alpha} T + \hat{C} \hat{\epsilon} = \hat{C} (\hat{\epsilon} - \hat{\alpha} T) \quad [115]$$

When the stress tensor is zero, we must have $\hat{\epsilon} = \hat{\alpha}T$, obtaining the physical meaning of the thermal expansion coefficient tensor $\hat{\alpha}$; it represents the thermal-induced strain for any degree of temperature.

A Different Form of the Virial Stress

We add some comments so the reader can avoid possible misunderstandings, which often are encountered in the literature when discussing the stress concept. As a matter of fact, the *virial stress* $\langle \hat{\Pi} \rangle$ is one of the most commonly used stress-like quantities in discrete particle systems (it is also called the *pressure tensor*), and it is sometimes defined as follow:^{66,67}

$$\langle \hat{\Pi} \rangle = -\frac{1}{V} \left\langle \sum_{\alpha=1}^N m_{\alpha} \frac{d\vec{x}_{\alpha}}{dt} \otimes \frac{d\vec{x}_{\alpha}}{dt} \right\rangle - \frac{1}{V} \left\langle \sum_{\alpha=1}^N \vec{x}_{\alpha} \otimes \vec{F}_{\alpha}^{\text{int}} \right\rangle \quad [116]$$

Such a virial stress concept is typically obtained by generalizing the Clausius and Maxwell theories for pressure.^{68,69} The first term depends on the mass and on the absolute velocity of atomic particles, reflecting that mass transfer generates a pressure on stationary spatial surfaces external to an atomic-particle system. The second term depends on interatomic forces and atomic positions, providing a continuum measure for the internal mechanical interactions between particles. However, the *virial stress* defined in Eq. [116] is not a measure of the Cauchy mechanical stress within an elastic body undergoing an arbitrary deformation.⁷⁰ As shown in the previous section, it can be proved that the absolute velocities $\vec{v}_{\alpha} = d\vec{x}_{\alpha}/dt$ in Eq. [116] must be replaced with thermal velocities \vec{v}_{α}^{th} to properly obtain the Cauchy stress.⁷¹

We also remark that the virial approach or virial theorem (Clausius 1870), as applied to gas systems for the evaluation of external pressure, captures this effect correctly. The key concept is that the pressure represents external forces between an atomic system and a container (where the pressure is generated by the collisions of the atoms on the inner surface of the container). In contrast, stress represents internal forces between particles inside a body (and it is not generated by collisions against a wall). Indeed, Eq. [116] describes the macroscopic pressure of a gas system correctly under the three following conditions: (1) the system is in statistical equilibrium, (2) the pressure is to be interpreted in a time- and volume-averaged sense (i.e., fluctuations at the molecular level are assumed to average out over time and space) and (3) the pressure must be recognized as the average force per unit area on the wall of a physical container holding the gas system. The *virial stress* given in Eq. [116] must be applied in molecular dynamics simulations when one is analyzing the pressure (or pressure tensor) of a gas or a fluid at thermodynamic equilibrium onto the inner surface of its container.

We recall that, in continuum mechanics, the Lagrangian reference frame is a way of looking at the motion in which the observer follows individual body particles as they move through space and time. Therefore, in this picture, the key quantity is the trajectory of a given volume element identified by its initial conditions. On the other hand, the Eulerian reference frame is a way of looking at the motion that focuses on specific locations in the space through which the body particles pass. In this case, the physical observables are described by scalar or vector fields, defined in a given point of the space. Eq. [109] represents the atomic counterpart of the Cauchy stress when it is considered in an Eulerian (spatial) reference frame. Andia, Costanzo, and Gray^{72,73} have taken a Lagrangian (material) frame of reference to show that the stress in the atomic system does not contain a velocity term at all by obtaining the further relation:

$$\langle \hat{\mathcal{T}}_{\mathcal{E}} \rangle = -\frac{1}{V} \left\langle \sum_{\alpha=1}^N \vec{x}_{\alpha} \otimes \bar{\vec{F}}_{\alpha}^{\text{int}} \right\rangle \quad [117]$$

Gao and Weiner⁷⁴ clearly show that the dynamic term is included only in an Eulerian (spatial) reference frame and not in a Lagrangian frame of reference. They also show the equivalence between the Eulerian (spatial) and the Lagrangian (material) definitions of virial stress.⁷⁴ Either way, in molecular dynamics simulations, the Eulerian point of view always must be considered to draw meaningful comparisons between numerical and continuum results.⁶⁴

Atomic Stress for Arbitrary Two-Body Interactions

In this section, we specialize the general result given in Eq. [109] to the case of two-body interactions between the atoms within a solid elastic body. The quantity $\bar{\vec{F}}_{\alpha}^{\text{int}}$ can be written as the sum $\sum_{\beta \neq \alpha}^N \vec{f}_{\alpha\beta}$, where $\vec{f}_{\alpha\beta}$ is the force applied on atom α by atom β . Eq. [109] can be converted to:

$$\langle \hat{\mathcal{T}} \rangle = -\frac{1}{V} \left\langle \sum_{\alpha=1}^N m_{\alpha} \vec{v}_{\alpha}^{\text{th}} \otimes \vec{v}_{\alpha}^{\text{th}} \right\rangle - \frac{1}{V} \left\langle \sum_{\alpha=1}^N \vec{x}_{\alpha} \otimes \sum_{\beta \neq \alpha}^N \vec{f}_{\alpha\beta} \right\rangle \quad [118]$$

The last term can be split into two identical terms as follows:

$$\begin{aligned} \langle \hat{\mathcal{T}} \rangle &= -\frac{1}{V} \left\langle \sum_{\alpha=1}^N m_{\alpha} \vec{v}_{\alpha}^{\text{th}} \otimes \vec{v}_{\alpha}^{\text{th}} \right\rangle \\ &\quad - \frac{1}{2V} \left\langle \sum_{\alpha=1}^N \vec{x}_{\alpha} \otimes \sum_{\beta \neq \alpha}^N \vec{f}_{\alpha\beta} \right\rangle + \frac{1}{2V} \left\langle \sum_{\alpha=1}^N \vec{x}_{\alpha} \otimes \sum_{\beta \neq \alpha}^N \vec{f}_{\beta\alpha} \right\rangle \end{aligned} \quad [119]$$

because $\vec{f}_{\beta\alpha} = -\vec{f}_{\alpha\beta}$. After some algebra we get the following:

$$\langle \hat{T} \rangle = -\frac{1}{V} \left\langle \sum_{\alpha=1}^N m_{\alpha} \vec{v}_{\alpha}^{th} \otimes \vec{v}_{\alpha}^{th} \right\rangle + \frac{1}{2V} \left\langle \sum_{\alpha=1}^N \sum_{\beta \neq \alpha}^N \vec{x}_{\alpha\beta} \otimes \vec{f}_{\alpha\beta} \right\rangle \quad [120]$$

where $\vec{x}_{\alpha\beta} = \vec{x}_{\beta} - \vec{x}_{\alpha}$. This form is particularly useful for molecular dynamics simulations because the force term $\vec{f}_{\alpha\beta}$ is linked directly with the interaction potential energy $U^{2B}(r)$

$$\vec{f}_{\alpha\beta} = \left. \frac{dU^{2B}(r)}{dr} \right|_{r=|\vec{x}_{\alpha\beta}|} \frac{\vec{x}_{\alpha\beta}}{|\vec{x}_{\alpha\beta}|} \quad [121]$$

By substituting Eq. [121] into Eq. [120], we obtain:

$$\begin{aligned} \langle \hat{T} \rangle &= -\frac{1}{V} \left\langle \sum_{\alpha=1}^N m_{\alpha} \vec{v}_{\alpha}^{th} \otimes \vec{v}_{\alpha}^{th} \right\rangle \\ &+ \frac{1}{2V} \left\langle \sum_{\alpha=1}^N \sum_{\beta \neq \alpha}^N \vec{x}_{\alpha\beta} \otimes \vec{x}_{\alpha\beta} \left(\frac{1}{r} \frac{dU^{2B}(r)}{dr} \right) \right|_{r=|\vec{x}_{\alpha\beta}|} \right\rangle \end{aligned} \quad [122]$$

This form is useful because it depends only on quantities available during any simulations, and it is well suited for being used under the typical assumption of periodic boundary conditions.

Atomic Stress for Arbitrary Many-Body Interactions

In this section, we derive a formulation of Eq. [109] that can be used for any many-body force field. We observe that many-body interactions such as Stillinger–Weber, Tersoff, Brenner, and EDIP, as well as tight-binding ones, have a total potential energy U that can be written in terms of all the possible (scalar) distances between each couple of atoms. If we define $x_{\alpha\beta} = |\vec{x}_{\alpha\beta}| = |\vec{x}_{\beta} - \vec{x}_{\alpha}|$, then we get $U = U(\{x_{\alpha\beta}\})$.

For a system of N atoms, we have $N(N-1)/2$ independent distances $x_{\alpha\beta}$ that define the positions of the particles up to a nonessential roto-translation (the total energy U must be invariant under roto-translation of the particle system). From Eq. [108] we obtain:

$$\langle \mathcal{T}_{bk} \rangle = -\frac{1}{V} \left\langle \sum_{\alpha=1}^N m_{\alpha} v_{\alpha,k}^{th} v_{\alpha,b}^{th} \right\rangle - \frac{1}{V} \langle \Gamma_{bk} \rangle \quad [123]$$

where

$$\begin{aligned}
 \Gamma_{hk} &= \sum_{\alpha=1}^N x_{\alpha,k} F_{\alpha,h}^{\text{int}} = - \sum_{\alpha=1}^N x_{\alpha,k} \frac{\partial U}{\partial x_{\alpha,h}} \\
 &= - \sum_{\alpha=1}^N x_{\alpha,k} \frac{1}{2} \sum_{\delta=1}^N \sum_{\rho=1}^N \frac{\partial U}{\partial x_{\delta\rho}} \frac{\partial x_{\delta\rho}}{\partial x_{\alpha,h}}
 \end{aligned} \tag{124}$$

where $\partial U / \partial x_{\gamma\gamma}$ is zero by definition (U does not depend on $x_{\gamma\gamma}$ because $x_{\gamma\gamma} = 0$ for any atom γ). We simply obtain the following:

$$\frac{\partial x_{\delta\rho}}{\partial x_{\alpha,h}} = \frac{\partial |\vec{x}_\rho - \vec{x}_\delta|}{\partial x_{\alpha,h}} = \frac{(\delta_{\delta\alpha} - \delta_{\rho\alpha}) (x_{\delta,h} - x_{\rho,h})}{x_{\delta\rho}} \tag{125}$$

We also define $x_{\alpha\beta,s} = \vec{x}_{\alpha\beta} \times \vec{e}_s$ and therefore:

$$\begin{aligned}
 \Gamma_{hk} &= \sum_{\alpha=1}^N x_{\alpha,k} \frac{1}{2} \sum_{\delta=1}^N \sum_{\rho=1}^N \frac{\partial U}{\partial x_{\delta\rho}} \frac{(\delta_{\delta\alpha} - \delta_{\rho\alpha}) x_{\delta\rho,h}}{x_{\delta\rho}} \\
 &= \sum_{\alpha=1}^N \sum_{\rho=1}^N \frac{x_{\alpha,k}}{2} \frac{\partial U}{\partial x_{\alpha\rho}} \frac{x_{\alpha\rho,h}}{x_{\alpha\rho}} - \sum_{\beta=1}^N \sum_{\delta=1}^N \frac{x_{\beta,k}}{2} \frac{\partial U}{\partial x_{\delta\beta}} \frac{x_{\delta\beta,h}}{x_{\delta\beta}} \\
 &= \sum_{\alpha=1}^N \sum_{\rho=1}^N \frac{x_{\alpha,k}}{2} \frac{\partial U}{\partial x_{\alpha\rho}} \frac{x_{\alpha\rho,h}}{x_{\alpha\rho}} - \sum_{\rho=1}^N \sum_{\alpha=1}^N \frac{x_{\rho,k}}{2} \frac{\partial U}{\partial x_{\alpha\rho}} \frac{x_{\alpha\rho,h}}{x_{\alpha\rho}} \\
 &= - \sum_{\alpha=1}^N \sum_{\rho=1}^N \frac{x_{\alpha\rho,h} x_{\alpha\rho,k}}{2} \frac{1}{x_{\alpha\rho}} \frac{\partial U}{\partial x_{\alpha\rho}}
 \end{aligned} \tag{126}$$

By substituting Eq. [126] in Eq. [123], we get the following:

$$\langle \mathcal{T}_{hk} \rangle = - \frac{1}{V} \left\langle \sum_{\alpha=1}^N m_\alpha v_{\alpha,k}^{th} v_{\alpha,h}^{th} \right\rangle + \frac{1}{V} \left\langle \sum_{\alpha=1}^N \sum_{\beta=1}^N \frac{x_{\alpha\beta,h} x_{\alpha\beta,k}}{2} \frac{1}{x_{\alpha\beta}} \frac{\partial U}{\partial x_{\alpha\beta}} \right\rangle \tag{127}$$

or, equivalently, in tensor form:

$$\langle \hat{\mathcal{T}} \rangle = - \frac{1}{V} \left\langle \sum_{\alpha=1}^N m_\alpha \vec{v}_\alpha^{th} \otimes \vec{v}_\alpha^{th} \right\rangle + \frac{1}{2V} \left\langle \sum_{\alpha=1}^N \sum_{\beta \neq \alpha}^N \vec{x}_{\alpha\beta} \otimes \vec{x}_{\alpha\beta} \frac{1}{x_{\alpha\beta}} \frac{\partial U}{\partial x_{\alpha\beta}} \right\rangle \tag{128}$$

Note that when the total energy U represents a system of two-body interactions, Eq. [128] reduces to Eq. [122], as expected. Once again, Eq. [128] is useful because it depends only on physical quantities available during any standard simulation.

LINEAR ELASTIC FRACTURE MECHANICS

Conceptual Layout

We now discuss the fundamental principles of fracture mechanics within the elasticity theory framework presented in “Essential Continuum Elasticity Theory”. The resulting theory has been named linear elastic fracture mechanics (LEFM). This implies that we will study fracture in linear elastic (brittle) solids. We remark that, although LEFM is an important task for many applications, it nevertheless has severe limitations because many real materials are ductile (i.e., they are not perfectly elastic and they undergo significant plastic deformation under large applied strains). The investigation of the fracture in a plastic or ductile material is called elastic-plastic fracture mechanics; it falls beyond the scope of the present review.

To better define the limits of validity for the theory to be developed here, we report in Figure 7 the paradigmatic stress–strain curves for brittle and plastic materials, showing how some mechanical properties of a material can be determined. Experiments measure the displacement caused by an applied load, and these two quantities then are converted into strain and stress, respectively, via simple relations. Brittle materials (like ceramics) fail at a given value of

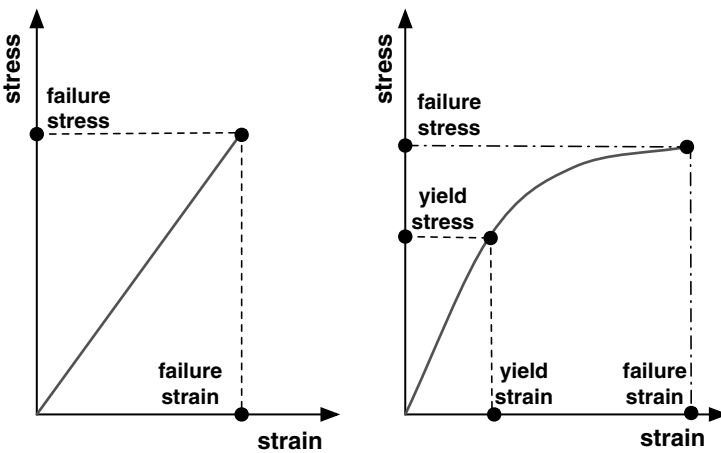


Figure 7 Schematic stress–strain curves for a brittle material (left) and a plastic material (right).

stress called the failure (ultimate) strength. Before failure, they follow a perfect linear constitutive relation defined by the elastic moduli. Plastic materials (such as metals) are described by a linear stress–strain relation for small deformations and start to deform (in the plastic regime, i.e., permanently) at the yield point before eventually failing at higher values of stress (failure strength).

These behaviors are valid for perfect homogeneous bodies, and therefore, the theoretical failure strength σ_f is a quantity that depends only on intrinsic material properties and not on possible defects of its microstructure. To introduce the main principles of fracture mechanics, we must admit (it has been verified experimentally) that any real material is not a perfectly homogeneous elastic body. Therefore, we suppose that it is a complex microstructured object; for example, it can contain possible inhomogeneities (small regions with different elastic properties) or cracks (void cuts). The existence of such a microstructure modifies the elastic or mechanical response of the overall body. We will prove that the flaws lower the failure strength by magnifying the local stress.

Stress Concentration

The first quantitative evidence for the stress concentration effect of flaws was provided by Inglis in 1913⁷⁵ by considering elliptical holes in flat plates (a plate is a specimen in which the thickness is much smaller than the other two dimensions), as in Figure 8. From the methodological point of view, this problem can be solved by using the complex variable method.^{75,76} The detailed solution also can be found in Refs. 77, 78. In particular, let us suppose that a plate containing a crack of length $2L$ (major axis) and thickness $2B$ (minor axis) is subjected to a remote uniaxial load σ along the y direction, as shown in Figure 8. Then, it is found that the actual stress occurring at the crack tips is as follows:

$$T_{yy}^{\text{tip}} = \sigma \left(1 + \frac{2L}{B} \right) = \sigma \left(1 + 2\sqrt{\frac{L}{\rho}} \right) \quad [129]$$

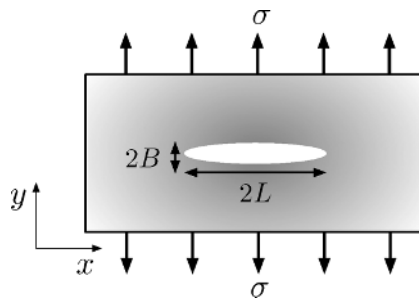


Figure 8 Elliptic hole in a flat (i.e., two-dimensional) plate under applied stress perpendicular to its major axis.

where $\rho = B^2/L$ is the radius of curvature at the crack tips. The stress enhancement, therefore, depends on the aspect ratio of the elliptic hole. We note that T_{yy} is the stress component that opens the crack (therefore, it is mainly responsible for failure). Moreover, the stress at the hole boundary where it is intersected by the minor axis is $T_{xx} = -\sigma$, independent of the aspect ratio. When $L = B$, the stress T_{yy}^{tip} reduces to the solution for a circular hole, for which the stress concentration factor is as large as 3. Interestingly, Eq. [129] predicts an infinite enhancement of the stress at the tips of the crack with vanishingly small thickness (slit crack). We remark that this nonphysical result is only because of the here adopted continuum hypothesis, whereas it is not relevant for the atomic architectures forming real materials. It is easy to figure out that, in atomic lattices, the minimum radius of curvature of a crack is approximately of the order of the interatomic distance. Nevertheless, in real materials the stress at the crack tips can assume very large values, as compared with the loads.

The conceptual importance of the Inglis result can be summed up as follows: *in a real material, the failure can occur for an applied stress that is much lower than the theoretical failure stress σ_f because the crack works as a stress concentrator.* Therefore, it is possible that an applied stress $\sigma < \sigma_f$ could be amplified locally and exceed the theoretical failure stress σ_f , thereby generating the crack propagation (failure of the system). As mentioned, a material that contains a slit crack theoretically should fail on the application of an infinitesimally small load. This paradox has motivated other researchers to develop a fracture theory based on a detailed energy balance rather than on local stress.

The Griffith Energy Criterion

The energy balance criterion developed by Griffith¹² relies on the elementary observation that the system must release energy upon cracking. In other words, a crack only can propagate under loading if there is a net decrease in the total energy. We consider the system shown in Figure 9 where a slit crack with half-length L can grow ($L \rightarrow L + dL$) under the effect of the applied load σ . This occurs only if the variation of the total energy dE_t for a length variation dL is negative:

$$\frac{dE_t}{dL} \leq 0 \tag{130}$$

The growth process of the crack generates the formation of a new internal surface dA for any length variation dL of the crack itself. We now observe that the total energy E_t of the system with a crack subject to traction can be written as the sum of two contributions, namely: a surface energy term E_s and an elastic energy term W_i (elastic energy of the body under load):

$$E_t = E_s + W_i \tag{131}$$

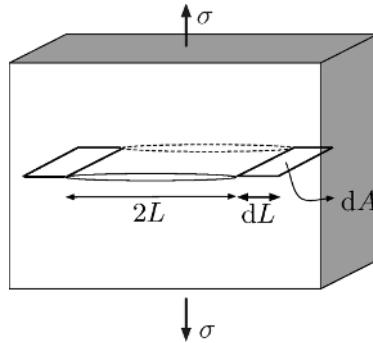


Figure 9 A slit crack with half-length L undergoes a growth of length $2dL$ under the applied stress σ .

The first contribution describes the work needed to create a new surface, and the second one takes into account the variation of elastic energy in the system resulting from the crack growth. From Eqs. [130] and [131] we get the following:

$$-\frac{dW_i}{dL} \geq \frac{dE_s}{dL} \quad [132]$$

The above energy balance can be developed further only if we can calculate explicitly W_i and E_s .

The surface energy E_s is given by:

$$E_s = 4LH\gamma_s \quad [133]$$

where H is the thickness of the plate under consideration and γ_s is the surface energy, considered here as a characteristic parameter of the material measuring the work needed to break the chemical bonds along the surface of the crack. It is important to remark that, in principle, the determination of γ_s is a typical materials physics problem. However, within LEFM, it is customary to identify γ_s with the ideal surface cleavage energy. This choice will be adopted here, but it will be readdressed critically in the next section.

By considering a linear elastic material with Young modulus E and Poisson ratio ν , Griffith used the stress analysis of Inglis to prove that:⁷⁵

$$W_i = -\frac{\pi HL^2 \sigma^2}{E'} \quad [134]$$

where E' is the effective Young modulus defined as follows:

$$E' = \begin{cases} E & \text{in } \textit{plane stress} \text{ conditions} \\ \frac{E}{1-\nu^2} & \text{in } \textit{plane strain} \text{ conditions} \end{cases} \quad [135]$$

By substituting Eqs. [133] and [134] in Eq. [132], we obtain the physical condition under which the slit crack (with initial half-length $2L$) can propagate within a brittle material under applied load σ :

$$\sigma \geq \sqrt{\frac{2\gamma_s E'}{\pi L}} \tag{136}$$

The result given in Eq. [136] allows us to state that for a slit crack, a threshold value exists for the applied load generating the growth of the crack and, therefore, the failure of the system. When $\sigma = \sqrt{\frac{2\gamma_s E'}{\pi L}}$, we are in a situation of unstable equilibrium.

Opening Modes and Stress Intensity Factors

The geometric configuration described for introducing the Inglis stress enhancement (see Figure 8) and the Griffith stability criterion (see Figure 9) is, within the framework of LEFM, named the *in-plane opening mode* or Mode I (a tensile stress normal to the plane of the crack). There are at least two other important geometric configurations to be considered, namely: a crack can be stimulated by means of the *in-plane shearing mode* or Mode II (a shear stress acting parallel to the plane containing the crack and perpendicular to the crack front) or through the *anti-plane shearing opening* or Mode III (a shear stress acting parallel to the plane containing the crack and parallel to the crack front). The three opening modes are shown in Figure 10, where the corresponding loading is indicated as well.

All atomistic investigations on fracture-related phenomena described in the next section are performed in the Mode I configuration. It is therefore useful to thoroughly characterize the behavior of the stress field $\hat{T}^{(I)}$ near a crack tip in the Mode I configuration. To this aim, we introduce a system of polar coordinates (r, ρ) centered at the tip of the slit crack, as shown in Figure 11. In

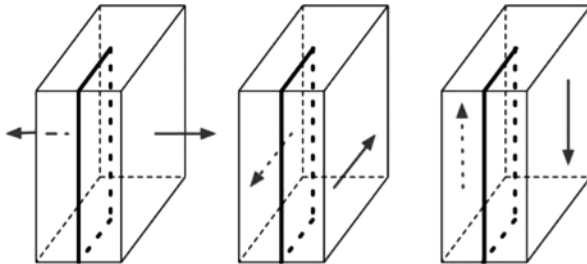


Figure 10 Typical modes of opening for a crack: Mode I is the *in-plane opening mode*, Mode II is the *in-plane shearing mode*, and Mode III is the *anti-plane shearing opening*.

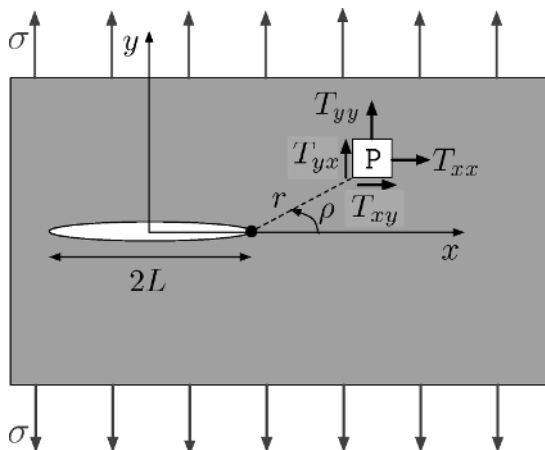


Figure 11 Components T_{xx} , T_{yy} , and $T_{xy} = T_{yx}$ of the stress tensor at the point P near the crack tip. The polar coordinates (r, ρ) are centered at the crack tip itself.

particular, we want to determine the components T_{xx} , T_{yy} , and $T_{xy} = T_{yx}$ of the stress tensor near the crack tip.

It has been proved^{11,77} that the stress components contain a leading term proportional to $1/\sqrt{r}$. As $r \rightarrow 0$, the leading term approaches infinity, accounting for the stress singularity and intensification. It also can be shown that the displacement near the crack tip varies with \sqrt{r} . The asymptotic form of stress near the crack tip is given by the following relation:

$$\lim_{r \rightarrow 0} T_{ij}^{(I)} = \frac{K_I}{\sqrt{2\pi r}} f_{ij}^{(I)}(\rho) \quad [137]$$

where $i, j = x, y$. The function $f_{ij}^{(I)}(\rho)$ represents a geometric dimensionless function of the angle ρ ,^{11,77} and the quantity K_I is called the stress intensity factor in Mode I.

The most important component of the stress tensor is T_{yy} , (i.e., the stress along the applied load). It is possible to prove that the behavior of such a quantity, as a function of the variable x , is given by:^{11,77,79}

$$T_{yy}(x, 0) = \frac{|x|\sigma}{\sqrt{x^2 - L^2}} \quad [138]$$

as shown in Figure 12. This result is valid for both plane strain and plane stress border conditions. For any value of σ , the stress component T_{yy} is singular at the crack tips (i.e., for $x \rightarrow \pm L$), as one can observe both in Eq. [138] and in Figure 12. Moreover, when we are far away from the crack (i.e.,

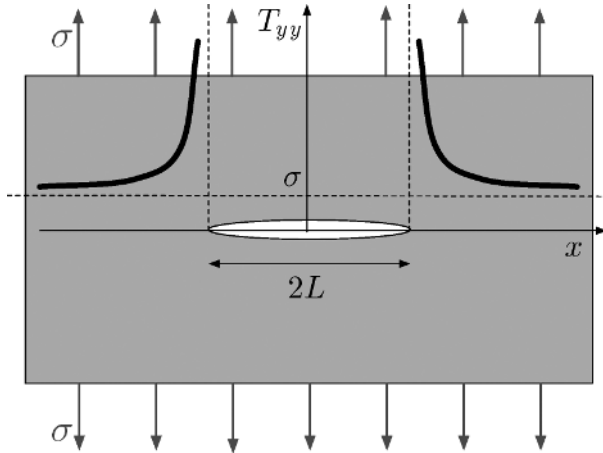


Figure 12 Behavior of the T_{yy} component of the stress field as a function of the variable x . The asymptotic value σ corresponds to the remotely applied load.

for $x \rightarrow \pm\infty$) the stress T_{yy} approaches the value σ of the remotely applied load. Eq. [138] allows us to identify the stress intensity factor in Mode I as follows:

$$K_I = \lim_{x \rightarrow L} T_{yy}(x, 0) \sqrt{2\pi(x-L)} = \sigma \sqrt{\pi L} \quad [139]$$

This explicit expression shows that the intensity factor K_I is independent of the elastic moduli of the cracked material, and, therefore it represents a very general concept.

An additionally important quantity in fracture mechanics is introduced by calculating Eq. [139] at the Griffith critical value $\sigma = \sqrt{\frac{2\gamma_s E'}{\pi L}}$ for the applied stress. We simply obtain the following:

$$K_{I,c} = \sqrt{2E'\gamma_s} \quad [140]$$

which is called *fracture toughness*. Its value depends only on material parameters and its meaning is the following: failure or fracture growth only occurs when $K_I > K_{I,c}$. The stress intensity factor and the fracture toughness can be expressed in units of $\text{Pa} \cdot (\text{m})^{1/2}$.

Some Three-Dimensional Configurations

In the previous sections, we have discussed the properties of a crack under the assumption of plane stress or plane strain. Therefore, we have discussed the

results only taking into account two-dimensional geometries. In this section, we describe some results concerning the behavior of the elastic fields around a crack in two three-dimensional configurations: the slit and the circular (penny-shaped) crack. These canonical problems contain almost all features related to the stress and strain fields of interest in linear elastic fracture mechanics.⁷⁷

We start with the slit crack (see Figure 13] in a three-dimensional environment under the applied stress $T_{22} = \sigma$, where σ represents the tensile stress applied in Mode I along the x_2 direction, as represented in Figure 13 on the right. The corresponding displacement field recently has been calculated⁸⁰ by means of a methodology based on the Eshelby theory,^{29,81,82} not discussed here. We get the following:

$$u_1 = -\frac{\sigma x_1 (1 + \nu)}{E} \left[\frac{1 - 2\nu^2}{1 + \nu} - \frac{\beta}{\alpha} \sqrt{\frac{\eta}{L^2 + \eta}} \right] \quad [141]$$

$$u_2 = \frac{\sigma x_2 (1 + \nu)}{E} \left[\frac{\nu(1 + 2\nu)}{1 + \nu} + \frac{\beta}{\alpha} \sqrt{\frac{L^2 + \eta}{\eta}} \right] \quad [142]$$

$$u_3 = -\frac{\sigma \nu x_3}{E} \quad [143]$$

Recall that the slit-crack is aligned along the x_3 axis, and the two surfaces of the crack lie on the plane (x_1, x_3) ; it follows that the component u_3 is not affected by the presence of the slit crack. The parameters α , β , and η are listed as

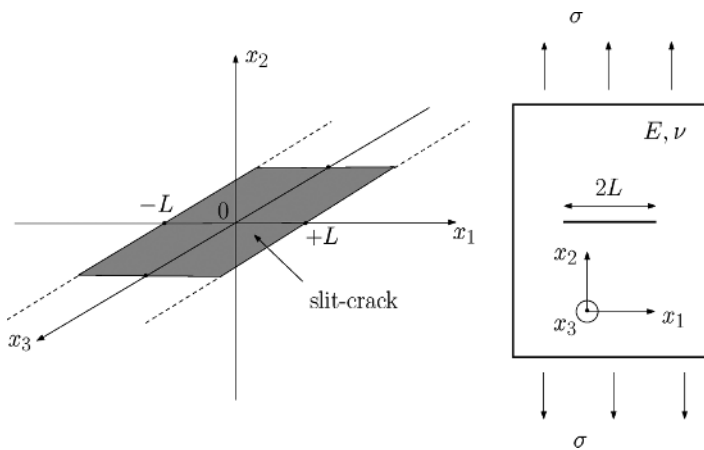


Figure 13 Left panel: geometry of a slit crack lying in the (x_1, x_3) plane. Right panel: elastic medium (with Young modulus E and Poisson ration ν) containing a slit crack (with length $2L$) under uniaxial stress σ (along x_2).

follows:

$$\begin{aligned}\alpha &= x_1^2 \eta^2 + x_2^2 (L^2 + \eta)^2 \\ \beta &= (1 - 2\nu) (x_1^2 + x_2^2) \eta^2 + 2(1 - \nu) x_2^2 L^4 + (3 - 4\nu) x_2^2 L^2 \eta \quad [144] \\ \eta &= \frac{1}{2} (x_1^2 + x_2^2 - L^2) + \frac{1}{2} \sqrt{(x_1^2 + x_2^2 + L^2)^2 - 4L^2 x_1^2}\end{aligned}$$

Eqs. [141], [142] and [143] are important because they describe in a very compact form the displacement field in the whole space, and they contain, as particular cases, all standard LEFM results, including those described previously.

Eqs. [141], [142] and [143] can be used in several ways to analyze the behavior of a crack. For example, it is easy to calculate the strain or the stress tensor just in some regions of interest by using the constitutive relation of the matrix. Here, we do not report the expressions for strain and stress because they are very complicated and do not add any conceptual content to the present discussion. Rather, we focus on the T_{22} component of the stress, which is reported in Figure 14. It is interesting to note the two singularities appearing at the crack tips, showing the typical intensification of the stress. When $x_2 = 0$, we obtain the well-known result $T_{22} = \frac{|x_1| \sigma}{\sqrt{x_1^2 - L^2}}$ if $x_2 \rightarrow 0$, $|x_1| > L$, as described in a previous section. This result is important because it naturally drives to the concept of stress intensity factor (previously introduced in Eq. [139]) by obtaining $K_I = \sigma \sqrt{L\pi}$.

We now can consider the circular or penny-shaped crack shown in Figure 15. In this case, we assume that the external forces are characterized by a

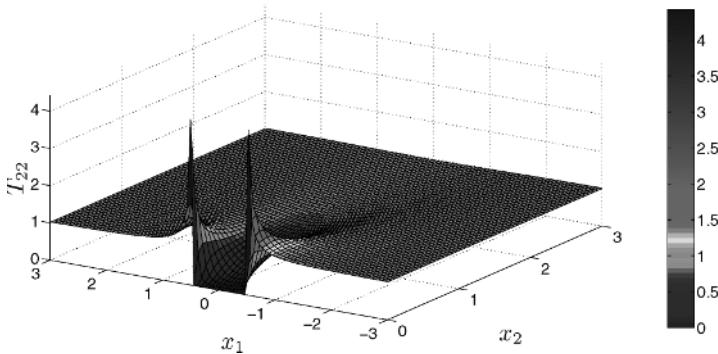


Figure 14 Tensile stress field T_{22} along x_2 in a slit crack. We have assumed the values: $E = 1$, $\sigma = 1$, $\nu = 0.33$, and $L = 0.5$ in arbitrary units. The region under consideration is described by $-3 < x_1 < 3$ and $0 < x_2 < 3$. The results are represented for plane stress conditions. The intensity of T_{22} in arbitrary units is given in the vertical direction.

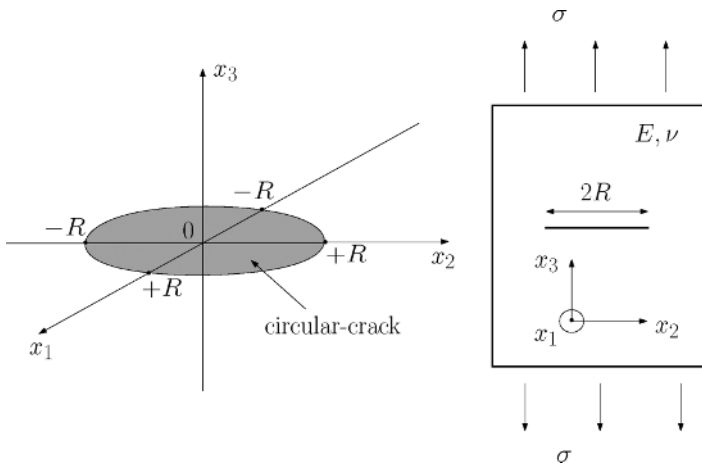


Figure 15 Left panel: geometry of a circular crack lying in the (x_1, x_2) plane. Right panel: elastic medium (with Young modulus E and Poisson ratio ν) containing a circular crack (with radius R) under uniaxial stress σ (along x_3).

tensile stress $T_{33} = \sigma$. To describe the resulting three-dimensional displacement field, it is useful to introduce a system of polar cylindrical coordinates (ρ, θ, x_3) , where $x_1 = \rho \cos(\theta)$ and $x_2 = \rho \sin(\theta)$. For the symmetry of our system, the final results will not depend on the angle θ . The explicit result describing the total displacement u_ρ and u_3 is given as follows:

$$u_\rho = -\frac{\sigma\rho(1+\nu)}{2E} \left[(1-2\nu) \left(\frac{(1+2\nu)(1-\nu)}{(1-2\nu)(1+\nu)} - \frac{2}{\pi} \arctan \frac{\sqrt{\eta}}{R} \right) - \frac{2}{\pi} \frac{\beta}{\alpha} \frac{R\sqrt{\eta}}{R^2 + \eta} \right] \quad [145]$$

$$u_3 = \frac{\sigma x_3(1+\nu)}{E} \left[(1-2\nu) \left(\frac{\nu(1+2\nu)}{(1+\nu)(1-2\nu)} + \frac{2}{\pi} \arctan \frac{\sqrt{\eta}}{R} \right) + \frac{2}{\pi} \frac{\beta - x_3^2 R^2 (R^2 + \eta)}{\alpha} \frac{R}{\sqrt{\eta}} \right] \quad [146]$$

where the variable u_ρ represents the radial displacement and $u_\rho^2 = u_1^2 + u_2^2$ is the radius $\rho = \sqrt{x_1^2 + x_2^2}$. We also have introduced the axial displacement u_3 and the following definitions:

$$\alpha = \rho^2 \eta^2 + x_3^2 (R^2 + \eta)^2$$

$$\beta = (1 - 2\nu)(x_3^2 + \rho^2)\eta^2 + 4(1 - \nu)\eta x_3^2 R^2 + (3 - 2\nu)x_3^2 R^4 \quad [147]$$

$$\eta = \frac{1}{2} \left(x_3^2 + \rho^2 - R^2 \right) + \frac{1}{2} \sqrt{(x_3^2 + \rho^2 + R^2)^2 - 4R^2 \rho^2}$$

The stress T_{33} along the direction of the Mode I loading is reported in Figure 16. It is interesting to observe that for $\rho = R$, $x_3 = 0$ (i.e., on the circumference of the crack), we have a singularity describing the stress intensification on the circular crack front. The quantity T_{33} can be specialized on the plane of the circular crack $x_3 = 0$ and for external radius $\rho > R$, obtaining the following:

$$T_{33}(\rho) = \frac{2\sigma}{\pi} \left[\frac{R}{\sqrt{\rho^2 - R^2}} + \arctan \frac{\sqrt{\rho^2 - R^2}}{R} \right] \quad [148]$$

This relation represents the analog of the slit-crack formula (see Eq. [138]), for a circular crack. Similarly, we can evaluate the stress intensity factor. For the circular crack, the distance from the border of the crack is given by $\rho - R$, and the stress intensity factor is calculated as follows:

$$K_I = \lim_{\rho \rightarrow R, x_3 \rightarrow 0} \sqrt{2\pi(\rho - R)} T_{33} = \frac{2\sqrt{R}}{\sqrt{\pi}} \sigma \quad [149]$$

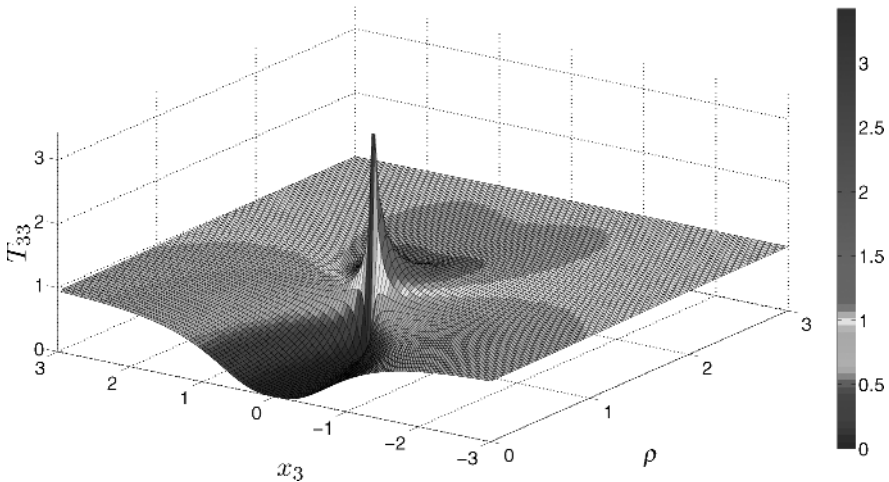


Figure 16 Tensile stress field T_{33} along x_3 in a circular crack. We have assumed the values: $E = 1$, $\sigma = 1$, $\nu = 0.33$, and $R = 1$ in arbitrary units. The region under consideration is described by $-3 < x_3 < 3$ and $0 < \rho < 3$. The results are represented for plane stress conditions. The intensity of T_{33} in arbitrary units is given in the vertical direction.

To conclude, we point out that the stress intensity factor depends on the geometry of the system under consideration.

Elastic Behavior of Multi Fractured Solids

We described the stability and the stress behavior of a single crack in a given brittle material in the previous section. Here, we discuss the effects of a given population of cracks on the mechanical or elastic behavior of an elastic body (degradation). Although linear elastic fracture mechanics, as stated above, provide the basic understanding of the failure instability for a single crack, the overall mechanical behavior of a multicroaked body actually depends on the positional and orientational distribution of an assembly of cracks. When considering the overall behavior of materials,^{83,84} a key conceptual issue involves the effective elastic properties that determine the mechanical performance of the system containing a given distribution of cracks.^{85,86}

We consider a region of the plane $z - y$ having area A and containing N slit-cracks having half-length a and uniform angular distribution on the plane (see Figure 17). We can define the characteristic quantity $\alpha = \frac{\pi a^2}{A} N$; it is dimensionless, and it effectively represents the crack density over the area A . To define the effective stiffness tensor of the microcracked system, it is important to compute the average values of the strain tensor $\langle \hat{\epsilon} \rangle$ and of the stress tensor $\langle \hat{T} \rangle$ throughout the whole region of interest (i.e., area A). Therefore, we define the effective stiffness tensor \hat{C}_{eff} of the cracked body through the relation $\langle \hat{T} \rangle = \hat{C}_{eff} \langle \hat{\epsilon} \rangle$.

We review the results under the conditions of plane stress or plane strain. The material will be described by the effective moduli E_{eff} and ν_{eff} . Under the hypothesis of low crack density, we obtain the effective elastic moduli in the plane stress case and their first order expansions in the density parameter α ,

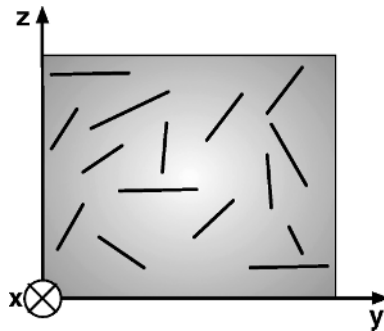


Figure 17 Structure of a multicroaked solid with randomly oriented slit-cracks aligned along the x -axis.

which are expressed as follows:

$$\begin{aligned}
 E_{\text{eff}} &= \frac{E}{1 + \alpha(1 - \nu^2)} \cong E[1 - \alpha(1 - \nu^2)] \\
 \nu_{\text{eff}} &= \frac{\nu}{1 + \alpha(1 - \nu^2)} \cong \nu[1 - \alpha(1 - \nu^2)]
 \end{aligned}
 \tag{150}$$

We observe that Eq. [150] holds true only for low values of the crack density N/A that appear in the parameter α . We describe the differential method to extend the applicability of the theory to higher values of the crack density. Let us suppose that the effective moduli of a microcracked medium are known to be E_{eff} and ν_{eff} . Now, if a small additional number of cracks ΔN is created in the matrix, the change in the elastic moduli is approximated to be that which develop if the same infinitesimal number of cracks were added to a uniform, homogeneous matrix with moduli E_{eff} and ν_{eff} . This leads, when applied to Eq. [150], to the following final results for isotropic two-dimensional elasticity in plane stress conditions:

$$\begin{aligned}
 E_{\text{eff}} &= \frac{E}{\sqrt{\nu^2 + (1 - \nu^2) e^{2\alpha}}} \\
 \nu_{\text{eff}} &= \frac{\nu}{\sqrt{\nu^2 + (1 - \nu^2) e^{2\alpha}}}
 \end{aligned}
 \tag{151}$$

Moreover, again under the hypothesis of low crack density, we obtain the equivalent elastic moduli under the plane strain condition and their first-order expansions in the parameter α as follows:

$$\begin{aligned}
 E_{\text{eff}} &= E \frac{[1 + \nu + \alpha(1 - \nu)]}{[1 + \alpha(1 - \nu)]^2(1 + \nu)} \cong E \left[1 - \alpha \frac{(1 - \nu)(1 + 2\nu)}{1 + \nu} \right] \\
 \nu_{\text{eff}} &= \frac{\nu}{1 + \alpha(1 - \nu)} \cong \nu[1 - \alpha(1 - \nu)]
 \end{aligned}
 \tag{152}$$

As before, knowing the first-order expansions is useful for applying the differential method, which leads to the following solutions:

$$\begin{aligned}
 E_{\text{eff}} &= E \frac{2\nu + (1 - \nu) e^\alpha}{[\nu + (1 - \nu) e^\alpha] r(1 + \nu)} \\
 \nu_{\text{eff}} &= \frac{\nu}{\nu + (1 - \nu) e^\alpha}
 \end{aligned}
 \tag{153}$$

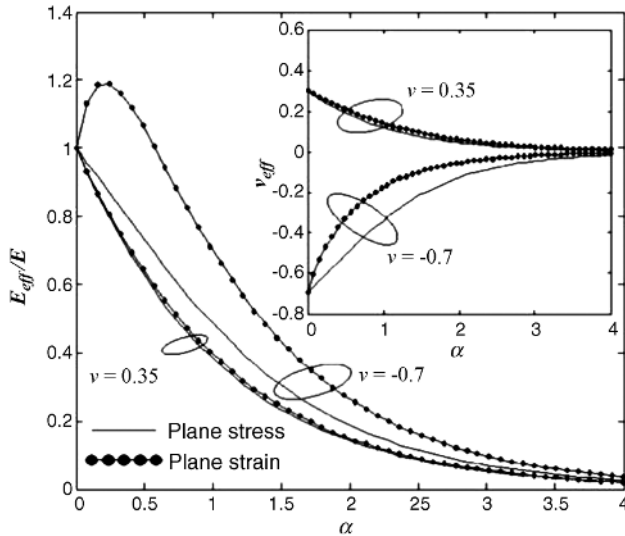


Figure 18 Effective Young modulus and Poisson ratio for a multicroaked solid under plane stress and plane strain conditions. The plots have been derived for two different homogeneous matrices having $\nu = 0.35$ and $\nu = -0.7$.

It is important to observe that the solutions given by Eq. [151] for plane stress and by Eq. [153] for plane strain depend, exponentially, on the crack density; in particular, the effective Young modulus of a multicroaked solid decreases exponentially with increasing density of cracks.

In Figure 18, these results have been represented versus the parameter α . A comparison between the plane stress and the plane strain cases has been drawn both for the positive and negative Poisson ratio. An interesting and unexpected behavior in a multicroaked solid has been found under plane strain condition when its Poisson ratio is negative. As a matter of fact, when α is small enough and $-1 < \nu < -1/2$, we obtain an effective Young modulus greater than the Young modulus of the original elastic matrix. This effect is shown in Figure 18 where a value $\nu = -0.7$ is assumed. This effect is not present under plane stress conditions. The unusual behavior observed in plane strain conditions can be attributed to the specific meaning of the Young modulus in such a case; the elastically loaded plain strain system has fewer degrees of freedom than the system in plane stress because of the peculiar boundary conditions needed to avoid the appearance of out-of-plane strain in the solid.

Atomistic View of Fracture

The first molecular simulation of fracture dynamics probably was carried out by Weiner and Pear.⁸⁷ They used a square lattice of atoms, inserted a crack in

its middle, and solved the equation of motion for the atoms. They also assumed that if the distance between two atoms becomes too large then those atoms can be considered as being disconnected. Simulations were performed both at zero and nonzero temperatures. Weiner and Pear found that, except at very high applied stresses, the velocity of the crack reaches a steady subsonic and stress-dependent value, which is in agreement with the prediction of continuum fracture mechanics.

Another molecular-like simulation of fracture was carried out by Ashurst and Hoover.⁸⁸ They used a triangular lattice in which the atoms interacted with each other by a truncated Hooke-like force. The most important finding of this study was that the velocity of the crack never reaches the Rayleigh wave speed, consistent with the difficulties that linear continuum mechanics of fracture dynamics previously had for explaining the experimental data of fracture propagation speed.

Thomson, Hsieh, and Rana⁸⁹ presented evidence for lattice trapping, a phenomenon in which a crack neither propagates nor heals; rather, it remains stable until external loads somewhat larger than the Griffith threshold are imposed on the system. The magnitude of the trapping range depends strongly on the characteristics of atomic bonding of materials. Lattice trapping also may depend on the direction in which the crack tip bonds are broken and, therefore, may be different for fracture propagation along different crystallographic directions. This model consists of a quasi-one-dimensional chain model comprised of two semi-infinite chains of point atoms bonded longitudinally by linear elastic elements and transversely ahead of the crack tip by stretchable elements ($n = 1, 2, \dots$). An opening load σ is applied to the system. When a transversal bond is stretched beyond the cut-off displacement $u_n = \delta$, it is considered to be broken. The mathematical solution of this model allows us to define a crack tip force function F_n : for $F_n > 0$, the bond opens, and for $F_n < 0$, it closes. This force takes into account the interaction between the lattice and the applied load. The function $F_n(u_n)$ (force-separation function) is represented in Figure 19. The load σ^+ is the force needed to obtain $u_n = \delta$ (crack extension), and the load σ^- corresponds to $u_{n-1} = \delta$ (crack healing).

The function $F_n(u_n)$ has three equilibrium or stationary points I, II, and III where $F_n(u_n) = 0$. The points I and III are stable; at I the bond remains intact, and at III the bond is broken. The state II is unstable; within the load range $\sigma^- < \sigma < \sigma^+$, the crack is mechanically trapped by the lattice. In this condition, it cannot move either forward or backward under the action of the load alone. This phenomenon persists also for cracks at macroscopic dimensions.

The first truly molecular dynamics (MD) simulations⁹⁰ of crack propagation were carried out by Paskin, Som, and Dienes.^{91,92} We call their computations true MD simulations because, unlike Ashurst and Hoover,⁸⁸ they used the LJ potential for representing the interactions between the atoms in a triangular lattice. In their simulations, a crack was inserted into the middle of the lattice to initiate fracture propagation. An external force then was applied to the

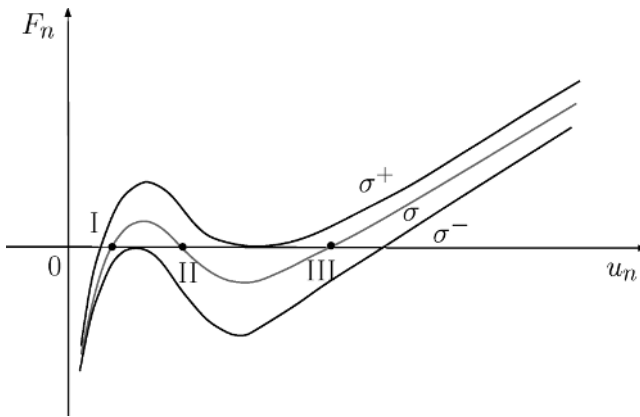


Figure 19 Graphical representation of the crack tip force function (lattice bond rupture force) F_n versus cut-off displacement u_n for different loads σ^- , σ , and σ^+ . The equilibrium points I and III are stable, whereas point II is unstable.

lattice, and Newton's equations of motion were solved to calculate the atomic positions, velocities, and forces. The cut-off for the LJ potential was assumed to be slightly smaller than two lattice bonds at equilibrium. This investigation showed that the Griffith energy criterion is incorrect for large cracks. The MD simulations also indicated that lattice trapping is a negligible effect, which was attributed to the long range of the interaction potentials. However, in general, one should expect lattice trappings to disappear at temperatures larger than room temperature, and therefore, to observe this phenomenon, experiments and MD simulations must be carried out at very low temperatures. The necessity of a low temperature explains why no lattice trapping has yet been observed experimentally in either crystalline or amorphous materials.

In addition to the work by Paskin, Som, and Dienes, interesting MD computations were carried out by Soules and Busbey⁹³ to study the fracture of sodium silicate fiber glass. Instead of using interatomic forces that result from LJ potentials, these authors used a modified semi-empirical equation. Simulations done by Soules and Busbey⁹³ indicated that the glass breaks when it is suddenly subjected to a large biaxial expansion. Moreover, when the temperature of the system is raised by about one order of magnitude, the strength of the material decreases by a factor of about two, a result that was claimed to be in agreement with experimental data.

To our knowledge, Ray and Chakrabarti^{94,95} and Chakrabarti, Chowdhury, and Stauffer⁹⁶ were the first to carry out MD simulations of fracture involving a model of materials with quenched disorder. A percolation-type disorder was used (i.e., the heterogeneity was generated by breaking some of the bonds between the atoms randomly before the simulations commenced). A LJ potential was used, for which the cut-off distance was set to 1.6 times

the bond length. During deformation of the lattice, a bond was considered to be broken if the distance between its end atoms was larger than the cut-off distance. Chakrabarti and coworkers found that the stress needed for fracture vanishes, and the time to complete fracture diverges both at the bond percolation threshold of the lattice.

Cheung and Yip,⁹⁷ employing the embedded-atom potential, studied the response of a crystal containing a sharp fracture to varying stress and temperature. Over a limited range of temperature, a transition from brittle to ductile fracture was observed, caused by dislocation emission from the tip of the fracture. This result indicated the existence of an energy barrier for nucleation of the dislocation.

Model potential MD has been used extensively to study various crack-related phenomena, including the brittle-to-ductile transition⁴² and the dynamic brittle fracture.⁴³ Furthermore, fracture mechanics was studied in perfect crystals,⁹⁸ as well as in nanostructured systems like, for example, nanocrystalline nickel.⁹⁹ Finally, although a quantitative agreement between atomistics and the continuum was discussed in Ref. 98 as for the Griffith criterion, multi-million atom MD simulations clarified several complementary aspects of crack propagation in brittle materials.¹⁰⁰

Despite the successful applications of model potential MD, the deficiencies of the available empirical force fields (see “Interatomic Potentials for Solid Mechanics”) stimulated the search for improved models based on a better description of the chemical bonding (possibly at a quantum mechanical level). Two paths have been explored in particular. The first was to study the whole atomistic system by the same quantum mechanical interaction scheme using *ab initio*^{101–103} or tight-binding¹⁰⁴ methods. However, because of their high computational workload, *ab initio* methods were focussed successfully just on a specific issues like, for example, the calculation of the surface energy¹⁰¹ appearing in Eq. [136] or the characterization of the quasi-static crack opening.¹⁰⁵

A second pathway to go beyond the limits of model potentials is to use a multiscale approach.^{106,107} The idea is that the different length scales, involved in the fracture phenomena, are described by using different methods.¹⁰⁶ In this theoretical framework, the classic force model is used far from the crack tip, whereas the chemical bonding nearby the crack tip is described by semi-empirical tight binding⁵⁸ or by *ab initio* density functional calculations.¹⁰⁸ Alternatively, the model potential is modified locally through a learn-on-the-fly procedure.¹⁰⁹ More recently, a multiparadigm approach has been proposed¹¹⁰ in which a reactive force field is applied at the crack tip. Such a method has been applied to the case of silicon as well as to biological materials such as proteins.¹¹¹ The multiscale approach is probably the most promising method to achieve an accurate modeling of fracture at the atomic scale. A detailed discussion about the historic development of molecular dynamics simulations of fracture propagation and the comparison with continuum theories can be found in Refs. 112, 113.

ATOMISTIC INVESTIGATIONS ON BRITTLE FRACTURE

Conceptual Layout

We focus on cubic silicon carbide (β -SiC) because it is the prototype of an ideally brittle material up to extreme values of strain, strain rate, and temperature as well as because of its technologic relevance as a structural and nuclear material. All examples discussed in this section will refer to SiC for the sake of consistency; in this way, it will be possible to work out a complete and thorough picture about the many aspects of brittle fracture on a common basis. More specifically, all results presented in the following sections have been obtained with the same interaction potential, simulation protocol, and computational device. So, these results can provide an illuminating perspective about the role of atomistic simulations in this field.

We will make extensive use of the continuum concepts developed in the “Essential Continuum Elasticity Theory” and in “Linear Elastic Fracture Mechanics” sections and whereas the atomistic analysis of the stress-related quantity is based on the virial formulation presented in “Linear Elastic Fracture Mechanics”. In any case, atomic forces were calculated according to the Tersoff model. Such an empirical interatomic potential already has been applied extensively to the study of mechanic properties in β -SiC and it can describe the experimentally observed brittle behavior of cubic β -SiC.^{57,114} Furthermore, this force field nicely fits the requirements specifically described in the “Interatomic Potentials for Solid Mechanics” section.

Griffith Criterion for Failure

Continuum Versus Atomistics

The Griffith criterion for a bulk specimen given in Eq. [136] is readdressed here by simulating mode-I loading on the sample represented in Figure 20.¹¹⁵ The crack arrangement is selected as illustrated because the lowest unrelaxed surface energy of β -SiC is found on the (111) shuffle plane,¹¹⁴ and therefore, the (111)-plane cracks are the most likely to form under experimental conditions. The simulation cell has the x , y , and z cartesian axes parallel to the $[11\bar{2}]$, $[\bar{1}10]$, and $[111]$ crystallographic directions, respectively. Therefore, the crack front lies parallel to the¹¹² direction. In other words, the crack arrangement is (111).¹¹²

The typical macroscopic conditions of a quasi-static (or adiabatic) crack loading process at $T = 0$ K are reproduced by applying external surface forces to the nonperiodic borders of the simulation cell. This is performed by using the constant traction method by Cleri.¹¹⁶ Atomic positions were relaxed, at any applied load condition, by constantly damping velocities to zero, until the

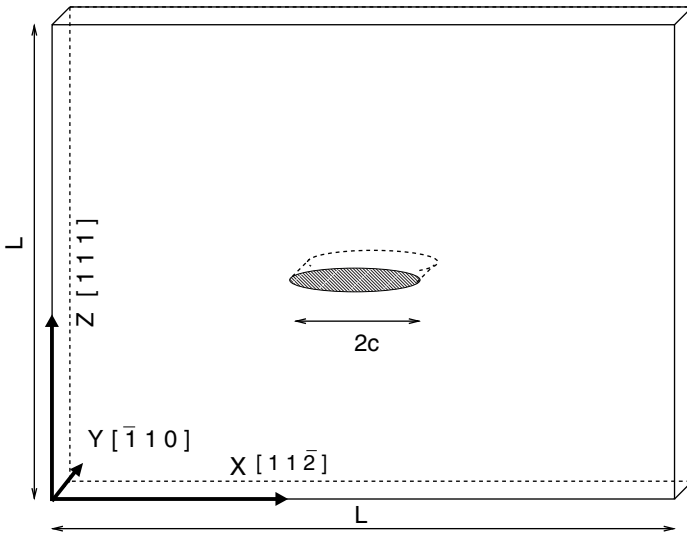


Figure 20 Geometry and orientation of the simulation cell. In the present simulations, $22 \text{ nm} < L < 88 \text{ nm}$. The shaded area represents the crack position.

maximum force was less than 0.0001 eV/\AA . We took special care to avoid finite-size effects, by setting the size of the simulation cell so as to achieve a ratio of $L/c > 10$ (see Figure 20). The resulting number of atoms contained in our simulation cell ranged from 3×10^4 to 2.5×10^5 .

The loading procedure involved four steps: (1) the three-dimensional periodic simulation box initially was deformed along the z direction, corresponding to a given strain value $\epsilon = \epsilon_{[111]}\delta_{zz}$ while keeping $\epsilon_{xx} = 0$ and $\epsilon_{yy} = 0$ (we remark that this configuration corresponds to a plane-strain border condition, as discussed in the ‘‘Governing Equations of Elasticity and Border Conditions’’ section); (2) periodicity then was removed along z and surface tractions were calculated to preserve the state of deformation; (3) a microcrack of given length was introduced by cutting the interatomic bonds across a segment of a central (111) plane (or, equivalently, by setting to zero the pair interactions across that plane); (4) the actual minimum-energy atomistic configuration was obtained by damped-dynamics. After crack opening, interatomic forces are fully restored, and the microcrack reaches its equilibrium shape after stress relaxation.

A series of atomistic simulations was performed with microcracks of length $2c_0 < 2c < 50c_0$, where $c_0 = 2.644 \text{ \AA}$ is the interbond distance along the 112 direction (see Figure 20). According to Eq. [136], the critical load increases with decreasing microcrack length. This implies that, for the Griffith theory to be valid, the limits of applicability of linear elasticity must be respected. Such a requirement defines implicitly the minimum length at which a finite-size microcrack still can be considered a ‘‘Griffith crack’’ this length corresponds to $c = 2c_0$ in our investigation.

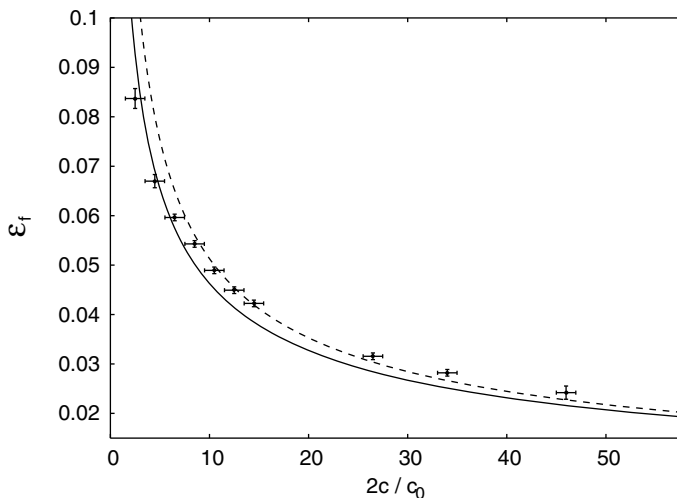


Figure 21 Critical strain, ϵ_f , as a function of the crack size, $2c$, in units of the $[11\bar{2}]$ interbond distance c_0 . Symbols are the data from atomistic simulations; the continuous line is Griffith's theory with constant material parameters, and the dashed line is the modified Griffith's theory, see text. The horizontal error bars in the figure are a result of the lattice spacing orthogonal to the crack front, whereas the vertical error bars are a result of the steps chosen to vary the strain, $\Delta\epsilon = 0.001$.

We report the values of the calculated critical strain ϵ_f of SiC as a function of microcrack length and the corresponding prediction of the continuum Griffith theory in Figure 21. The Young modulus and the Poisson ratio values are provided in both cases by the Tersoff potential. Consistent with the expected brittle behavior, we found that the microcrack extends in a perfectly brittle way at loads above the critical strain (i.e., by preserving atomically smooth (111) cleavage surfaces). On the other hand, no rehealing of the microcrack edges ever was observed in our simulations at subcritical values of the load (i.e., the microcrack does not revert back to the perfect crystal). This latter observation is a result of the relaxation of the free surface created by the microcrack, which entails both a slight energy decrease and a variation of the optimum bond angles from the perfect tetrahedral arrangement.

Although the overall agreement between continuum and atomistic models shown in Figure 21 is remarkable, it is interesting to note that for microcracks longer than $\sim 10c_0$, the calculated critical strain is systematically higher than the Griffith theory prediction. To explain this result, it must be understood that the basic assumptions of the linear elastic fracture mechanics model underlying the Griffith data are not truly fulfilled by atomistic simulations, which indeed are based on an anharmonic force model. Two corrections to the standard Griffith model for SiC crack resistance, in fact, can be applied. These are: (1) the surface energy γ entering in Eq. [136] depends on the state of strain; (2) the stress-strain curve is not strictly linear across the range of explored loads (which amounts

to stating that the Young modulus is not constant). As for (1), it is easy to understand that the strain dependence of the surface energy can be computed straightforwardly by an atomistic model; simply, the surface energy must be computed for several ideal (i.e., noncracked) deformed samples, corresponding to each value of strain investigated in the Griffith problem. Similarly, the strain dependence of the Young modulus can be introduced straightforwardly into the continuum curve (interesting enough, this dependence is nonlinear for the range of investigated strains and crack lengths). The result of such a modified Griffith theory is reported in Figure 21 as a dashed line. The agreement between atomistic data and the modified Griffith theory is now much better, within the reported error bars. This demonstrates that identifying the crack resistance with the unstrained cleavage energy provides only a lower bound to the energy release rate (see “The Griffith Energy Criterion”).

Improving the Griffith Model

The previous conclusion is intriguing; according to standard Griffith’s theory, the surface energy—hereafter indicated as γ and representing the intrinsic crack resistance—does not depend on the crack length. Instead, it is a material constant. On the other hand, the corresponding atomistic quantity—hereafter indicated as γ_s —is actually affected by both loading (i.e., applied strain) and crack dimension. In Figure 22 we represent this concept by reporting the Griffith data

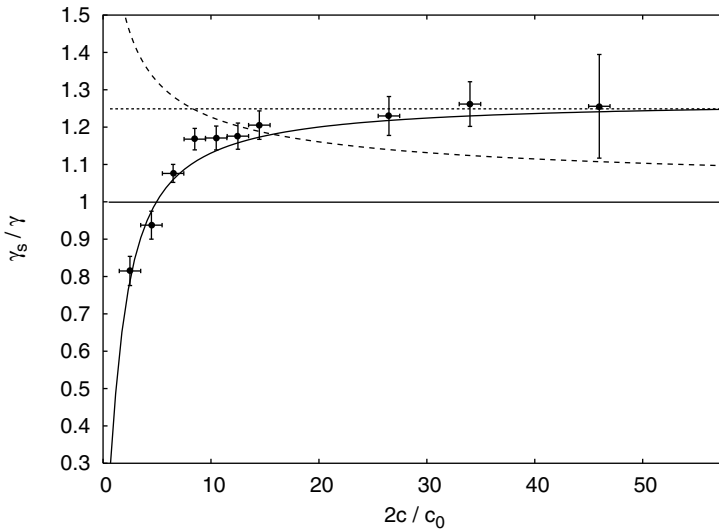


Figure 22 Crack resistance γ_s as a function of the microcrack length $2c$. Symbols are atomistic simulation data; the horizontal continuous line is the original Griffith theory; the long-dashed line is the modified Griffith theory, with strain-dependent surface energy and Young modulus; the continuous line is the fit to the DBCS elasto-plastic model. The horizontal short-dashed line at $\gamma_s/\gamma = 1.25$ represents the asymptotic value for the infinite crack intrinsic resistance estimated from atomistic simulations.

as a full line and the atomistic simulations by a long-dashed line. Let us, for the moment, focus on long cracks, corresponding to $2c/c_0 \geq 10$; although the modified Griffith theory grossly agrees with the atomistic data, a sizeable discrepancy is still evident, with a 25% departure from the classic Griffith theory (horizontal full line at $\gamma_s = \gamma$). However, a substantial part of this discrepancy is a result of the lack of an explicit strain dependence of the material parameters. In the modified Griffith theory, these strain dependences are included and provide a $\gamma_s = 1.10\gamma$ as the asymptotic limit, corresponding to the short-dashed line reported in Figure 22. The remaining discrepancy, therefore, must be attributed to a new feature, not yet discussed.

For very short microcracks of length of a few c_0 , the critical stress is so high that it becomes difficult to discriminate between bond breaking and incipient plasticity. A description of this regime can be attempted by a fit to an empirical elasto-plastic law, such as the Dugdale–Bilby–Cottrell–Swinden model (DBCS).¹¹⁷ In this case, the model fracture stress can be deduced by inverting the expression for the (unknown) crack tip displacement δ , as:

$$\sigma_f^D = \frac{2\sigma_M}{\pi} \cos^{-1} \left[\exp \left(-\frac{\pi\Delta}{4(1-\nu)c} \right) \right] \quad [154]$$

The lumped length parameter Δ should be equal to $\Delta = \mu\delta/\sigma_M$, with μ the shear elastic modulus, and σ_M the ideal cohesive strength, in the original DBCS model. The best fit of the DBCS model to the atomistic data is represented in Figure 22 by a continuous curve, merging with the atomistically corrected Griffith theory result at longer crack lengths. It is worth noting that, with the fitted values of the parameters, $\sigma_M = 53$ GPa and $\Delta = 2.3c_0$, we obtain an estimate of the crack tip opening $\delta \sim 0.7c_0$. This means that, for an ideally brittle material, the extent of a “plastic” zone in the incipient microcrack (a “flaw”) is, indeed, vanishingly small.

Failure in Complex Systems

A given material could be defined as “complex” if either its morphology or its mechanical behavior is considered. In the first case, we cope with its nanostructure, which in turn, makes it possible to classify the material itself as being a composite, fiber-reinforced, or defective material. In this respect, a complex material is a different mechanical object than the homogeneous medium found in elementary continuum mechanics. In the second case, we look at the complex response of a material to an arbitrary mechanical load, which could be elastic versus plastic or, when specifically addressing the failure behavior, could be brittle versus ductile. The actual response is a result of a complex hierarchy of phenomena, notably including the occurrence of nanodefects and their mutual interactions.

In both scenarios, complexity means the superposition of a rich variety of phenomena, possibly falling beyond the linear response regime. Among them, fracture phenomena play a key role in modern nanoscience. The theoretical and computational investigation of the such phenomena represents the core activity of present-day nanomechanics. In this section, we review some investigations on complex SiC-based systems.

Fracture Toughness in Fiber-Reinforced SiC

Ceramic materials are used widely for structural applications because of their low density, chemical inertness, high strength, high hardness, and stability at high temperature. Unfortunately, they also have a very low fracture toughness, a feature severely limiting their use for the most demanding applications.¹¹⁸ Ceramic matrix composites (CMC), consisting of a ceramic matrix reinforced with inclusions (e.g., particles, whiskers, or fibers), therefore, have been developed to overcome their intrinsic brittleness. This process is known as fiber reinforcing.

Within the large class of possible CMC structures, composites made of a carbon fiber distribution in a SiC matrix are mostly investigated.¹¹⁹ Carbon is, in fact, the optimal choice for the fiber in terms of stiffness, failure strength, and density. Also, a SiC matrix avoids compatibility problems with the carbon fiber, and it increases the oxidation resistance in oxidizing atmospheres.¹²⁰

Despite a considerable body of theoretical work (and, importantly enough, because of the unavoidable arbitrary assumptions of continuum modeling), the most fundamental features of fiber toughening in CMCs are still a matter of debate. In particular, it is not obvious if LEFM results can be extended (and, if so, to what extent) to the case of nanosized cracks and inclusions, as found in advanced CMC materials. We address here a key issue (among many others), namely: the stress intensification at a crack tip facing a nanosized fiber within a monocrystalline zincblend silicon-carbide matrix.¹²¹

The geometry of the simulated system (containing as many as 60,480 particles) is represented schematically in Figure 23. The crack is elliptically shaped (left) and aligned along the (111) shuffle plane for the reasons discussed in “Continuum Versus Atomistics”, whereas the x , y , and z cartesian axes (which also define the edges of our simulation cell) are parallel to the $[11\bar{2}]$, $[\bar{1}10]$, and $[111]$ crystallographic directions, respectively. A 1 nm large cylindrical fiber, which is softer (harder) than the matrix, was created by replacing a suitable number of carbon (silicon) atoms with the same number of silicon (carbon) atoms (see Figure 23). We remark that, because of the lattice mismatch between the inclusion (fiber) and the host matrix, a residual stress field results in the matrix even at $T = 0\text{K}$. The applied strain along the $[111]$ direction was obtained by surface tractions¹¹⁶ and varied in the 3–8% range. The geometry of Figure 23 corresponds to the plane strain condition.

For an isolated crack, LEFM predicts that the stress varies along the distance from the crack tip as $\sigma(r) = K_0/\sqrt{2\pi r}$. Notably, for the present plane

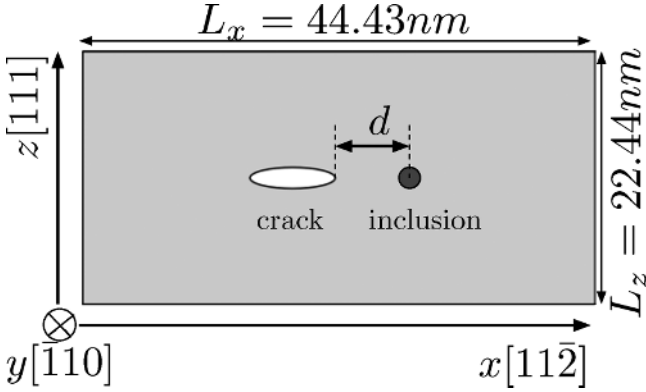


Figure 23 Geometry, orientation, and dimension of the simulation cell. Both the crack (left) and the cylindrical inclusion (right) are shown as well.

strain and mode-I configuration, K_0 coincides with the fracture toughness.¹²² The results of atomistic simulations show that such a square-root law is still valid even in the presence of the inclusion once K_0 is replaced with a renormalized expression $K_0 + \Delta K_{\text{tip}}$. To further develop this issue, we compare the stress $\sigma_{CI}(x)$ of a crack facing an inclusion with the corresponding value $\sigma_C(x)$ for an isolated crack, and we calculate (at vanishing distance δ from the crack tip) the ratio as follows:

$$\frac{\Delta K_{\text{tip}}}{K_0} = \lim_{\delta \rightarrow 0} \frac{\sigma_{CI}(x_C + \delta) - \sigma_C(x_C + \delta)}{\sigma_C(x_C + \delta)} \quad [155]$$

which corresponds to the relative variation of the stress intensity factor. Such a quantity depends on the relative crack-inclusion distance d and is reported in Figure 24 for the Si-inclusion/SiC-matrix case (top panel) and C-inclusion/SiC-matrix case (bottom panel), respectively. For C/SiC, the excess stress concentration resulting from the hard inclusion is purely tensile, and it effectively lowers the crack-tip toughness ($\Delta K_{\text{tip}} < 0$), thus giving rise to an overall mechanical stabilization of the system. This is an important result that illustrates the atomic-scale origin of fiber toughening.

To fully understand the usefulness of atomistic investigations, it is worth comparing the present results with conflicting continuum solutions by Li and Chen¹²³ and by Helsing.¹²⁴ In Ref. 123, the following expression was derived for ΔK_{tip} close to the crack tip and was induced by an inclusion of known shape:

$$\frac{\Delta K_{\text{tip}}}{K_0} = \frac{1}{\pi} \int_A r^{-2} \left(C_1 \cos \frac{\theta}{2} \cos \frac{3\theta}{2} + C_2 \sin^2 \theta \cos \theta \right) r dr d\theta \quad [156]$$

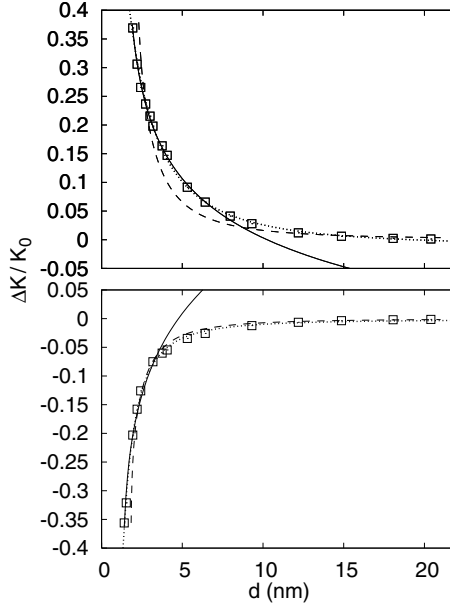


Figure 24 Stress intensity factor at the crack tip as a function of the crack-inclusion distance d . Top and bottom panels refer to silicon and carbon inclusion, respectively. Symbols are atomistic data and the dotted line is their best fit; the dashed line is based on the theory of Li and Chen;^{12,3} the continuous line is the best fit based on Helsing theory.¹²⁴

where $2A$ is the area of the inclusion and (r, θ) is the polar coordinate for a point within the inclusion with respect of the crack tip, whereas C_1 and C_2 are constants depending on the Young modulus and Poisson ratio, respectively. We can use Eq. [156] to fit the value of R , by keeping the value for the elastic constants as provided by the Tersoff model. The results are shown in Figure 24 as dashed lines. The agreement is very good for $d \geq 10$ nm, although at very short distances, the atomistic-continuum comparison is less satisfactory. We remark that the fitted value for R is about twice as large as the actual radius of the fiber.

By using the Helsing model,¹²⁴ we derive the following expression:

$$\frac{\Delta K_{\text{tip}}}{K_0} = \left[q_1 \left(\frac{d - R}{a} \right)^{(0.5 - \lambda)} - 1 \right] \quad [157]$$

where a is the crack semi-length; λ is a nondimensional parameter depending only on the elastic constants; q_1 approaches a constant as $(d - R)/a$ goes to zero. Once again, we can fit the atomistic data by using q_1 , R , and λ as adjustable parameters. As in the case of Li and Chen theory, the best fit provides

an increased radius, but in this case, the fitted value is just 30% larger than the actual one. The best values of λ are 0.61 and 0.38 for silicon and carbon inclusion, respectively. These numbers are in good agreement with the expected values $\lambda_{Si} = 0.62$ and $\lambda_C = 0.40$, as obtained from the elastic constants of Si, C, and SiC corresponding to the Tersoff potential. Overall, we can conclude that atomistic simulations show a better agreement with the continuum theory for the Helsing model at small crack-inclusion distances.

In a more general perspective, this investigation shows that the best available continuum models are not guaranteed to describe the stress intensification phenomena properly at arbitrary values of distance between the crack tip and the inclusion and for different matrix inclusion elastic mismatches. The atomistic results, instead, provided the following simple law for the effective variation of the crack toughness:

$$\frac{\Delta K_{\text{tip}}}{K_0} = \frac{c_1}{(d + c_2)^2} \quad [158]$$

where c_1 and c_2 are constants fitted directly on numeric results. For a Si (C) inclusion, we get $c_1 = 5.31$ (−0.87) and $c_2 = 1.85$ (0.15) nm, respectively. This equation is notably valid in both the silicon and carbon case (i.e., for very different matrix-inclusion mismatches) and provides a simple yet robust constitutive equation for stress intensification phenomena at any crack-inclusion distance in a ceramic composite.

Failure Strength in SiC-Containing Nanovoids

Voids affect the mechanical behavior of brittle solids because they modify the overall strength of the material. Sometimes such defects are unavoidable because they form during synthesis; alternatively, voids may be introduced into the material by design, to obtain specific properties as found, for example, in porous materials.¹²⁵

The strength of materials containing voids is described according to *stress intensification* or *stress concentration* arguments, as outlined in “Opening Modes and Stress Intensity Factors” it is common practice to assume that the failure takes place when the stress intensity factor K is equal to the material fracture toughness K_c .^{77,122} Once again, this criterion relies on the energy balance of the Griffith theory. In contrast, elasticity theory predicts that the failure from a void (as in the case of cylindrical or spherical holes) takes place when the maximum local stress equals the ideal material strength σ_{th} . Here, the key point is that both alternative continuum approaches are unlikely to work at the nanoscale. Their weaknesses, in principle, could be a result of the failure of at least one of the three underlying (constitutive) hypotheses upon which they rely—either continuum mechanics, or elasticity or linearity. It is, therefore, useful to address this problem by atomistic simulations in which none of the constitutive hypotheses is assumed a priori.¹²⁶

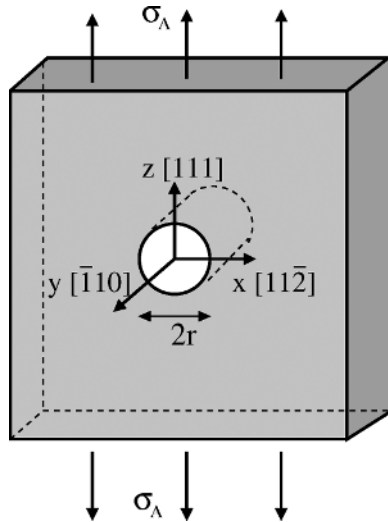


Figure 25 Geometry of a system containing a cylindrical hole and strained along the z -direction. A similar geometry is assumed for a straight crack and a spherical hole.

In Figure 25, we represent the geometry of the adopted simulation cell, consisting in a β -SiC monocrystal under tensile load, embedding either a cylindrical or a spherical hole. Our goal is to evaluate the failure strength of the defected specimen as a function of the defect size and shape. In the x - y plane, the simulation cell was kept fixed both in size and shape and repeated periodically. In this plane, the lattice parameter was 4.318 \AA , corresponding to the equilibrium length for β -SiC. The tensile load σ_A was applied along the z direction by means of the constant traction method.¹¹⁶ Throughout the simulation, the internal degrees of freedom (i.e., atomic positions) were completely free to relax in all directions. This simulation protocol reproduces the plane strain border conditions of continuum mechanics.

The cylindrical and the spherical holes were obtained by removing N_b atoms in a selected region of radius r at the center of the simulation cell. The hole size was $r + \delta r$, where δr is the maximum variation of the radius that does not modify the number N_b of removed atoms (we remark $\delta r \ll c_0$). The cylindrical voids were oriented along the y axis, perpendicularly to the applied stress. We observe that a simulated hole of given size can have a different surface structure depending on its position in the lattice. The simulation cell width was set with dimensions $L_x = L_z = L$ and $L_y \ll L$ (typically $L_y \simeq 12 \text{ \AA}$) for cylindrical voids, and we used a cubic shape $L_x = L_z = L_y = L$ for spherical holes. This corresponds to 2.5×10^5 and to 8×10^5 particles, respectively.

The ideal strength of β -SiC was calculated by simulating a perfect bulk loaded along the $[111]$ crystallographic axis up to the failure: the calculated critical strain and stress are $\varepsilon_{zz} \simeq 0.20$ and $\sigma_{th} = 58 \pm 1 \text{ GPa}$, respectively. The

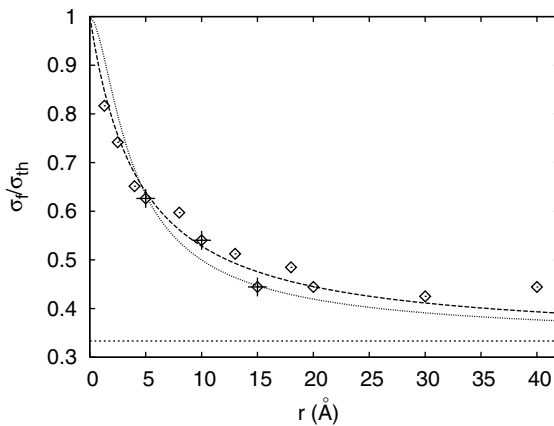


Figure 26 Failure strength for a system containing a cylindrical hole. Diamond (cross) symbols: atomistic data in plane strain (stress); horizontal dashed line: standard linear elasticity result; full and dot-dashed lines: two improved continuum models, as explained in the text.

value of σ_{th} is about $E/10$, where the Young modulus was estimated to be $E = 556 \pm 1$ GPa. This result is in qualitative agreement with a standard ansatz of continuum mechanics.¹²² On the other hand, the calculated failure strength for a system with an infinitely long cylindrical hole is represented in Figure 26 (open diamonds). For hole radii $r \leq 20$ Å, a strong dependence of σ_f on the hole size is observed, whereas the prediction $\sigma_f/\sigma_{th} = 1/3$ of continuum elasticity theory only represents the asymptotic limit for large radii. However, it is interesting to note that the full and dot-dashed curves nicely reproduce the atomistic results; they represent improved continuum models formulated so as to incorporate a suitable material length scale λ , aimed at describing a process zone close to the void in which at least one of these constitutive hypotheses fails.¹²⁶ Although the continuum model does not provide any hint for estimating λ , it is indeed possible to use atomistic data to determine it. A value ranging from 2.2 to 6.6 Å is found, thus proving that the deviation from standard continuum elasticity is a real nanoscale feature.

The results for the strength reduction resulting from a spherical hole are reported in Figure 27. Even in this case, σ_f depends strongly on the hole size, contrary to what is predicted by elasticity (i.e., $\sigma_f/\sigma_{th} = 1/2$). Introducing the parameter λ in the continuum theory as described allows us to improve the agreement with atomistics, as indicated by the full and dot-dashed line. In particular, we have calculated for a single vacancy a 4% strength reduction; this result is reproduced reasonably well by the improved elastic models.

Overall, this investigation proves that atomistic simulations are not only (as expected) more accurate at the nanoscale than are continuum fracture mechanics, but they also provide useful insight for the development (as well as

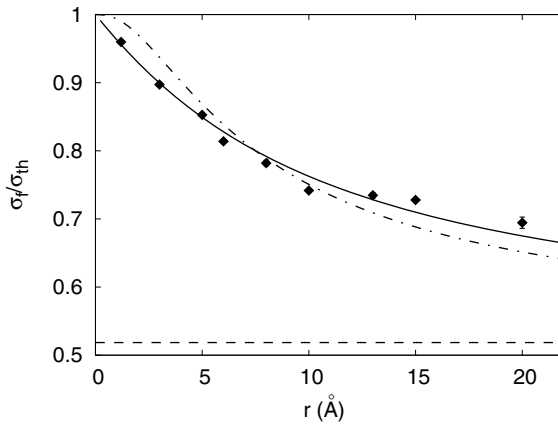


Figure 27 Failure strength for a spherical hole. Symbols: atomistic data; horizontal dashed line: standard linear elasticity result; full and dot-dashed lines: two improved continuum models, as reported in the text.

reliable data for the calibration) of improved elasticity theory models. In conclusion, we can state that atomistic simulations are valuable in developing atomically informed mesoscopic models.

Stress Shielding at Crack-Tip

In the previous sections, we considered separately the case of a crack and of an inclusion embedded into a SiC bulk matrix. We now investigate their mutual interaction, which represents the most fundamental issue in the physics of fiber reinforcing.¹²⁷

We adopted the geometry described in Figure 28 and the computational setup is the same as reported in the previous sections. In particular, several calculations were performed by varying the relative distance between the crack tip and the inclusion. The total number of atoms simulated here was as large as 60,840. The simulation protocol involved several steps: (1) a β -SiC monocrystal containing the carbon inclusion was relaxed at zero load; (2) the system then was strained at 8% by the application of constant tractions and again fully relaxed; (3) at this stage, the crack was inserted into the system along two different alignments, namely with horizontal (H-) and vertical (V-) relative orientation. The energy of a system containing both the inclusion and the microcrack is reported in Figure 29 where our result is expressed as energy per unit length of fiber as an inclusion in infinite fiber.

As the distance between the microcrack and inclusion decreases, the energy of the system lowers for the H alignment, as shown in Figure 29. This result indicates that an attraction basin exists between the two objects. Because no bond rearrangement occurs (the defects are spatially separated at all the distances considered) we can conclude further that such an energy basin must

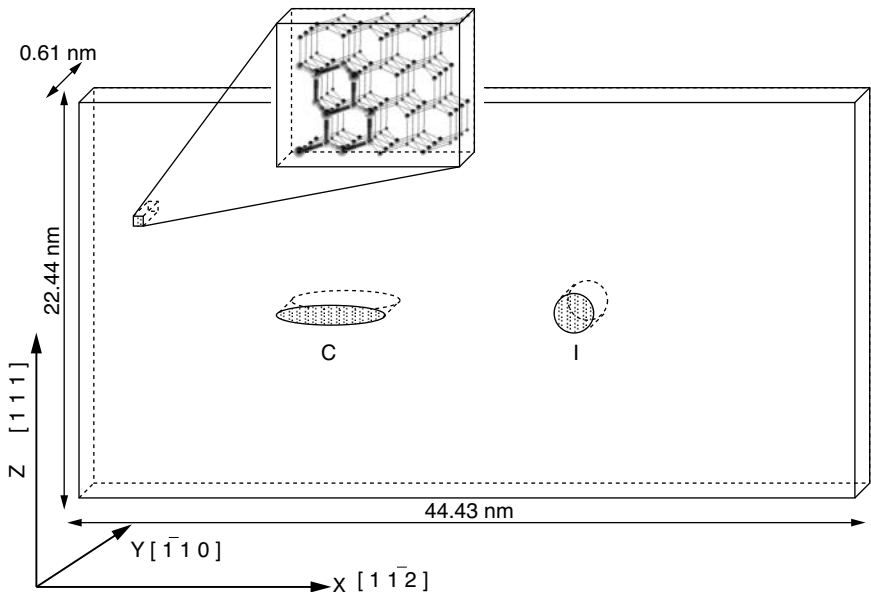


Figure 28 Geometry, orientation, crystal structure, and dimension of the simulation cell. Both the crack (C) and the cylindrical inclusion (I) are shown as well.

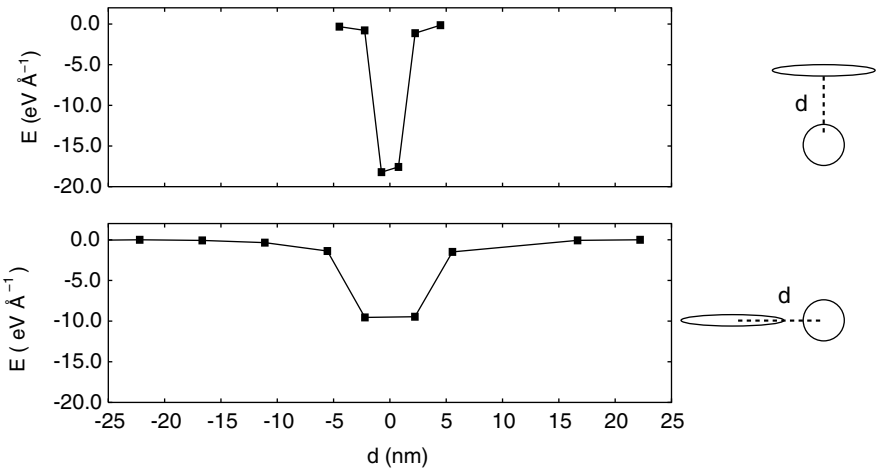


Figure 29 Top panel: energy of strained β -SiC ($\epsilon_{zz} = 8\%$) containing a stable crack and a diamond inclusion as a function of the relative distance for a vertical crack-inclusion alignment; bottom panel: the same for horizontal alignment.

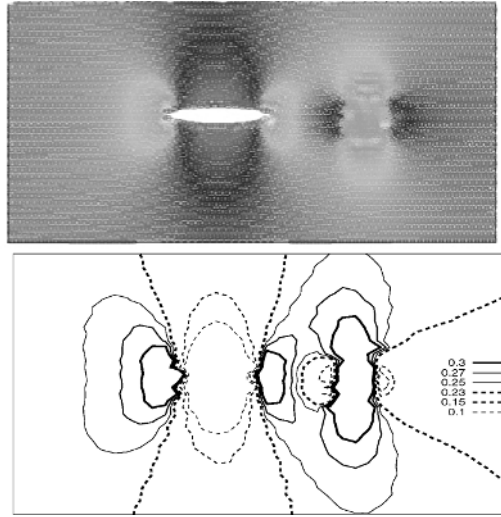


Figure 30 Top panel: stress map $\sigma_{zz}(x, y)$ of β -SiC containing both a diamond inclusion ($R = 10 \text{ \AA}$) and a stable crack ($a = 18 \text{ \AA}$) at the distance of 5.5 nm. Bottom panel: iso-stress contour plot (units of eV \AA^{-3}) for the same system. Note that only a small portion of the simulation cell is represented for the sake of clarity. Such a portion corresponds to a length of 18 nm and 10 nm in the x and z directions, respectively.

be attributed to the interaction between the stress fields of the microcrack and of the hard inclusion. The total stress field, generated by the defect pair and calculated according to the virial formulation reported in “Atomic-Scale Stress”, is reported in Figure 30. The region corresponding to the highest tensile stress (delimited by the the iso-stress contour $\sigma_{zz} = 0.27 \text{ eV \AA}^{-3}$) at the right crack tip is made smaller by the compressive stress lobe generated by the inclusion; at the same time, the iso-stress contour $\sigma_{zz} = 0.25 \text{ eV \AA}^{-3}$ (corresponding to a lower value of tensile stress) turns out to be extended all around the inclusion.

Another interesting feature is observed when the relative distance of the two defects is about 5.5 nm; in this situation, the opposite stress lobes interact with a net energy gain $\Delta E \sim 1.5 \text{ eV \AA}^{-1}$. The maximum depth of the attraction basin is reached when the crack tip and the inclusion are separated by just a few Ångström and the defects are nearly in contact ($\Delta E \sim 12 \text{ eV \AA}^{-1}$). For V alignment, we find a similar attraction basin; however, the interaction is now stronger (although more short-ranged), and the calculated energy basin has the depth $\Delta E \sim 18 \text{ eV \AA}^{-1}$.

Although the present results are obtained just for an especially clean configuration, they, nevertheless, prove a qualitatively important feature about the interaction between a microcrack and a hard diamond inclusion in β -SiC, namely the stress field annihilation at the crack tip caused by the inclusion. Basically, this corresponds to the observed reduced brittle failure of fiber-reinforced ceramics. Furthermore, atomistic simulations provide a topologically

complex potential energy landscape, proving that at small crack-inclusion distances, the system is energetically more stable.

ACKNOWLEDGMENTS

Many collaborators have been working with us on the topics discussed here. We warmly thank all of them, especially: Mariella Ippolito, Fabrizio Cleri, Giorgia Fugallo, and Nicola Pugno. Our research efforts have been funded by MiUR (under PRIN and PON projects), by ENEA, and by INFN (CNR). Computational support by CASPUR, CINECA, and the COSMOLAB supercomputing consortia is acknowledged as well.

APPENDIX: NOTATION

In this chapter, we adopt the following notation: the cartesian axis are indicated by (x_1, x_2, x_3) and the corresponding unit vectors are indicated by $\{\vec{e}_1, \vec{e}_2, \vec{e}_3\}$; the vectors appear as arrowed symbols (e.g., \vec{x}) with components $\{x_i\}_{i=1,2,3}$; the second-order tensors will be indicated as \hat{T} with components $\{T_{ij}\}_{i,j=1,2,3}$; the fourth-order tensor will appear as \hat{C} with components $\{C_{ijkl}\}_{i,j,k=1,2,3}$; the scalar product between vectors \vec{a} and \vec{b} is $\vec{a} \cdot \vec{b}$; the cross product between \vec{a} and \vec{b} is $\vec{a} \times \vec{b}$; the Einstein notation on repeated indexes is adopted: $a_{bk}b_k = \sum_k a_{bk}b_k$; the product matrix-matrix or matrix-vector are written as $\hat{A}\hat{B}$ or $\hat{A}\vec{v}$; the Kronecker symbol is δ_{ij} ($\delta_{ij} = 1$ if $i = j$ and $\delta_{ij} = 0$ if $i \neq j$); the identity tensor \hat{I} has components δ_{ij} ; the trace of a tensor is $\text{Tr}(\hat{T}) = T_{kk}$ (with sum over k); finally, the Levi-Civita permutation symbol is indicated as η_{nmj} ; it assumes the value 1 if (n, m, j) is an even permutation of (1, 2, 3), it assumes the value -1 if (n, m, j) is an odd permutation of (1, 2, 3), and it assumes the value 0 if there is a repetition in the numbers (n, m, j) ; such a symbol is useful to write the cross-product: $(\vec{a} \times \vec{b})_j = a_n b_m \eta_{nmj}$ or $\vec{a} \times \vec{b} = a_n b_m \eta_{nmj} \vec{e}_j$; the properties $\eta_{nmj} = \eta_{jnm} = \eta_{mjn}$ and $\eta_{ijk} \eta_{pqk} = \delta_{ip} \delta_{jq} - \delta_{iq} \delta_{jp}$ are useful; the tensor product of two vector \vec{a} and \vec{b} is given by the tensor $\vec{a} \otimes \vec{b}$ whose components are $(\vec{a} \otimes \vec{b})_{kb} = a_k b_b$; it follows that $(\vec{a} \otimes \vec{b})\vec{v} = \vec{a}(\vec{b} \cdot \vec{v})$.

REFERENCES

1. A. J. Fresnel, *Oeuvres Complètes*, Imprimerie Impériale, Paris, France, 1868.
2. C. L. M. H. Navier, *Mémoires de l'Académie des Sciences de l'Institut de France*, 7, 375 (1822). Mémoire sur les Lois de l'Équilibre et du Mouvement des Corps Solides Élastiques.
3. N. W. Ashcroft and N. D. Mermin, *Solid State Physics*, Saunders College Publishing, Orlando, FL, 1976.

4. C. Kittel, *Introduction to Solid State Physics*, 7th edition, John Wiley & Sons, New York, 1996.
5. J. H. Weiner, *Statistical Mechanics of Elasticity*, Dover Publication Inc., New York, 2002.
6. A. L. Cauchy, *Bulletin de la Société Philomathique*, 9–13, (1823). Recherches sur l'Équilibre et le Mouvement Intérieur des Corps Solides ou Fluides, Élastiques ou non Élastiques.
7. A. L. Cauchy, *Exercices de Mathématique*, 2, 108 (1827). Sur les Relations qui Existent dans l'État d'Équilibre d'un Corps Solide ou Fluide, entre les Pressions ou Tensions et les Forces Accélératrices.
8. I. Todhunter, *A History of the Theory of Elasticity and of the Strength of Materials from Galilei to the Present Time*, Cambridge University Press, Cambridge, UK, 1893.
9. W. Voigt, *Abhandlungen der königlichen Gesellschaft der Wissenschaften zu Göttingen*, 34, (1887). Theoretische Studien über die Elasticitätsverhältnisse der Krystalle.
10. L. Landau and E. Lifshitz, *Theory of Elasticity*, Pergamon Press, Oxford, UK, 1959.
11. T. L. Anderson, *Fracture Mechanics*, CRC Press, Boca Raton, FL, 1995.
12. A. A. Griffith, *Phil. Roy. Soc. London*, A 221, 163 (1920). The Phenomena of Rupture and Flow in Solids.
13. F. Erdogan, *Int. J. Solids Structures*, 37, 171 (2000). Fracture Mechanics.
14. J. L. Synge and A. Schild, *Tensor Calculus*, Dover Publication Inc., New York, 1978.
15. C. P. Chou and N. J. Pagano, *Elasticity. Tensor, Dyadic, and Engineering Approaches*, Dover Publication Inc., New York, 1992.
16. J. E. Marsden and T. J. R. Hughes, *Mathematical Foundations of Elasticity*, Dover Publication Inc., New York, 1994.
17. R. J. Atkin and N. Fox, *An Introduction to the Theory of Elasticity*, Dover Publication Inc., New York, 1980.
18. A. E. Green and W. Zerna, *Theoretical Elasticity*, Clarendon Press, Oxford, 1954.
19. V. V. Novozhilov, *Foundations of the Nonlinear Theory of Elasticity*, Dover Publication Inc., New York, 1999.
20. Y. A. Amenzade, *Theory of Elasticity*, MIR Publisher, Moscow, Russia, 1979.
21. I. N. Sneddon and D. S. Berry, in *Elasticity and Plasticity*, S. Flugge (Ed.), Springer Verlag, Berlin, 1958, Vol. VI, pp. 1–126, The Classical Theory of Elasticity.
22. A. E. H. Love, *A Treatise on the Mathematical Theory of Elasticity*, Dover Publication Inc., New York, 1964.
23. V. Parton and P. Perline, *Méthodes de la Théorie Mathématique de l'Élasticité*, First and Second, éditions MIR, Moscow, Russia, 1981.
24. M. Ciarletta and D. Iesan, *Non-Classical Elastic Solids*, Longman Scientific and Technical, Harlow, Essex, UK, 1993.
25. J. P. Den Hartog, *Advanced Strength of Materials*, Dover Publication Inc., New York, 1987.
26. J. Lubliner, *Plasticity Theory*, Macmillan Publishing Company, New York, 1990.
27. K. F. Graff, *Wave Motion in Elastic Solids*, Dover Publication Inc., New York, 1991.
28. V. Rékatch, *Problèmes de la Théorie de l'Élasticité*, MIR, Moscow, Russia, 1980.
29. T. Mura, *Micromechanics of Defects in Solids*, Kluwer Academic Publishers, Dordrecht, The Netherlands 1982.
30. R. Lakes, *Science*, 235, 1038 (1987). Foam Structures with a Negative Poisson's Ratio.
31. N. R. Keskar and J. R. Chelikowsky, *Nature*, 358, 222 (1992). Negative Poisson Ratios in Crystalline SiO₂ from First-Principles Calculations.
32. A. Yeganeh-Haeri, D. J. Weidner, and J. B. Parise, *Science*, 357, 650 (1992). Elasticity of α -Cristobalite: A Silicon Dioxide with a Negative Poisson's Ratio.

33. J. W. Martin, *J. Phys. C: Solid State Phys.*, **8**, 2837 (1975). Many-Body Forces in Metals and the Brugger Elastic Constants.
34. M. Catti, *Acta Cryst.*, **A41**, 494 (1985). Calculation of Elastic Constants by the Method of Crystal Static Deformation.
35. R. Pasianot, D. Farkas, and E. J. Savino, *Phys. Rev. B*, **43**, 6952 (1991). Empirical Many-Body Interatomic Potential for BCC Transition Metals. R. Pasianot, D. Farkas, and E. J. Savino, *Phys. Rev. B*, **47**, 4149 (1993). Erratum.
36. R. Pasianot and E. J. Savino, *Phys. Rev. B*, **45**, 12704 (1992). Embedded-Atom-Method Interatomic Potentials for HCP Metals.
37. R. Pasianot and E. J. Savino, *Phys. Stat. Sol. B*, **176**, 327 (1993). Elastic Constants for the HCP Lattice.
38. M. C. Rechtsman, F. H. Stillinger, and S. Torquato, *Phys. Rev. Lett.*, **101**, 085501 (2008). Negative Poisson Ratio Materials via Isotropic Interactions.
39. A. Mattoni, M. Ippolito, and L. Colombo, *Phys. Rev. B*, **76**, 224103 (2007). Atomistic Modeling of Brittleness in Covalent Materials.
40. J. E. Lennard-Jones, *Proc. Phys. Soc.*, **43**, 461 (1931). Cohesion.
41. T. H. K. Barron and C. Domb, *Proc. R. Soc. Lond. A, Math. Phys. Sci.*, **227**, 447 (1955). On the Cubic and Hexagonal Close-Packed Lattices.
42. F. Cleri, S. Yip, D. Wolf, and S. R. Phillpot, *Phys. Rev. Lett.*, **79**, 1309 (1997). Atomic-Scale Mechanism of Crack-Tip Plasticity: Dislocation Nucleation and Crack-Tip Shielding.
43. F. F. Abraham, *Phys. Rev. Lett.*, **77**, 869 (1996). Dynamics of Brittle Fracture with Variable Elasticity.
44. F. H. Stillinger and T. A. Weber, *Phys. Rev. B*, **31**, 5262 (1985). Computer Simulation of Local Order in Condensed Phases of Silicon.
45. C. Krzeminski, Q. Brulin, V. Cuny, E. Lecat, E. Lampin, and F. Cleri, *J. Appl. Phys.*, **101**, 123506 (2007). Molecular Dynamics Simulation of the Recrystallization of Amorphous Si Layers: Comprehensive Study of the Dependence of the Recrystallization Velocity on the Interatomic Potential.
46. D. Holland and M. Marder, *Adv. Mater.*, **11**, 783 (1999). Cracks and Atoms.
47. J. F. Justo, M. Z. Bazant, E. Kaxiras, V. V. Bulatov, and S. Yip, *Phys. Rev. B*, **58**, 2539 (1998). Interatomic Potential for Silicon Defects and Disordered Phases.
48. M. Z. Bazant, E. Kaxiras, and J. F. Justo, *Phys. Rev. B*, **56**, 8542 (1997). Environment-Dependent Interatomic Potential for Bulk Silicon.
49. M. Z. Bazant and E. Kaxiras, *Phys. Rev. Lett.*, **77**, 4370 (1996). Modeling of Covalent Bonding in Solids by Inversion of Cohesive Energy Curves.
50. G. C. Abell, *Phys. Rev. B*, **31**, 6184 (1985). Empirical Chemical Pseudopotential Theory of Molecular and Metallic Bonding.
51. J. H. Rose, J. R. Smith, F. Guinea, and J. Ferrante, *Phys. Rev. B*, **29**, 2963 (1984). Universal Features of the Equation of State of Metals.
52. J. Tersoff, *Phys. Rev. B*, **39**, 5566 (1989). Modeling Solid-State Chemistry: Interatomic Potentials for Multicomponent Systems.
53. D. W. Brenner, *Phys. Rev. B*, **42**, 9458 (1990). Empirical Potential for Hydrocarbons for Use in Simulating the Chemical Vapor Deposition of Diamond Films.
54. D. W. Brenner, O. A. Shenderova, J. A. Harrison, S. J. Stuart, B. Ni, and S. B. Sinnott, *J. Phys. Condens. Matter*, **14**, 783 (2002). A Second-Generation Reactive Empirical Bond Order (REBO) Potential Energy Expression for Hydrocarbons.
55. D. G. Pettifor and I. I. Oleinik, *Phys. Rev. B*, **59**, 8487 (1999). Analytic Bond-Order Potentials Beyond Tersoff-Brenner. I. Theory.
56. L. Pastewka, P. Pou, R. Pérez, P. Gumbsch, and M. Moseler, *Phys. Rev. B*, **78**, 161402 (2008). Describing Bond-Breaking Processes by Reactive Potentials: Importance of an Environment-Dependent Interaction Range.

57. M. Tang and S. Yip, *Phys. Rev. B*, **52**, 15150 (1995). Atomistic Simulation of Thermomechanical Properties of β -SiC.
58. D. Holland and M. Marder, *Phys. Rev. Lett.*, **80**, 746 (1998). Ideal Brittle Fracture of Silicon Studied with Molecular Dynamics.
59. N. Bernstein and D. W. Hess, *Phys. Rev. Lett.*, **91**, 025501 (2003). Lattice Trapping Barriers to Brittle Fracture.
60. H. Kicuchi, R. K. Kalia, A. Nakano, P. Vashista, P. Branicio, and F. Shimojo, *J. Appl. Phys.*, **98**, 103524 (2005). Brittle Dynamic Fracture of Crystalline Cubic Silicon Carbide (3C-SiC) via Molecular Dynamics Simulation.
61. J. G. Swadener, M. I. Baskes, and M. Nastasi, *Phys. Rev. Lett.*, **89**, 085503 (2002). Molecular Dynamics Simulation of Brittle Fracture in Silicon.
62. W. R. L. Lambrecht, B. Segall, M. Methfessel, and M. van Schilfgaarde, *Phys. Rev. B*, **44**, 3685 (1991). Calculated Elastic Constants and Deformation Potentials of Cubic SiC.
63. W. Li and T. Wang, *Phys. Rev. B*, **59**, 3993 (1999). Elasticity, Stability, and Ideal Strength of β -SiC in Plane-Wave-Based Ab Initio Calculations.
64. A. K. Subramaniyan and C.T. Sun, *Int. J. Solids Structures*, **45**, 4340 (2008). Continuum Interpretation of Virial Stress in Molecular Simulations.
65. M. Ippolito, G. Fugallo, A. Mattoni, and L. Colombo, *Strength, Fracture, Complexity*, **3**, 89 (2005). Fracture in Brittle Materials: The Atomic Scale Viewpoint.
66. A. G. McLellan, *Am. J. Phys.*, **42**, 239 (1974). Virial Theorem Generalized.
67. R. J. Swenson, *Am. J. Phys.*, **51**, 940 (1983). Comments for Virial Systems for Bounded Systems.
68. R. Clausius, *Phil. Mag.*, **40**, 122 (1870). On a Mechanical Theory Applicable to Heat.
69. J. C. Maxwell, *Trans. R. Soc. Edinburg*, **XXVI**, 1 (1870). On Reciprocal Figures, Frames and Diagrams of Forces.
70. M. Zhou, *Proc. R. Soc. Lond. A*, **459**, 2347 (2003). A New Look at The Atomic Level Virial Stress: On Continuum-Molecular System Equivalence.
71. J. H. Irving and J. G. Kirkwood, *J. Chem. Phys.*, **18**, 817 (1950). The Statistical Mechanical Theory of Transport Processes. IV. The Equations of Hydrodynamics.
72. P. C. Andia, F. Costanzo, and G. L. Gray, *Model. Simul. Mater. Sci. Eng.*, **14**, 741 (2006). A Classical Mechanics Approach to the Determination of the Stress and Strain Response of Particle Systems.
73. P. C. Andia, F. Costanzo, and G. L. Gray, *Int. J. Solids Structures*, **42**, 6409 (2005). A Lagrangian-Based Continuum Homogenization Approach Applicable to Molecular Dynamics Simulations.
74. J. Gao and J. H. Weiner, *Macromolecules*, **20**, 2520 (1987). Excluded-Volume Effects in Rubber Elasticity. 1. Virial Stress Formulation.
75. C. E. Inglis, *Trans. Inst. Naval Arch. London*, **LV**, 219 (1913). Stresses in a Plate Due to the Presence of Cracks and Sharp Corners.
76. G. Kolossoff, *Zeitschrift für Math. und Physik*, **62**, 384 (1914). Über einige Eigenschaften des ebenen Problems der Elastizitätstheorie.
77. K. B. Broberg, *Cracks and Fracture*, Academic Press, London, UK, 1999.
78. S. P. Timoshenko and J. N. Goodier, *Theory of Elasticity*, McGraw Hill, New York, 1951.
79. G. R. Irwin, *J. Appl. Mech.*, **24**, 361 (1957). Analysis of Stresses and Strains Near the End of a Crack Traversing a Plate.
80. S. Giordano and L. Colombo, *Phys. Rev. B*, **76**, 174120 (2007). Local Elastic Fields Around Cracks and Their Stress Density of States.
81. J. D. Eshelby, *Proc. R. Soc. Lond.*, **A241**, 376 (1957). The Determination of the Elastic Field of an Ellipsoidal Inclusion and Related Problems.

82. J. D. Eshelby, *Proc. R. Soc. Lond.*, **A252**, 561 (1959). The Elastic Field Outside an Ellipsoidal Inclusion.
83. L. J. Walpole, *Adv. Appl. Mech.*, **11**, 169 (1981). Elastic Behavior of Composite Materials: Theoretical Foundations.
84. S. Giordano, *Eur. J. Mech. A/Solids*, **22**, 885 (2003). Differential Schemes for the Elastic Characterization of Dispersions of Randomly Oriented Ellipsoids.
85. S. Giordano and L. Colombo, *Phys. Rev. Lett.*, **98**, 055503 (2007). Effects of the Orientational Distribution of Cracks in Solids.
86. S. Giordano and L. Colombo, *Phys. Rev. B*, **77**, 054106 (2008). Elastic Properties of Solids Containing Elliptic Cracks.
87. J. H. Weiner and M. Pear, *J. Appl. Phys.*, **46**, 2398 (1975). Crack and Dislocation Propagation in an Idealized Crystal Model.
88. W. T. Ashurst and W. G. Hoover, *Phys. Rev. B*, **14**, 1465 (1976). Microscopic Fracture Studies in the Two-Dimensional Triangular Lattice.
89. R. Thomson, C. Hsieh, and V. Rana, *J. Appl. Phys.*, **42**, 3154 (1971). Lattice Trapping of Fracture Cracks.
90. D. Frenkel and B. Smit, *Understanding Molecular Simulations*, Academic Press, San Diego, CA, 1996.
91. P. Paskin, A. Gohar, and G. J. Dienes, *Phys. Rev. Lett.*, **44**, 940 (1980). Computer Simulation of Crack Propagation.
92. P. Paskin, D. K. Som, and G. J. Dienes, *J. Phys. C*, **14**, L171 (1981). Computer Simulation of Crack Propagation: Lattice Trapping.
93. T. F. Soules and R. F. Busbey, *J. Chem. Phys.*, **78**, 6307 (1983). The Rheological Properties and Fracture of a Molecular Dynamic Simulation of Sodium Silicate Glass.
94. P. Ray and B. K. Chakrabarti, *J. Phys. C*, **18**, L185 (1985). The Critical Behavior of Fracture Properties of Dilute Brittle Solids Near the Percolation Threshold.
95. P. Ray and B. K. Chakrabarti, *Solid State Commun.*, **53**, 477 (1985). A Microscopic Approach to the Statistical Fracture Analysis of Disordered Brittle Solids.
96. B. K. Chakrabarti, D. Chowdhury, and D. Stauffer, *Z. Phys. B*, **62**, 343 (1986). Molecular Dynamic Study of Fracture in 2D Disordered Elastic Lennard-Jones Solids.
97. K. S. Cheung and S. Yip, *Phys. Rev. Lett.*, **65**, 2804 (1990). Brittle-Ductile Transition in Intrinsic Fracture Behavior of Crystals.
98. F. Cleri, S. R. Phillpot, S. Yip, and D. Wolf, *J. Am. Ceram. Soc.*, **81**, 501 (1998). Atomistic Simulations of Materials Fracture and the Link between Atomic and Continuum Length Scales.
99. A. Cao and Y. Wei, *Phys. Rev. B*, **76**, 024113 (2007). Atomistic Simulations of Crack Nucleation and Intergranular Fracture in Bulk Nanocrystalline Nickel.
100. C. L. Rountree, R. K. Kalia, E. Lidorikis, A. Nakano, L. Van Brutzel, and P. Vashishta, *Ann. Rev. of Mat. Res.*, **32**, 377 (2002). Atomistic Aspects of Crack Propagation in Brittle Materials: Multimillion Atom Molecular Dynamics Simulations.
101. R. Perez and P. Gumbsch, *Phys. Rev. Lett.*, **84**, 5347 (2000). Directional Anisotropy in the Cleavage Fracture of Silicon.
102. P. Lazar and R. Podloucky, *Phys. Rev. B*, **78**, 104114 (2008). Cleavage Fracture of a Crystal: Density Functional Theory Calculations Based on a Model Which Includes Structural Relaxations.
103. P. Gumbsch, *Mat. Sci. Eng. A*, **319**, 1 (2001). Modeling Brittle and Semi-Brittle Fracture Processes.
104. T. Hoshi and T. Fujiwara, *J. Phys. Soc. Jpn.*, **72**, 2429 (2003). Dynamical Brittle Fractures of Nanocrystalline Silicon using Large-Scale Electronic Structure Calculations.
105. G. Galli, F. Gygi, and A. Catellani, *Phys. Rev. Lett.*, **82**, 3476 (1999). Quantum Mechanical Simulations of Microfracture in Complex Materials.

106. P. Gumbsch, Ed., *Conference Proceedings, 3rd Int. Conference Multiscale Materials Modeling*, Frunhofer-Istitute for Mechanics of Materials, Freiburg, Germany, 2006.
107. F. F. Abraham, J. Q. Broughton, N. Bernstein, and E. Kaxiras, *Eur. Phys. Lett.*, **44**, 783 (1998). Spanning the Continuum to Quantum Length Scales in a Dynamic Simulation of Brittle Fracture.
108. G. Lu and E. B. Tadmor, and E. Kaxiras, *Phys. Rev. B*, **73**, 024108 (2006). From Electrons to Finite Elements: A Concurrent Multiscale Approach for Metals.
109. C. Csanyi, T. Albaret, M. C. Payne, and A. De Vita, *Phys. Rev. Lett.*, **93**, 175503 (2004). Learn on the Fly: A Hybrid Classical and Quantum-Mechanical Molecular Dynamics Simulation.
110. M. J. Buehler, A. C. T. van Duin, and W. A. Goddard III, *Phys. Rev. Lett.*, **96**, 095505 (2006). Multiparadigm Modeling of Dynamical Crack Propagation in Silicon Using a Reactive Force Field.
111. M. Buehler and T. Ackbarow, *Materials Today*, **10**, 46 (2007). Fracture Mechanics of Protein Materials.
112. M. Sahimi, *Heterogeneous Materials I, Linear Transport and Optical Properties*, Springer-Verlag, New York, 2003.
113. M. Sahimi, *Heterogeneous Materials II, Nonlinear and Breakdown Properties and Atomistic Modeling*, Springer-Verlag, New York, 2003.
114. M. Tang and S. Yip, *J. Appl. Phys.*, **76**, 2719 (1994). Lattice Instability in β -SiC and Simulation of Brittle Fracture.
115. A. Mattoni, L. Colombo, and F. Cleri, *Phys. Rev. Lett.*, **95**, 115501 (2005). Atomic Scale Origin of Crack Resistance in Brittle Fracture.
116. F. Cleri, *Phys. Rev. B*, **65**, 014107 (2002). Representation of Mechanical Loads in Molecular Dynamics Simulations.
117. B. A. Bilby, A. H. Cottrell, and K. H. Swinden, *Proc. R. Soc. London A*, **272**, 304 (1963). The Spread of Plastic Yield from a Notch.
118. H. Awaji, S. M. Choi, and E. Yagi, *Mech. Mater.*, **34**, 411 (2002). Mechanisms of Toughening and Strengthening in Ceramic-Based Nanocomposites.
119. J. D. Kuntz, G. Zhan, and A. K. Mukherjee, *Mat. Res. Bull.*, **29**, 22 (2004). Nanocrystalline-Matrix Ceramic Composites for Improved Fracture Toughness.
120. R. Naslain, *Int. J. Appl. Ceram. Technol.*, **2**, 73 (2005). SiC-Matrix Composites: Nonbrittle Ceramics for Thermo-Structural Applications.
121. M. Ippolito, A. Mattoni, L. Colombo, and F. Cleri, *Appl. Phys. Lett.*, **87**, 14912 (2005). Fracture Toughness of Nanostructured Silicon Carbide.
122. B. R. Lawn, *Fracture of Brittle Solids*, Cambridge University Press, Cambridge, UK, 1975.
123. Z. Li and Q. Chen, *Eng. Fract. Mech.*, **70**, 581 (2003). Some Simple Formulas to Predict the Variation of Stress Intensity Factors for Mode I Crack Induced by Near Crack-Tip Inclusion.
124. J. Helsing, *Eng. Fract. Mech.*, **64**, 245 (1999). Stress Intensity Factors for a Crack in Front of an Inclusion.
125. L. J. Gibson and M. F. Ashby, *Cellular Solids: Structure and Properties*, Cambridge University Press, Cambridge, UK, 1997.
126. M. Ippolito, A. Mattoni, N. Pugno, and L. Colombo, *Phys. Rev. B*, **75**, 224110 (2007). Failure Strength of Brittle Materials Containing Nanovoids.
127. A. Mattoni, L. Colombo, and F. Cleri, *Phys. Rev. B*, **70**, 094108 (2004). Crack-Tip Stress Shielding by a Hard Fiber in β -SiC: An Atomistic Study.

